

ELECTRON NUCLEAR DOUBLE RESONANCE STUDIES OF FREE RADICALS
TRAPPED IN IRRADIATED SINGLE CRYSTALS OF SODIUM FORMATE
AND POTASSIUM HYDROGEN BISPHENYLACETATE

by

JOHN MELVYN PARK

B.A., University of Keele, 1970

A THESIS SUBMITTED IN PARTIAL FULFILLMENT OF
THE REQUIREMENTS FOR THE DEGREE OF

DOCTOR OF PHILOSOPHY

In the Department of
Chemistry

We accept this thesis as conforming to the
required standard

THE UNIVERSITY OF BRITISH COLUMBIA

January, 1977

(c) John Melvyn Park, 1977

In presenting this thesis in partial fulfilment of the requirements for an advanced degree at the University of British Columbia, I agree that the Library shall make it freely available for reference and study.

I further agree that permission for extensive copying of this thesis for scholarly purposes may be granted by the Head of my Department or by his representatives. It is understood that copying or publication of this thesis for financial gain shall not be allowed without my written permission.

Department of Chemistry

The University of British Columbia
2075 Wesbrook Place
Vancouver, Canada
V6T 1W5

Date 24th January 1977

Abstract

Electron Nuclear Double Resonance (ENDOR) measurements have been made of hyperfine couplings in x-irradiated single crystals of sodium formate and potassium hydrogen bisphenylacetate (KHBP).

In sodium formate ENDOR signals were obtained from both proton and sodium ion neighbours of the CO_2^- centre formed on irradiation. ENDOR studies of the ^{23}Na hyperfine interaction together with CNDO calculations indicate that the CO_2^- forms a tight ion pair with the nearer Na^+ cation, thus explaining the four line EPR hfs. observed. Hf. interactions have also been resolved for four pairs of nearest neighbour protons. The tensors are mainly dipolar in character, but contain some isotropic contributions which are interpreted in terms of covalent interactions.

Extra so-called 'forbidden' lines are observed in the ^{23}Na ENDOR and a model of ENDOR enhancements involving cross relaxation with other paramagnetic species is suggested.

CO_2^- was also observed in uv-irradiated samples: the threshold energy for radical formation was estimated to be $100 \pm 10 \text{ kcal mole}^{-1}$. A previously reported free-radical reaction in sodium formate was found to be reversed by uv irradiation, the reaction obeying second order kinetics.

Proton ENDOR studies of x-irradiated KHBP confirmed the presence of the benzyl radical, for which all seven anisotropic proton hyperfine tensors were measured. The isotropic couplings agree with earlier EPR measurements of the benzyl radical undergoing free rotation. The dipolar couplings provide an independent estimate of the spin density distribution in the radical which is not in complete accord with earlier determinations based on the McConnell relation. The dipolar tensors imply a spin distribution close to that

predicted by INDO and other calculations, which suggests that these calculations may be qualitatively correct, and the McConnell relation not strictly applicable.

Several other radicals are also present in irradiated KHBP. Two are tentatively identified as cyclohexadienyl type radicals formed by hydrogen addition at the phenyl ring ortho and para to the methylene carboxy group.

TABLE OF CONTENTS

	<u>Page</u>
ABSTRACT	i
TABLE OF CONTENTS	iii
LIST OF TABLES	vi
LIST OF FIGURES	vii
ACKNOWLEDGEMENTS	ix
CHAPTER 1 INTRODUCTION	1
CHAPTER 2 THEORETICAL	7
2.1 The Spin Hamiltonian	7
2.2 Hamiltonian Parameters	8
2.3 The Eigenvalue Problem	12
2.3(a) EPR Hamiltonian with Field Along a principal direction ($S-I=\frac{1}{2}$)	13
2.3(b) EPR Hamiltonian with Field in a General Direction	18
2.3(c) Introduction of the Nuclear Zeeman Term - 'Forbidden Transitions	19
2.3(d) ENDOR Transitions	21
2.3(e) ENDOR Intensities	25
2.4 NMR Experiments in Paramagnetic Systems	25
2.5 The ENDOR Experiment	28
2.6 Relation of Hyperfine Coupling Tensors to Electronic Structure	32
2.6(a) Isotropic Couplings	33
2.6(b) The McConnell Relationship	34

	<u>Page</u>
2.6(c) β Proton Couplings	36
2.6(d) Anisotropic Couplings	38
2.6(e) Multicentre Terms	40
2.6(f) Three Centre Terms	42
2.6(g) Applications	42
CHAPTER 3 EXPERIMENTAL	44
3.1 Experimental	44
3.2 ENDOR Spectrometer	44
3.3 Field and Frequency Calibration	48
3.4 ENDOR Experiments	49
3.5 Irradiation Units	50
3.6 Sample Preparation	51
3.7 Data Analysis	52
3.7(a) Preliminary Analysis	52
3.7(b) Determination of Hyperfine Parameters	53
3.8 CNDO/INDO Calculations	54
3.9 Crystal Alignment	55
CHAPTER 4 EPR AND ENDOR STUDIES OF CO_2^- CENTRES IN UV- AND X-IRRADIATED SINGLE CRYSTALS OF SODIUM FORMATE	58
4.1 Introduction	58
4.2 EPR of uv-Irradiated Crystals	63
4.3 Proton ENDOR Studies	65
4.4 Sodium Hyperfine Interaction	74
4.5 ENDOR Intensities and Relaxation Mechanisms	82

	<u>Page</u>
CHAPTER 5	
ENDOR STUDIES OF AN X-IRRADIATED	
SINGLE CRYSTAL OF POTASSIUM	
HYDROGEN BISPHENYLACETATE	87
5.1 Introduction	87
5.2 The Benzyl Radical	91
5.3 Results and Discussion: Benzyl Radical	94
5.4 Other Radicals	106
REFERENCES	115
APPENDIX 1	
The Effect of g-Anisotropy on ENDOR	
Frequencies	122
APPENDIX 2	
Some Aspects of the Dipolar Hyperfine	
Interaction	126
APPENDIX 3	
Misalignment of Planes of Observation	129
APPENDIX 4	
A uv-Induced Radical Reaction in	
Irradiated Sodium Formate	133

LIST OF TABLES

TABLE		Page
I	EPR Parameters for the CO_2^- Centre Produced by γ and UV Irradiation	64
II	Proton Hyperfine Tensors in λ -Irradiated Sodium Formate . .	73
III	CNDO Spin Densities as Functions of Geometry	78
IV	Proton Hyperfine Tensors in the Benzyl Radical	98
V	Proton Isotropic Coupling Constants (MHz) for the Benzyl Radical in Different Media	99
VI	Angles ϕ_i° Between σ Vector of Proton Tensor i and σ Vector of para proton tensor	99
VII	Proton Dipolar Coupling Tensors in Benzyl Radical (MHz) . .	103
VIII	Hyperfine Tensors for Radicals I and II.	108
IX	Hyperfine Tensors in the Cyclohexadienyl and α -Naphthyl Radicals	109

LIST OF FIGURES

FIGURE		Page
1.	EPR and ENDOR transitions for a system with $S=I=\frac{1}{2}$.	16
2.	First order ENDOR transitions for a system with $S=\frac{1}{2}$ $I=3/2$.	23
3.	Relaxation pathways for a system with $S=I=\frac{1}{2}$.	30
4.	(a) Schematic representation of isotropic proton couplings induced by σ - π polarisation. (b) Dihedral angle θ used in calculating β proton couplings.	35
5.	Coordinate system used in McConnell-Strathdee calculations.	39
6.	Block diagram of ENDOR spectrometer.	45
7.	Typical morphology and axis systems for sodium formate.	59
8.	Angular variation of proton ENDOR frequencies in (a) approximate $\alpha\beta$ and (b) the approximate $\gamma\beta$ plane.	66
9.	Angular variation of proton ENDOR frequencies in the approximation $\alpha\gamma$ plane sodium formate.	67
10.	A typical ENDOR spectrum of x-irradiated sodium formate at 77K.	68
11.	Projection of part of the sodium formate lattice into the crystallographic bc plane, showing the hydrogen atoms corresponding to the hyperfine tensors listed in Table II.	70
12.	Schematic representation of p-orbital overlaps inducing spin density in an HCO_2^- neighbour of the CO_2^- radical ion.	71
13.	Sodium ENDOR spectrum in the frequency range near the free sodium NMR frequency ν_{Na} .	75
14.	Sodium ENDOR spectra obtained by irradiating EPR lines i-iv in turn, in order of decreasing field.	80
15.	Appearance of all three sodium ENDOR lines obtained by irradiating the lowest field EPR line.	81
16.	ENDOR spectrum obtained from sodium formate crystal after 11.5 h x-irradiation, showing the strong distant ENDOR proton resonance line.	84
17.	Sodium ENDOR lines obtained by irradiating the second lowest field EPR line at 4.2K.	85
18.	External morphology and axis system of KHBP single crystal.	88
19.	Projection of part of the KHBP crystal lattice onto the ac plane.	89
20.	Angular variation of proton ENDOR spectra from the benzyl radical in x-irradiated KHBP.	93

FIGURE		Page
21.	Typical EPR(a) and ENDOR(b) spectra of x-irradiated KHBP obtained at 77K.	95
22.	INDO overlap spin densities in the benzyl radical.	104
23.	Proton dipolar vectors in cyclohexadienyl.	110
24.	Assignments of hydrogen addition radicals I and II.	111
25.	Angular variation of ENDOR spectra for radicals I and II.	112
26.	Relative intensities of CO_2^- (C) and secondary radical (X) EPR spectra as a function of uv-irradiation time.	134
27.	Ratio of EPR intensities $[\text{C}]/[\text{X}]$ plotted against uv-irradiation time. Data from Fig. 26.	135

Acknowledgements

I wish to thank Dr. C.A. McDowell for supervising the work described here, and for suggesting the problems studied.

I am grateful to Mr. P. Markila for performing the crystal structure analysis of sodium formate and identifying the axes of crystals used for ENDOR measurements, and to Dr. J.C. Speakman of Glasgow University for very kindly providing unpublished results of a redetermination of the crystal structure of potassium hydrogen bisphenylacetate.

Two discussions with Dr. J. Trotter were instrumental in elucidating the implications of Dr. Speakman's results.

Dr. F.G. Herring was a continual source of advice and encouragement, and Drs. J.B. Farmer and W.C. Lin provided useful background information about instrumentation and the EPR spectra of irradiated potassium hydrogen bisphenylacetate.

Messrs. T. Markus and K. Sukul provided expert maintenance of the spectrometers used.

I must thank all my colleagues for their interest and encouragement. Particularly, I thank Dr. N.S. Dalal whose friendship, scientific expertise and unflagging enthusiasm were invaluable during the inevitable periods of frustration.

I am grateful to the National Research Council of Canada for a Graduate Student Bursary, and to the Department of Chemistry for several assistantships.

Chapter 1

INTRODUCTION

Viewed classically, the magnetic resonance phenomenon is a consequence of the fact that a magnetic dipole will precess about a fixed magnetic field with a characteristic (Larmor) frequency. If a rotating or oscillatory magnetic field is applied in the plane of this precession, it produces a maximum effect when its frequency of oscillation is equal to the Larmor frequency. This frequency equality is called the resonance condition: when it is satisfied the precessing dipole will strongly absorb energy from the oscillating field and widen the cone of its precession. A quantum mechanical analysis yields essentially the same result.

Two of the most important applications of this effect have been in electron paramagnetic resonance (EPR) and nuclear magnetic resonance (NMR), in which the magnetic dipoles are provided by the electronic and nuclear spin respectively. These two techniques are complementary in the types of system to which they can be applied, and also in the sense that EPR has the higher sensitivity and NMR the higher resolution.

A double resonance experiment consists in satisfying two such resonance conditions simultaneously, in such a way that the energy absorption by one resonance influences the absorption by the other. Such an experiment can be invaluable in studying (or eliminating) the interactions between different spins in a given system.

In its widest sense the term electron nuclear double resonance encompasses such experiments as dynamic nuclear polarisation and the solid state and Overhauser effects (1-6); the acronym ENDOR however refers to a specific experiment originated by Feher in 1956 (7-9) to measure the hyperfine couplings of magnetic nuclei interacting with paramagnetic centres.

This technique proved useful from the first because it was able to resolve hyperfine couplings which were comparable to or even hidden within the electron paramagnetic resonance linewidth. A classic example of this was the experiment by Holton, Blum and Slichter (10) on F centres in LiF in which splittings were resolved for nuclei as much as seven shells away from the defect centre, all the couplings being within the EPR linewidth.

The early applications of ENDOR were to such inorganic systems, particularly to the study of point defects in alkali halide crystals. For nuclei such as chlorine, sodium or nitrogen, with spins greater than $\frac{1}{2}$, ENDOR can also measure the quadrupole coupling constant if the local symmetry allows this to be non-zero. Hyperfine and quadrupole parameters were measured by Cook and Whiffen (11) for nitrogen centres trapped in diamond. In many cases too it was possible to make accurate measurement of the effective nuclear g-factors and to relate the observed anisotropies to the electronic structure of the paramagnetic centre. ENDOR of point defects in alkali halide crystals has been the subject of several reviews. (12-15)

Systems of more chemical interest studied by ENDOR have included ligand superhyperfine in transition metal complexes (16-18) and, hyperfine interactions in organic triplet state molecules (19-21), and in free radicals. The first two of these are again adequately covered in the literature, so this discussion of them will be brief. The analysis of ligand superhyperfine structure enables one to estimate the amount of admixture of ligand wavefunctions to the wavefunction of the metal ion, and hence to estimate the covalent contributions to the metal-ligand bonding. In the higher multiplet states one's main interest is in using the measured hyperfine parameters to describe the delocalised orbitals containing the unpaired electrons.

Probably the largest area of study and the one of most interest here has been that of organic free radicals. For these the range of available nuclei is quite limited, and probably 90% of the work has been on proton ENDOR. Halogen and metals hyperfine couplings have been determined. But of the elements usually present in such species, carbon, oxygen and sulphur all consist of at least 99% zero-spin isotopes, while ENDOR of nitrogen nuclei is hindered by quadrupole relaxation effects (22).

Proton ENDOR has at least two advantages. First the high proportion of hydrogen atoms in most organic molecules means that there will be many possible couplings to measure, both inter- and intra-molecular. Secondly, the interpretation of such couplings is simplified by the fact that for hydrogen only the 1s orbital is occupied.

The information derived from the proton hyperfine couplings can be related to the electronic structure of the radical, and more fundamentally can be used to identify the radical itself. This use of ENDOR has proved particularly valuable in studies of radiation-damaged crystals of amino acids (23-26) and other molecules of biological interest (27-30); in these cases the EPR spectrum is often too complex or poorly resolved for

analysis and ENDOR provides the only means of identifying the radical. In many cases too ENDOR has shown that such unresolved spectra are due to more than one species, when this was not apparent from the EPR spectrum itself (28-29).

Such results taken in conjunction with knowledge of the temperature of irradiation and of the crystal structure have been used to infer the mechanism of radical formation. (27, 31)

Improvements in instrumentation have opened up new possibilities for the application of ENDOR and this survey concludes with an account of some of these developments.

The application of ENDOR to the study of powders or glasses rather than single crystals requires the use of larger samples but reduces the amount of data analysis needed (32-38). Relaxation effects become more complex and important in this case, and can be used to advantage. The method is particularly useful for the study of complex biological molecules which do not form good crystals.

In recent years ENDOR has been applied to the study of free radicals and ion pairs in the liquid phase (40-42). This poses much more stringent requirements, since it necessitates relatively high temperatures, at which relaxation makes low power saturation of the EPR signal impossible. As a result radio-frequency amplifiers producing of the order of 1 kW are needed and the consequent problems of radio-frequency interference can be severe. (40)

Double ENDOR, electron nuclear triple resonance, or TRIPLE are extensions of the ENDOR experiment to the simultaneous saturation of two nuclear resonances; as a result the relative signs of the two couplings can be determined. The experiment is difficult and has rarely been performed

on solids (43, 44), but recent results suggest that it may find useful application in the liquid phase. (45)

Optical detection of ENDOR is a technique of high sensitivity which can be used to measure the hyperfine interactions in the excited triplet states of diamagnetic molecules; it has been profitably applied to the study of biological molecules (46, 47).

These and other aspects of ENDOR are well covered in review articles (50, 51)

The work described in this thesis mainly concerns proton ENDOR studies of free radicals in irradiated single crystals (52, 53). The couplings measured encompass the most useful range of ENDOR; in the case of CO_2^- centre described in Chapter 4 the proton couplings are intermolecular, mainly dipolar in character and 3 MHz or less in magnitude; for the radicals trapped in X-irradiated potassium-hydrogen bisphenylacetate described in Chapter 5, the couplings are intramolecular, with significant isotropic parts, and in some cases magnitudes greater than 50 MHz. The work described in Chapter 4 also includes some ENDOR studies of neighbouring sodium nuclei, from which structural information was deduced and relaxation mechanisms qualitatively assessed.

In Chapter 4 the emphasis is on intermolecular interactions and a probe of the radical's environment; in Chapter 5 it is on the identification of the radicals and the determination of their geometric and electronic structures.

The theory of the Spin Hamiltonian and its application to ENDOR is presented in Chapter 2, together with a discussion of the ENDOR experiment itself and the interpretation of hyperfine tensors in terms of electronic structure.

Chapter 3 describes the experimental procedures and instrumentation used to obtain the data, and the methods of data analysis and interpretation.

Chapter 2

THEORETICAL

2.1 The Spin Hamiltonian

Note on Units

In the following discussion, unless otherwise stated, energies will be assumed to be given in frequency units (generally MHz), so that for example the simple expression for the EPR resonance condition would be written

$$\nu = g\beta H ;$$

angular momenta are given in units of \hbar ; thus the statement 'I=3/2' refers to a nucleus with angular momentum $3/2\hbar$.

Several thorough and detailed comprehensive accounts of the Spin Hamiltonian are available in the literature (104-6). Rather than attempting to imitate them, this discussion is in the nature of an overview with a phenomenological bias and some emphasis on points of particular relevance to the rest of this thesis.

Historical

In 1950 Pryce (54) showed that the magnetic properties of a doublet or higher state could be described by a single spin operator, and that the result was accurate to second order in energy; and the following year Abragam and Pryce (55) extended the formulation to include hyperfine interactions. These results are fundamental since they make the theory of magnetic resonance tractable, reducing a many-electron problem to one involving the effective Hamiltonian of a single electron. In the spirit of this formulation the results of electron paramagnetic resonance experiments are often successfully interpreted in terms of a single unpaired electron occupying a unique molecular orbital.

2.2 Hamiltonian Parameters

With the work of Pryce et al the spin Hamiltonian came to take on a conventional form, primarily justified by the success of its applications. Pake and Estle (56) have discussed the type of Hamiltonian parameters which are allowed by symmetry and the dimension of the basis set of spin functions. Several of the terms they describe apply only to transition metals or to higher multiplet states of organic molecules or are negligibly small, and for the cases of interest here the spin Hamiltonian \mathcal{H} takes the following form:

$$\mathcal{H} = \beta \mathbf{H} \cdot \mathbf{g} \cdot \mathbf{S} + \mathbf{S} \cdot \mathbf{D} \cdot \mathbf{S} + \sum_i [\mathbf{S} \cdot \mathbf{A}^{(i)} \cdot \mathbf{I}^{(i)} - g_N^{(i)} \beta_N \mathbf{I}^{(i)} \cdot \mathbf{H} + \mathbf{I}^{(i)} \cdot \mathbf{P}^{(i)} \cdot \mathbf{I}^{(i)}] \quad [2-1]$$

Here \mathbf{H} is the applied magnetic field vector, \mathbf{S} the vector operator for the total unpaired electron spin, and $\mathbf{I}^{(i)}$ the corresponding operator for the i th nucleus. At X-band frequencies (~9.3 GHz), typical ranges of values of the terms are, in order: 9.3 GHz, 0-20 GHz, 1-200 MHz, 1-15 MHz, 0-100 MHz; the physical significances of the individual terms are given below.

2.2 (a) $\beta \underline{H} \cdot \underline{g} \cdot \underline{S}$, the electron Zeeman term, represents the potential energy of the electron magnetic moment, $-\beta \underline{g} \cdot \underline{S}$, in the magnetic field \underline{H} . For a free electron this energy would be simply $g_e \beta \underline{H} \cdot \underline{S}$, where the scalar g_e has the value 2.00232, the Landé factor for a free electron. In practice, the electronic angular momentum is not purely derived from the spin: due to spin-orbit coupling small amounts of orbital angular momentum are mixed in, so that \underline{S} represents an 'effective' or 'fictitious' spin. This admixture of orbital angular momentum causes the effective g-factor to be shifted from its spin-only value, and to vary with the magnetic field direction, since the orbital contributions to \underline{S} are themselves anisotropic. The fact that, for free radicals in the solid state, g approximates the free-spin value is due to 'quenching' of the orbital angular momentum -- its precession in the crystal electric fields so that magnetic interactions are averaged out. Mathematically, this appears as the fact that the eigenvalue of the angular momentum operator L_z , must be zero, because the eigenvalue of any hermitian operator is real, and the orbital must be taken as real, while L_z itself is pure imaginary.

For free radicals the g-shift, $g_{\text{obs}} - g_e$ is generally less than 1% and the quantity \underline{g} , referred to as the g-tensor, is represented by a real 3x3 symmetric matrix (g_{ij}). The elements of \underline{g} are estimated by perturbation theory taking the spin-orbit coupling term $\lambda \underline{L} \cdot \underline{S}$ as a first order perturbation, and for an atom the result for g_{zz} is (62)

$$g_{zz} = g_e - 2\lambda \sum_n \frac{\langle \psi_0 | L_z | \psi_n \rangle \langle \psi_n | L_z | \psi_0 \rangle}{E_n - E_0} \quad [2-2]$$

with similar expressions for the other elements of \underline{g} . The g-factor for a molecule is taken as a sum of atomic terms (56, 62).

The absolute sign of the g-tensor cannot be determined in a conventional EPR experiment, but requires the use of circularly polarised microwaves. Further details of this, together with other implications of this way of writing the electron Zeeman term, and possible exceptions to the formulation are given in References (56, 59).

2.2 (b) $\underline{S} \cdot \underline{D} \cdot \underline{S}$ the electronic spin-spin coupling energy, where \underline{S} is the total spin represents the magnetic interactions between two or more unpaired electrons. The term is zero for doublet states, but can be very large in organic triplet molecules and transition metal complexes. The mechanism of the interaction can be dominated by either spin-orbit coupling (transition metals) or a through-space dipolar interaction (organic triplets and higher multiplets.)

For a suitable choice of axis system the dipolar spin-spin interaction can be written in the form

$$\frac{1}{2} g^2 \beta^2 \left\{ S_x^2 \left\langle \frac{r^2 - 3x^2}{r^5} \right\rangle + S_y^2 \left\langle \frac{r^2 - 3y^2}{r^5} \right\rangle + S_z^2 \left\langle \frac{r^2 - 3z^2}{r^5} \right\rangle \right\} \quad [2-3]$$

where the angular brackets denote a spatial average. This form shows the tensor \underline{D} is traceless since $x^2 + y^2 + z^2 = r^2$. For the spin-orbit coupling mechanism the same result holds and \underline{D} is generally represented by a traceless symmetric tensor.

2.2 (c) $\underline{S} \cdot \underline{A} \cdot \underline{I}$, the hyperfine energy, represents the interaction between the nuclear and electron magnetic moments. Like \underline{g} and \underline{D} , the tensor \underline{A} is usually written as 3x3 symmetric matrix. (See 59). It has two main components.

(a) The dipolar term $\underline{S} \cdot \underline{B} \cdot \underline{I}$ which corresponds to the classical interaction $-\underline{\mu}_1 \cdot [(3\underline{r}\underline{r} - r^2 \underline{U}) r^{-5}] \cdot \underline{\mu}_2$ of two dipoles $\underline{\mu}_1$ and $\underline{\mu}_2$ separated by a

vector \underline{r} . (\underline{U} is the unit dyadic). If both μ_1 and μ_2 are quantised along a common direction, making an angle θ with \underline{r} , the angular variation of the dipolar interaction has the familiar form

$$B' \cdot (3\cos^2\theta - 1) \quad [2-4]$$

where B' is a constant.

The trace of the tensor \underline{B} is proportional to that of $(\underline{u}\underline{u} - (1/3)\underline{U})$ (where \underline{u} is a unit vector parallel to \underline{r}) which is given by

$$(\underline{u}\underline{u} - (1/3)\underline{U}) : \underline{U} = \underline{u} \cdot \underline{u} - 1/3(3) = 0, \quad [2-5]$$

so that \underline{B} is the anisotropic part of \underline{A} .

(b) The isotropic Fermi contact term ' a ' or ' a_{iso} ' corresponds to the interaction between the nucleus and an electron which is inside it, in other words to the overlap of the electronic wave function with the nucleus. The relative size of the latter enables one to approximate the quantity a by

$$a \approx \frac{8\pi}{3} g\beta g_N \beta_N \int \Psi^* \delta(\underline{r}) \Psi d\tau = \frac{8\pi}{3} g\beta g_N \beta_N |\Psi^2(0)|, \quad [2-6]$$

where Ψ is the electronic wave function in question.

For heavy elements where Ψ is 'dense', the finite size of the nucleus may become significant, giving rise to the so-called 'hyperfine anomaly' (60, 61). This is much less than 1% of the total hyperfine interaction in all cases of interest here, and will not be considered further.

The value a is 1/3 of the trace of \underline{A} , so it is easy to separate the two components phenomenologically; their physical interpretations are discussed in a later section.

2.2 (d) $-g_N \beta_N \vec{H} \cdot \vec{I}$, the nuclear Zeeman interaction is the analogue of the electron Zeeman term; the main difference is that nuclear magnetic moments are of the order of $\beta_N/\beta_e = 1/1836$ times the electronic moment, so that the nuclear Zeeman energy is correspondingly smaller. (At X-band frequencies, the electron and proton terms are ca 9.3 GHz and 14 MHz respectively.) As a result, anisotropy in the nuclear g factor is undetectable in normal electron paramagnetic resonance.

2.2 (e) $\vec{I} \cdot \vec{P} \cdot \vec{I}$ the nuclear quadrupole interaction is formally analogous to the electronic spin-spin term; it represents the energy of a non spherical nucleus in an inhomogeneous electric field and is zero if $I < 1$. The tensor \vec{P} is proportional to the nuclear electric quadrupole moment Q and to the gradient tensor of the electric field at the nucleus. If the electric field satisfies Laplace's equation the latter tensor is traceless, and this is generally assumed to hold for \vec{P} . The applicability of this assumption is discussed in References (64, 65).

2.3 The Eigenvalue Problem

To relate the transition fields and frequencies measured in a magnetic resonance experiment to the Hamiltonian parameters discussed above, one needs to solve the eigenvalue equation

$$\mathcal{H}\Psi = E\Psi \quad [2-7]$$

for E and Ψ . The most general method of solution, and the method adopted for the treatment of data described in this thesis, is by numerical diagonalisation of the total spin Hamiltonian matrix \mathcal{H} . In favourable cases the equation may also be solved analytically or by perturbation theory taken to first or second order.

In recent years second order approximations to the eigenvalues of [2-7]

have been given by several authors. (66-70). The results are very complicated in the general case, but contain the interesting feature that tensors such as \underline{g} and \underline{A} occur only in symmetric terms (e.g. $\underline{g}^T \cdot \underline{A}^T \cdot \underline{A} \cdot \underline{g}$) so that any asymmetry in the tensors themselves would not be apparent.

Since these methods are useful for preliminary analysis of data, and offer more physical insight than numerical methods, the next section provides an illustration of their use in solving a relatively simple Hamiltonian.

2.3 (a) EPR Hamiltonian with field along a principal direction ($S=I=\frac{1}{2}$)

We take the Hamiltonian of equation [2-1], with $S=\frac{1}{2}$, $I=\frac{1}{2}$, so that the spin-spin and quadrupole terms do not appear; \underline{g} is taken to be isotropic, and \underline{H} , defining the z axis, is parallel to a principal axis of the A-tensor; the x and y axes coincide with the other principal axes of \underline{A} , so that there are no off-diagonal elements of the hyperfine tensor.

One chooses as a basis in which to express \mathcal{H} the set $|M_S M_I\rangle$ defined by the eigenvalues of S_Z and I_Z ; for $S=\frac{1}{2}$ and $I=\frac{1}{2}$ as here, $m_S=\pm\frac{1}{2}$, $M_I=\pm\frac{1}{2}$, so the states are conveniently denoted by $|++\rangle$, $|+-\rangle$, $| -+\rangle$, $| --\rangle$.

The x and y terms in the Hamiltonian are evaluated using the relations

$$J_+ = (J_x + iJ_y); J_- = (J_x - iJ_y) \quad [2-8]$$

and

$$\langle M_J+1 | J_+ | M_J \rangle = \langle M_J | J_- | M_J+1 \rangle = (J(J+1) - M_J(M_J+1))^{\frac{1}{2}} \quad [2-9]$$

where $J=S$ or I . The resulting Hamiltonian matrix is, with $G=g\beta H$ and $N=-g_N\beta_N H$,

$$\begin{array}{c}
 \begin{array}{cccc}
 & 1++> & 1--> & 1+-> & 1-+> \\
 <++1 & \left[\begin{array}{cccc}
 \frac{1}{2}G + \frac{1}{2}N + \frac{1}{4}A_z & \frac{1}{4}(A_x - A_y) & 0 & 0 \\
 \frac{1}{4}(A_x - A_y) & -\frac{1}{2}G - \frac{1}{2}N + \frac{1}{4}A_z & 0 & 0 \\
 0 & 0 & \frac{1}{2}G - \frac{1}{2}N - \frac{1}{4}A_z & \frac{1}{4}(A_x + A_y) \\
 0 & 0 & \frac{1}{4}(A_x - A_y) & -\frac{1}{2}G + \frac{1}{2}N - \frac{1}{4}A_z
 \end{array} \right] & \\
 <--1 & & & & \\
 <+-1 & & & & \\
 <--1 & & & &
 \end{array}
 \end{array} \quad [2-10]$$

and its eigenvalues E are the solutions of the equation

$$\text{Det}(\underline{H} - E\mathbf{1}) = 0 \quad [2-11]$$

where $\mathbf{1}$ is the 4x4 unit matrix.

The two blocks are solved separately, yielding

$$\begin{aligned}
 E_1 &= \frac{1}{4}A_z + \frac{1}{2}[(G+N)^2 + \frac{1}{4}(A_x - A_y)^2]^{\frac{1}{2}} \\
 E_2 &= \frac{1}{4}A_z - \frac{1}{2}[(G+N)^2 + \frac{1}{4}(A_x - A_y)^2]^{\frac{1}{2}} \\
 E_3 &= -\frac{1}{4}A_z + \frac{1}{2}[(G-N)^2 + \frac{1}{4}(A_x + A_y)^2]^{\frac{1}{2}} \\
 E_4 &= -\frac{1}{4}A_z - \frac{1}{2}[(G-N)^2 + \frac{1}{4}(A_x + A_y)^2]^{\frac{1}{2}}
 \end{aligned} \quad [2-12]$$

To put these in a form useful for other than numerical analysis one has to approximate the square roots according to the conditions normally valid for X-band EPR, viz $N \ll G$, and (slightly less generally) $A_x, A_y \ll G$. A binomial expansion then gives

$$\begin{aligned}
 E_1 &= \frac{1}{4}A_z + \frac{1}{2}(G+N) + \frac{1}{16}(A_x - A_y)^2/G + \frac{1}{64}(A_x - A_y)^4/G^3 \\
 E_2 &= \frac{1}{4}A_z - \frac{1}{2}(G+N) - \frac{1}{16}(A_x - A_y)^2/G - \frac{1}{64}(A_x - A_y)^4/G^3
 \end{aligned}$$

$$E_3 = -\frac{1}{4}A_z + \frac{1}{2}(G-N) + \frac{1}{16}(A_x + A_y)^2/G + \mathcal{O}((A_x + A_y)^4/G^3) \quad [2-13]$$

$$E_4 = -\frac{1}{4}A_z - \frac{1}{2}(G-N) - \frac{1}{16}(A_x + A_y)^2/G + \mathcal{O}((A_x + A_y)^4/G^3)$$

Substituting these results into the original eigenvalue equation gives the eigenfunctions Ψ_i which to the same level of approximation are

$$\begin{aligned} \Psi_1 &\approx \left\{ 1 - \frac{1}{32} \left(\frac{A_x - A_y}{G+N} \right)^2 \right\} |++> - \frac{1}{4} \left(\frac{A_x - A_y}{G+N} \right) |--> \\ \Psi_2 &\approx \left\{ 1 - \frac{1}{32} \left(\frac{A_x - A_y}{G+N} \right)^2 \right\} |--> + \frac{1}{4} \left(\frac{A_x - A_y}{G+N} \right) |++> \\ \Psi_3 &\approx \left\{ 1 - \frac{1}{32} \left(\frac{A_x + A_y}{G-N} \right)^2 \right\} |+-> + \frac{1}{4} \left(\frac{A_x + A_y}{G-N} \right) |-+> \\ \Psi_4 &\approx \left\{ 1 - \frac{1}{32} \left(\frac{A_x + A_y}{G-N} \right)^2 \right\} |-+> - \frac{1}{4} \left(\frac{A_x + A_y}{G-N} \right) |+-> \end{aligned} \quad [2-14]$$

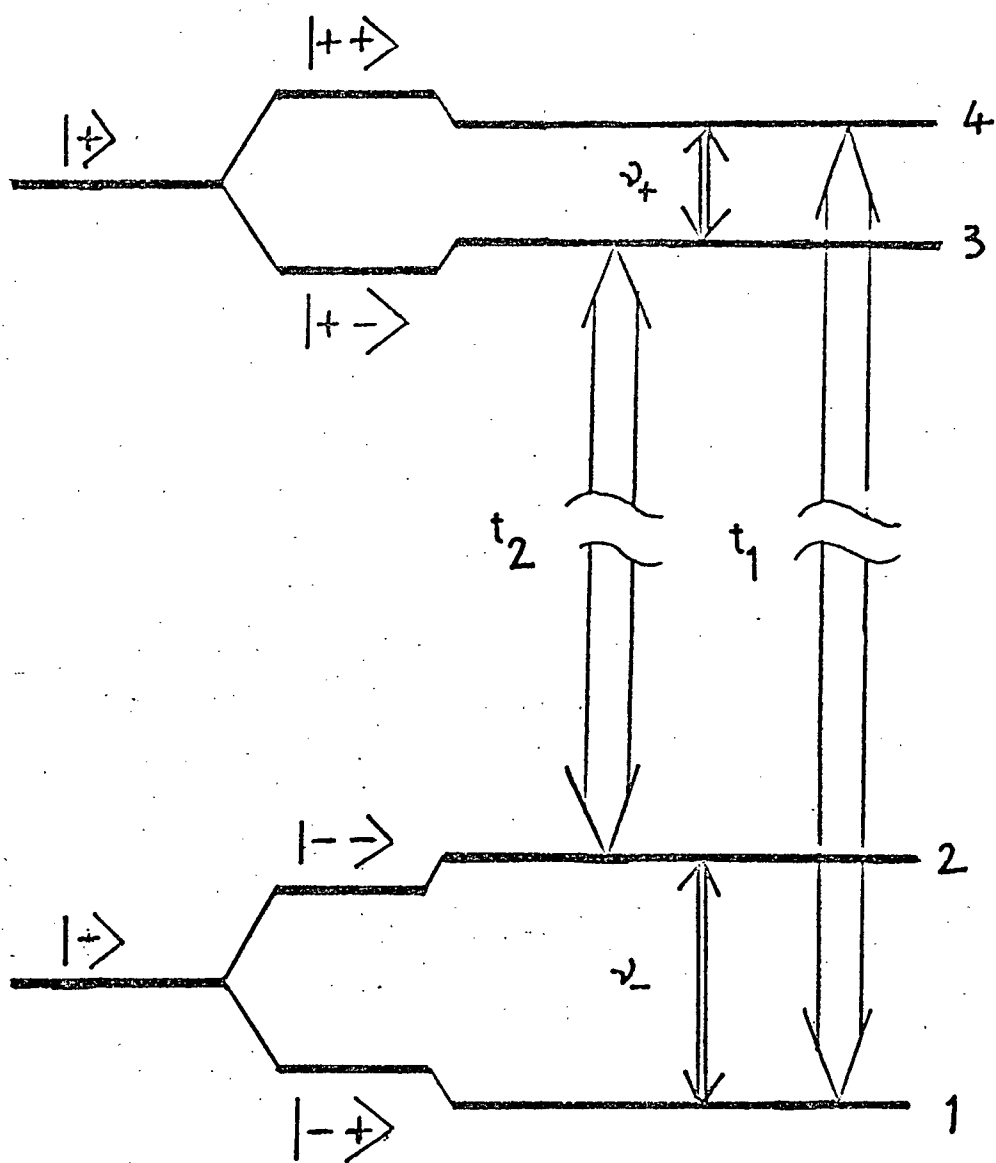
Normally in EPR, transitions are induced by a linearly polarised microwave field producing a time-dependent magnetic field

$$H_1 \cdot \cos 2\pi \nu t.$$

H_1 is usually perpendicular to H and can be taken as being along the x axis, so that it introduces the following time-dependent term in the Hamiltonian

$$g\beta S_x \cdot H_1 \cos 2\pi \nu t - g_N \beta_N I_x H_1 \cos 2\pi \nu t \quad [2-15]$$

When the frequency ν is equal to the energy difference (MHz) between two eigenstates of \mathcal{H} the resonance condition is satisfied and a transition can occur. The corresponding transition probability between states i and j is



$$g\beta H \cdot \tilde{S} + a \tilde{S} \cdot \tilde{I} = g_N \beta_N H \cdot \tilde{I}$$

Fig. 1. EPR and ENDOR transitions for a system with $S=I=\frac{1}{2}$.

$$(4\pi^2/h)H_1^2 |\langle \psi_i | g\beta S_x - g_N\beta_N I_x | \psi_j \rangle|^2 \cdot \delta(h\nu - \Delta E) \quad [2-16]$$

As before, the nuclear term is much smaller than the electronic and can be neglected; a further simplification results if the hyperfine terms in [2-14] are less than about 10% of the Zeeman term, in which case the eigenfunctions ψ_i are approximate eigenfunctions of S_z and the strongly allowed EPR transitions correspond to the selection rule $\Delta M_s = \pm 1$.

The principal EPR transitions are thus

$$t_1 \psi_1 \longleftrightarrow \psi_4 \quad t_2 \psi_2 \longleftrightarrow \psi_3$$

The corresponding energies are $E_1 - E_4$ and $E_2 - E_3$; and the resonance conditions are

$$\nu = E_1 - E_4 \div \frac{1}{2}A_z + G + \frac{1}{8} \left(\frac{A_x^2 + A_y^2}{G} \right) + \dots$$

and

$$\nu = E_2 - E_3 \div -\frac{1}{2}A_z + G + \frac{1}{8} \left(\frac{A_x^2 + A_y^2}{G} \right) + \dots \quad [2-17]$$

In a field-swept experiment N and G will have different values for each transition, so that the corresponding second order terms will make different contributions; this difference however is generally very small and will be neglected. The splitting between the two allowed lines is then (in field units)

$$|G_1 - G_2| = g\beta |H_1 - H_2| = |A_z| \quad [2-18]$$

Similarly the centre of the two lines falls at

$$\frac{1}{2}|G_1 + G_2| = \nu - \frac{1}{8} \left[\frac{A_x^2 + A_y^2}{G} \right] \quad [2-19]$$

which is shifted downfield from the 'g-only' value ($= h\nu/g\beta$) by approximately

$$\frac{1}{8} \left(\frac{A_x^2 + A_y^2}{g\beta H} \right) \quad [2-20]$$

2.3 (b) EPR Hamiltonian with field in a general direction

The main limitation of this discussion has been the assumption that \underline{H} lies along a principal axis of \underline{A} , in which case as shown by equation 2-17 above, the nuclear Zeeman term makes an undetectable contribution to the observed spectrum. One consequence of this is that it is very hard to determine even the relative signs of the principal values of the hyperfine tensor. This remains true if we relax the condition on the direction of \underline{H} , but still require $\underline{S} \cdot \underline{A} \cdot \underline{I} \gg g_N \beta_N \underline{H} \cdot \underline{I}$, as the following analysis illustrates.

We take the electronic Zeeman term as the zero order Hamiltonian and evaluate the first order corrections ϵ due to the nuclear terms.

A useful device is the 'effective field approximation' in which one regards the nuclear spin \underline{I} as experiencing an effective magnetic field $\underline{H}_{\text{eff}}$ defined by

$$-g_N \beta_N \underline{H}_{\text{eff}} \cdot \underline{I} \equiv \underline{S} \cdot \underline{A} \cdot \underline{I} - g_N \beta_N \underline{H} \cdot \underline{I} \quad [2-21]$$

In the EPR case now considered, the hyperfine term predominates and for this one makes the first order substitution

$$\underline{S} \cdot \underline{A} \approx m_s \underline{h} \cdot \underline{A} \quad [2.22]$$

where \underline{h} is the unit vector along which \underline{S} is quantised. ($\underline{h} = \underline{H}/|H|$), or a little more generally,

$$\tilde{h} = \tilde{H} \cdot \tilde{g} / (\tilde{H} \cdot \tilde{g} \cdot \tilde{g} \cdot \tilde{H})^{1/2}, \quad [2-23]$$

for $\tilde{S} \cdot \tilde{A} \cdot \tilde{I} \ll g\beta H$.)

The eigenvalues of I in this effective field are

$$-g_N \beta_N |\tilde{H}_{\text{eff}}| m_I \pm m_S (\tilde{h} \cdot \tilde{A}^2 \cdot \tilde{h})^{1/2} m_I \quad [2-24]$$

and I now obeys the selection rules $\Delta m_I = \pm 1$. The resulting hyperfine pattern consists of $2I+1$ lines separated by $(\tilde{h} \cdot \tilde{A}^2 \cdot \tilde{h})^{1/2}$, from which one can determine only the tensor \tilde{A}^2 . The principal values of \tilde{A}^2 are the squares of those of \tilde{A} so that all information concerning the signs of the latter has been lost.

2.3 (c) Introduction of Nuclear Zeeman Term - 'Forbidden' Transitions

When \tilde{A} becomes comparable to the nuclear Zeeman energy the situation becomes more complicated and one must diagonalise the full nuclear Hamiltonian [2-21], to an appropriate level of approximation at least.

Since the requirement that $\tilde{S} \cdot \tilde{A} \cdot \tilde{I} \sim g_N \beta_N H \ll g\beta H$ implies a small \tilde{A} , a first order treatment is again adequate, and the eigenfunctions of [2-21] are approximate eigenfunctions of S_z . The nuclear Hamiltonian is now

$$m_S \tilde{h} \cdot \tilde{A} \cdot \tilde{I} - g_N \beta_N \tilde{H} \cdot \tilde{I} \quad [2-25]$$

If the eigenvalue of this Hamiltonian is ϵ , it can be shown⁽⁷²⁾ that, for negligible g-anisotropy, the corresponding eigenfunctions have the form

$$\begin{aligned} \phi_i = & \frac{2\epsilon - A_{zz} m_S + \nu p}{[(2\epsilon - A_{zz} m_S + \nu p)^2 + (A_{xz}^2 + A_{yz}^2) m_S^2]^{1/2}} |m_S^{+>} \\ & + \frac{(A_{xz} m_S - i A_{yz} m_S)}{[(2\epsilon - A_{zz} m_S + \nu p)^2 + (A_{xz}^2 + A_{yz}^2) m_S^2]^{1/2}} |m_S^{->} \end{aligned} \quad [2-26]$$

with $\nu_p = g_N \beta_N H$.

This expression shows that if the static field direction (z axis) is along a principal axis of \underline{A} , or if A_{zz} is either much larger or much smaller than $\nu_p/2$ then there is no mixing of nuclear spin functions. But in the general case, mixing of the nuclear spin states allows other transitions among the four energy levels and gives rise to four EPR lines.

The expression for ϵ is most simply evaluated using the effective field approximation used above, and turns out to be

$$\begin{aligned} \epsilon_{m_S, m_I} &= [m_S^2 \hbar^2 \underline{A}^2 \cdot \underline{h} - 2m_S g_N \beta_N H \hbar \underline{A} \cdot \underline{h} + (g_N \beta_N H)^2]^{1/2} m_I \\ &= [\frac{1}{4} \hbar^2 \underline{A} \cdot \underline{A} \cdot \underline{h} \cdot \underline{h} + g_N \beta_N H \hbar \underline{A} \cdot \underline{h} + (g_N \beta_N H)^2]^{1/2} m_I, \end{aligned} \quad [2-27]$$

with as above, $\underline{H} = H \underline{h}$. Note that ϵ is now not linear in m_S .

In general, one cannot expand the square root in a rapidly convergent series, so that the transitions between levels of different m_S value occur at energies which bear no simple relation to the magnitude of the hyperfine tensor. Furthermore ϵ is typically of the order of $|A_{zz}/2 \pm \nu_p|$ so that the wavefunctions can vary rapidly with magnetic field strength and the orientation of the A-tensor.

The resulting EPR spectrum consists of two pairs of lines of strongly varying intensity and complex dependence on the hyperfine parameters. (72)

Such spectra are very difficult to analyse. Methods involving the use of second moments have been suggested (73); the extra information one obtains is the tensor \underline{A} itself rather than \underline{A}^2 . Although the global sign of the tensor cannot be determined in this way, the relative signs of the principal values are fixed by the interaction with the nuclear Zeeman term,

and make it possible for instance to determine the absolute value of the contact interaction unambiguously.

The success of these methods is limited by the resolution available in a solid state EPR experiment where the linewidth, typically 1-10 MHz, is often comparable to the hyperfine couplings to be measured.

2.3 (d) ENDOR Transitions

At this point ENDOR can provide a major simplification of the analysis. Postponing for a moment consideration of the ENDOR experiment itself, we may view the technique as an investigation of the energy levels of the nuclear Hamiltonian [2-21] within a given m_S multiplet. In general a spin- $\frac{1}{2}$ nucleus will give rise to two ENDOR transitions, denoted by ν_+ and ν_- , corresponding to transitions within the two electronic multiplets. (See Fig. 1). The nuclear resonance condition is satisfied when

$$\nu_{\pm} = \epsilon_{m_S m_I} - \epsilon_{m_S m'_I} \quad [2-28]$$

where

$$|m_I - m'_I| = 1 \quad [2-29]$$

so that

$$\nu_{\pm} = \left(\frac{1}{4} h \cdot A^2 \cdot h + g_N \beta_N H h \cdot A \cdot h + (g_N \beta_N H)^2 \right)^{\frac{1}{2}} \quad [2-30]$$

Thus the observed frequencies are now related relatively simply to the

components of the hyperfine tensor. If $I > \frac{1}{2}$, there will be $2I$ transitions corresponding to $\Delta m_I = \pm 1$ within each m_S multiplet; to first order these nuclear transitions will be degenerate if the quadrupole interaction is absent. Figure 2 illustrates this for the case of $I = 3/2$.

If h rotates within a single co-ordinate plane, then a plot of ν^2 against field orientation (for constant field strength and zero quadrupole interaction) has the form

$$\nu^2 = a \cos^2 \theta + b \sin^2 \theta + c \sin^2 \theta, \quad [2-31]$$

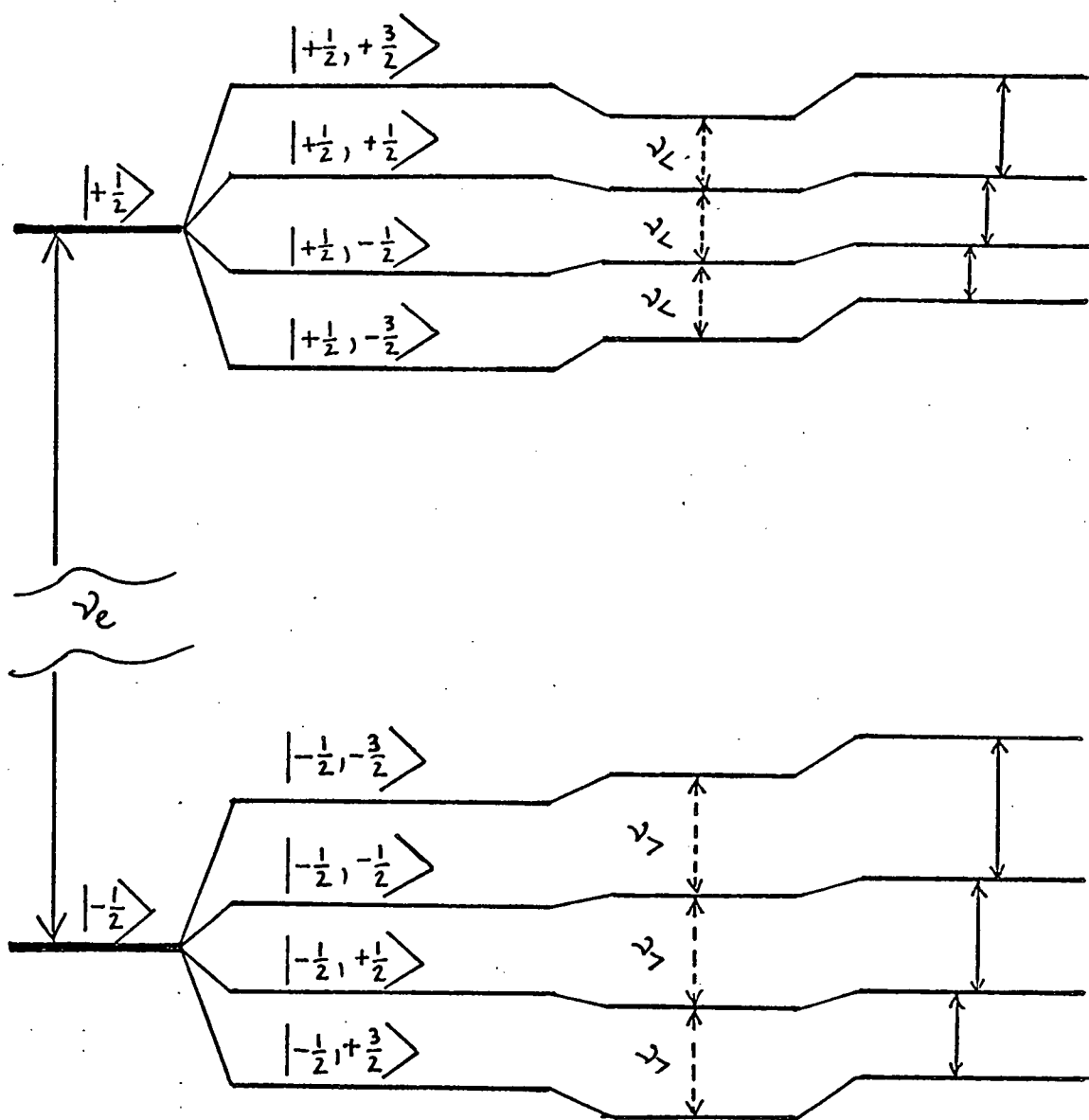
a simple result which is very useful for the preliminary analysis of data; the constants a, b, c are elements of the tensor $(\nu_{p \pm \frac{1}{2}} U \pm \frac{1}{2} A)^2$.

The second order corrections are of order $A^2/4G$; the ENDOR line width is ~ 30 kHz, so this first order treatment is adequate for $a \leq 40$ MHz, when $H = 3300$ G, and within this range of coupling constants three further useful results can be derived.

Firstly it follows directly from [2-30] that

$$\frac{\nu_+^2 - \nu_-^2}{2g_N \beta_N H} = -\hbar \cdot A \cdot \hbar \quad [2-32]$$

In practice one cannot assign the m_S values absolutely so that ν_+ and ν_- are usually interpreted as the high and low frequency transitions respectively; observation of both transitions thus gives a simple method of determining A to within a sign.



$$g\beta H m_S + a' m_S m_I - g_N \beta_N H m_I + P' m_I^2$$

Fig. 2. First order ENDOR transitions for a system with $S=1/2$, $I=3/2$. In the absence of a quadrupole interaction, the three transitions labelled $\nu_{>}$ are degenerate in first order.

Secondly, if A is small compared to $\nu_p U$, the square root in the expression for ν_{\pm} can be expanded in a binomial series. If all but the first two terms are negligible the ENDOR lines are symmetrically placed about $\nu_p = |g_N \beta_N H|$. The same result is obtained when A is isotropic: if A is replaced by $a U$, the expression for ν_{\pm} immediately reduces to $|\nu_p \pm a/2|$. In a solid matrix, the proliferation of small couplings from weakly coupled nuclei usually gives the ENDOR spectrum a characteristic symmetry about ν_p and serves as a convenient means of field calibration. If a is larger than $2\nu_p$ the two ENDOR lines are separated by $2\nu_p$ and fall symmetrically about $a/2$.

Thirdly, by expanding the expression for ν_{\pm} as a Taylor series in $\Delta\nu_p = g_N \beta_N \Delta H$, one can show that when $a < 2\nu_p$, to a reasonable approximation, the separation of the ENDOR lines is unchanged by small variations in H , so that observed ENDOR frequencies can be corrected to a constant field value by applying shifts equal in magnitude to the change in NMR frequency. This is useful in plotting the angular dependence of ENDOR lines when the static field is varying.

Within the range of g -values normally encountered in free radicals, the ENDOR frequencies calculated above are independent of the magnitude of the electronic g -tensor. However, the relative anisotropy of g can produce a small first order effect on ν_{\pm} by changing the quantisation axis of S . This point is discussed in Appendix 1.

The above analysis has assumed throughout that m_S is (approximately) a good quantum number. If the spin Hamiltonian contains other terms which are comparable to $g\beta H$ this will not be true. Examples are the hyperfine interaction of an arsenic nucleus (74) or the effect of a large D -tensor (75); in these cases m_S must be replaced by the expectation value $\langle S_z \rangle$ which in general will differ from 0.5 and will vary from state to state; this

phenomenon has been used to determine the relative signs of the 'ENDOR' coupling and the larger tensor, and has been extended to the case of two moderate and comparable proton couplings (76).

2.3 (e) ENDOR intensities

To evaluate the ENDOR transition moment one needs second order wave functions. These are very difficult to obtain analytically for the general case, but have been given by Kwiram (33) and Iwasaki et al (67), and a simple calculation for a special case was presented in 1966 by Whiffen (71). The important consequences are that the ENDOR transition moment increases with the ENDOR frequency, and varies with the magnitude of the A-tensor and its orientation with respect to the static field. As will appear in the next section, the ENDOR intensity also depends, but in no simple way, on the relaxation characteristics of the paramagnetic system. For these reasons, calculation or simulation of solid state ENDOR spectra has rarely been attempted. The paper by Dalton and Kwiram (33) is a notable exception.

2.4 NMR experiments in Paramagnetic Systems

Before we turn to the ENDOR experiment itself, it is instructive to consider the results of a simple NMR experiment on a similar system. Figure 3 shows the energy level diagram for a system with $S=\frac{1}{2}$, $I=\frac{1}{2}$. In the absence of induced transitions, the spin system will be in thermal equilibrium with the lattice, and spin-lattice relaxation will maintain a population difference between each pair of levels; the ratio of populations will follow the Boltzmann distribution,

$$N_1/N_2 = \exp(-\Delta E/kT) , \quad [2-33]$$

where ΔE is the energy difference between the two levels. For X-band experiments, the exponentials may be replaced by $1 - \Delta E/kT$; this is an excellent approximation at 300K or 77K, and remains adequate for the present purpose at 4.2K. The separation of levels connected by EPR transitions is ca. 9.3 GHz, while the nuclear levels 1 and 2, 3 and 4 are separated by a 14 MHz. Thus the population differences across the nuclear levels are $\sim 10^{-3}$ of the electronic values, and this is reflected in the relative intensities of the two types of transition.

In the diamagnetic system the NMR sensitivity would also be limited by the long spin-lattice relaxation times which cause saturation at low power. In a paramagnetic system, this limitation is greatly reduced since the fluctuating fields due to the relaxing electrons enhance the nuclear relaxation rates.

As a result of this, the NMR line is considerably broadened, and except at very low temperatures the nuclei see only a time-averaged hyperfine interaction given by $\langle m_S \rangle \hbar \cdot \mathbf{A} \cdot \mathbf{I}$, where $\langle m_S \rangle$ is the time average expectation value of the S_z operator for the electron interacting with a given nucleus. $\langle m_S \rangle$ differs from zero only because of the Boltzmann distribution of populations in the $m_S = \pm \frac{1}{2}$ levels. At X-band frequencies and a temperature of 77K $\langle m_S \rangle \sim 10^{-3}$, so that the effect of a hyperfine coupling even as large as 50 MHz will be only to shift the NMR resonance by ~ 50 KHz from the free proton frequency. In many cases this will be only a few linewidths so that the relative resolution, shift/linewidth, is quite low.

An order-of-magnitude estimate of the relative EPR and NMR sensitivities in such a paramagnetic system can be obtained as follows. The output voltage produced by a typical spectrometer has the form

$$\Delta V = Q \chi'' \zeta V$$

where Q is the quality factor of the resonant cavity or circuit, ζ the filling factor, V the applied voltage, which is proportional to the oscillating field H_1 , and χ'' is the imaginary part of the susceptibility (63). A Bloch Equation treatment (58) gives

$$\chi'' = \frac{1}{2} \frac{\omega_0 T_2 \chi_0}{(1 + T_2^2 (\omega - \omega_0)^2 + T_1 T_2 \gamma^2 H_1^2)} \quad [2-35]$$

where T_2 is the spin-spin relaxation time, $\gamma = g\beta/\hbar$ and χ_0 is given by the Curie-Law expression

$$\chi_0 = \frac{Ng^2 \beta^2 J(J+1)}{3kT}, \quad J = S \text{ or } I. \quad [2-36]$$

For simplicity we consider the amplitude of an absorption mode signal at the centre of the resonance, $\omega = \omega_0$, and to take account of the variation of transition probability with magnetic moment, we evaluate the maximum signal as a function of H_1 , giving the signal strength limited by saturation. ΔV is proportional to $\chi'' H_1$, and this function has a maximum when $T_1 T_2 \gamma^2 H_1^2 = 1$.

Substitution of this into [2-35] leads to the relation

$$\frac{\Delta V_{\text{EPR}}}{\Delta V_{\text{NMR}}} = \frac{\chi_{\text{OE}}}{\chi_{\text{ON}}} \left(\frac{T_{2e}}{T_{1e}} \frac{T_{1N}}{T_{2N}} \right)^{\frac{1}{2}}, \quad [2-37]$$

where the term ω_0/γ has been cancelled since it is equal to H which is assumed to be the same for both systems. From [2-36] $\chi_{\text{OE}}/\chi_{\text{ON}} \propto (v_e/v_N)^2 \approx 4 \times 10^5$; and T_{2e}/T_{2N} can be replaced by the ratio of reciprocal linewidths, typically ~ 200 , with the result that

$$\frac{\Delta V_{\text{EPR}}}{\Delta V_{\text{NMR}}} \approx 3 \times 10^4. \quad [2-38]$$

This estimate neglects the difference in nuclear and electronic

spin lattice relaxation times, but in practise NMR experiments could be carried out at higher fields than EPR so that the increased value of ω_0 would partially compensate for the ease of saturation.

As it stands this rough calculation shows why NMR in paramagnetic systems is a very difficult experiment, and to obtain detailed measurements of hyperfine interactions a more sophisticated technique is needed, using the sensitivity of the electronic absorption.

2.5 The ENDOR Experiment

Now we consider what happens if one of the EPR transitions (say $2 \leftrightarrow 3$) is induced and the microwave power increased until saturation occurs. The original population difference between these two levels is reduced and can be brought close to zero, at which point the EPR signal amplitude will fall to a low value. In practice to achieve effective microwave saturation usually requires lowering the sample temperature to 77 K or 4.2K, when most relaxation processes will be inhibited. In this case the population difference between levels 1 and 2 or 3 and 4 will be increased from δ to ϵ (see Figure 3). A source of radio-frequency radiation is now scanned until the resonance condition for one of the hyperfine transitions is satisfied; when this is achieved a large absorption of energy occurs, tending to return the populations of the spin states to their thermal equilibrium values, and desaturating the electron resonance. This increase in the original EPR signal as a result of an induced nuclear transition is called an ENDOR enhancement; the experimental procedure involves monitoring the intensity of the saturated transition while the rf oscillator is scanned through the hyperfine frequencies. Experimentally it is often found that the strongest ENDOR signals are obtained when the EPR signal is only slightly saturated -- within ca 3dB of the microwave power producing

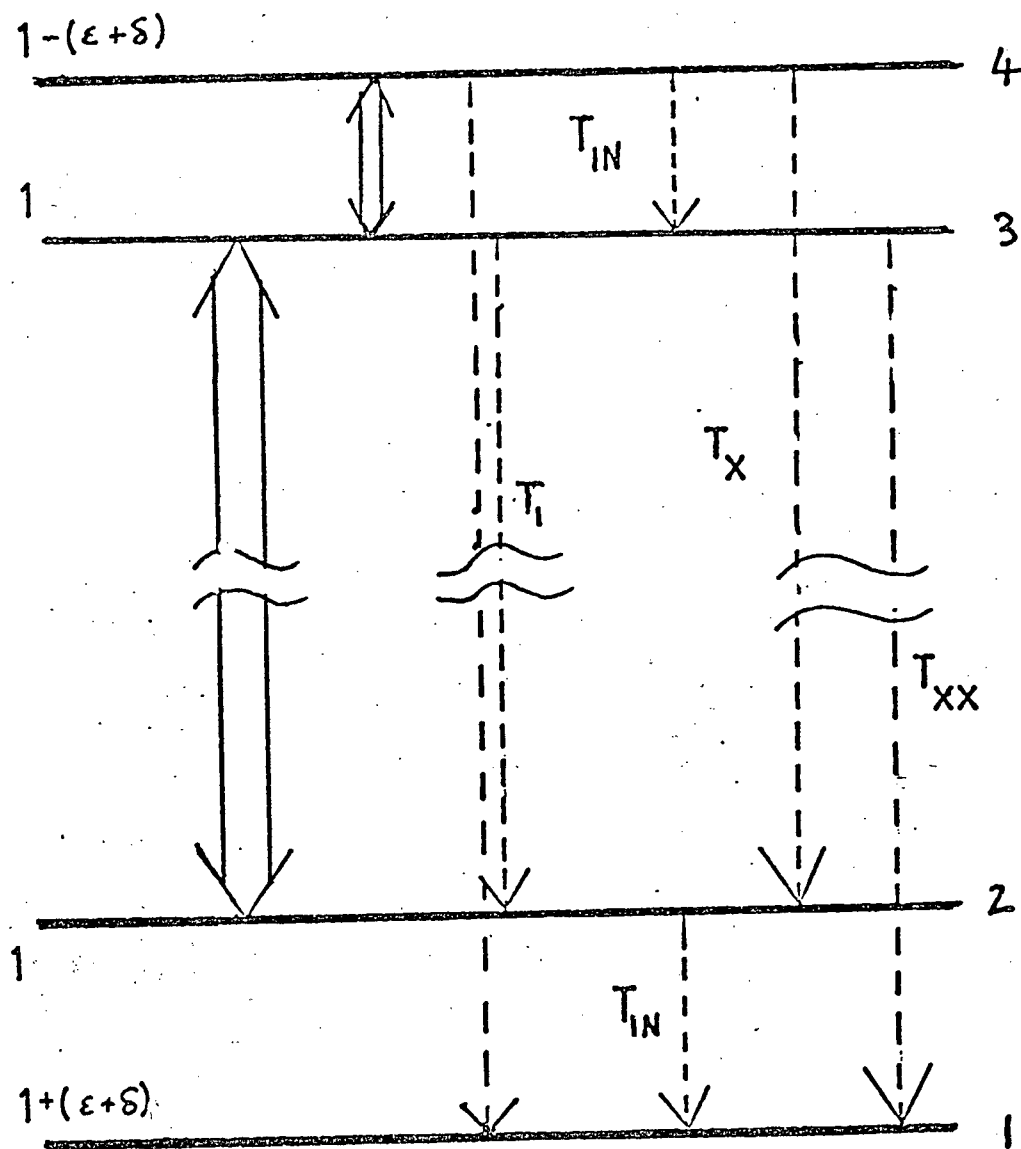
the maximum signal. (40, 78)

This discussion has been basically qualitative because it is very difficult to give a general description of the ENDOR mechanism which is quantitatively useful. But one can discuss some of the other factors involved in the ENDOR mechanism as follows.

The ENDOR enhancement arises from two main mechanisms, only one of which is specific to the double resonance experiment; this first process is the increase in effective nuclear Boltzmann factor, and the removal of nuclear relaxation times as a limit on the signal strength. The second mechanism is more subtle and arises from the hyperfine interaction (50, 51) The electronic magnetisation will follow the total magnetic field given by $H + H_{rf}$, since the latter varies much more slowly than the electron Larmor frequency; the resulting hyperfine field experienced by the nucleus will thus have a transverse component varying at the same frequency as the applied rf. The sum of these two oscillating fields induces the nuclear transitions; this sum may be zero if the two effects cancel, in which case ENDOR will be unobservable. If the two fields add, the resultant may be much greater than H_{rf} alone and lead to an enhanced transition rate for the same power.

This is the physical basis of the variation of ENDOR intensity with ENDOR frequency mentioned above. In practice to take full advantage of this one needs to match the impedance of the rf coil to that of the amplifier over the range of the frequency scan.

One instrumental factor should also be mentioned: a microwave cavity equipped for ENDOR will have a quality factor of the order of 2000; the corresponding value for a conventional NMR coil will be closer to 100, so the use of an EPR signal to detect NMR in this way has a further advantage. This too is related to the higher frequency of the EPR experiment.



$$2\epsilon = \nu_e/kT$$

$$2\delta = \nu_p/kT$$

Fig. 3. Relaxation pathways for a system with $S=I=\frac{1}{2}$. T_1 and T_{IN} are the electronic and nuclear spin lattice relaxation times respectively. T_X and T_{XX} represent cross-relaxation processes. The open arrows represent allowed EPR and ENDOR transitions, and the values at the left are the relative populations of the four levels when the EPR transition is saturated.

A full treatment of ENDOR mechanisms and intensities has not been developed for several reasons. In general one cannot usefully abstract a two-spin system from the ensemble of nuclei and paramagnetic centres. There are other relaxation pathways such as those in Figure 3 denoted by T_{1N} (nuclear spin-lattice relaxation), and the cross relaxation routes T_x and T_{xx} , which may be induced by the interactions between neighbouring paramagnetic centres. Note that T_x and T_{xx} correspond to forbidden transitions.

These routes should be included, together with other magnetic interactions with the lattice. In fact the existence of other relaxation routes than T_1 is essential for a conventional ENDOR experiment. In the simple model discussed above, in which one EPR transition was saturated and T_1 was the only significant relaxation process, inducing a single NMR transition would merely redistribute the populations of the levels and allow the EPR signal to saturate again in a time $\sim T_1$. In the absence of other relaxation processes only a transient ENDOR signal would be observed.

One aspect of these other interactions is the polarisation of distant nuclei. This has its origin in a solid state effect, by which the nuclei are polarised in the EPR levels undergoing saturation. This polarisation can diffuse to 'distant' nuclei in the lattice and give rise to a 'distant ENDOR' or 'matrix ENDOR' line. (79)

Further complications arise due to contributions from the dispersion mode of the EPR signal, and from passage effects due to modulation and a finite scan rate. In particular, field and frequency modulations often produce markedly different spectra in the region of the free proton NMR frequency.

Occasionally the effects of some of these mechanisms have been studied using the theory of electrical networks, with the radio-frequency

transition acting as a 'short' by decreasing the effective T_1 . The method has been applied to a study of Tm^{2+} ions in CaF_2 (80), but in general the resulting equations are very complicated and contain several quantities which are very hard to determine. Their application has been limited mainly to double resonance experiments in the liquid phase. (81)

In sum, ENDOR intensities are typically 10^{-2} of the corresponding EPR intensities; this represents a gain of about two orders of magnitude over the NMR values for the same system. The linewidths however are comparable to the values that would be obtained by NMR and constitute an improvement on EPR resolution by a factor of $1-5 \times 10^2$.

2.6 Relation of Hyperfine Coupling Tensors to Electronic Structure

Since the bulk of the work described in Chapters 4 and 5 is devoted to the interpretation of measured hyperfine parameters, this section surveys the means by which such parameters are related to the electronic structure of a paramagnetic centre.

In all cases this is via the spin density distribution $\rho(\underline{r})$ - the excess of a α spin over β spin at a point \underline{r} - which may be defined by

$$\rho(\underline{r}) = \langle \Psi | \sum_k \delta(\underline{r} - \underline{r}_k) 2S_{z_k} | \Psi \rangle \quad [2-39]$$

where the sum runs over all electrons. ρ is often used to mean the total spin on an atom or in an orbital, in which case the form of ρ given above must be integrated over the orbitals in question; the term spin density although conventional, is then not really appropriate since what is referred to is a fraction of the total spin rather than a volume density.

In many cases the spin distribution is adequately represented by a single molecular orbital consisting of a linear combination of atomic orbitals (LCAO):

$$\psi = \sum_i c_i \phi_i \quad [2-40]$$

In this case the spin density in the i^{th} orbital is simply c_i^2 , and the spin density on a given atom is of the form $\sum_k c_i^2$ where k runs over the orbitals

centred on the atom in question. McConnell (85), proposed an 'atomic' delta function as the spin density operator, which gives a generalisation of this result. An advantage of this simple formulation is that it lends itself to the direct interpretation of experimental results. Given the measured hyperfine constants a_i and the corresponding values a_i^0 for unit spin, one obtains simply,

$$|c_i| = (a_i/a_i^0)^{1/2} \quad [2-41]$$

The single LCAO description can give only positive values for ρ ; a more sophisticated model will incorporate spin polarisation (or more generally electron correlation effects) due to the exchange interactions between electrons and will lead to negative spin densities at some points. A simple case of this is provided by the McConnell relation which is discussed below.

2.6 (a) Isotropic Couplings

As discussed above, the Fermi contact interaction is proportional to the value of ψ^2 evaluated at the nucleus. The expression

$$\int \psi \delta(\underline{r}-\underline{r}_i) \psi d\tau = \sum_{i,j} c_i c_j \int \phi_i \delta(\underline{r}-\underline{r}_i) \phi_j d\tau \quad [2-42]$$

will be dominated by the one centre term corresponding to orbitals centred on nucleus i , since the amplitude of an atomic orbital decreases almost exponentially with distance. In this approximation only s-orbitals will give rise to a contact interaction, since all higher orbitals have nodes at the nucleus: the isotropic part of the hyperfine tensor is thus a measure of the s-orbital spin density.

For atoms other than hydrogen the main use of these spin densities is in the calculation of hybridisation ratios and the prediction of geometry using p-orbital spin densities and the Coulson relationship (82).

For hydrogen atoms there is an important simplification because the gap between the $n=1$ and $n=2$ electronic energy levels is $\sim 10\text{eV}$ or 230kcal/mole , which means that essentially only the $1s$ orbital is available for bonding. Thus the s -orbital spin density of a hydrogen atom is directly related to the amount of covalent bonding to the paramagnetic centre. This has been applied to studies of hydrogen bonding where the separation of covalent and ionic contributions to the total bond is otherwise very difficult (83).

2.6 (b) The McConnell Relationship

The above discussion is quite adequate for systems of σ symmetry, but for species which approximate π symmetry other effects must be included. On a simple model the H-atoms of an aromatic π radical should show no hyperfine couplings since they lie in the nodal plane of the spin distribution. The observed couplings, often of the order of 30MHz , are much too large to be the result of out-of-plane vibrations of the hydrogen atoms (84): the couplings in fact result from spin polarisation.

An empirical relation

$$a = Q\rho_{\pi} \quad [2-43]$$

had been proposed, relating the observed proton isotropic coupling a to the π -electron density on the nearest carbon atom. McConnell and Chestnut (85) showed that this relation could be derived semiquantitatively from Valence Bond, Molecular Orbital or Unrestricted Hartree Fock Theory.

The simplest qualitative description is in terms of the exchange interaction which favours the proximity of antiparallel spins for electrons in orthogonal orbitals. See Fig. 4.

The prediction of all these models is that positive spin at the carbon will induce negative spin at the proton, and this was confirmed by

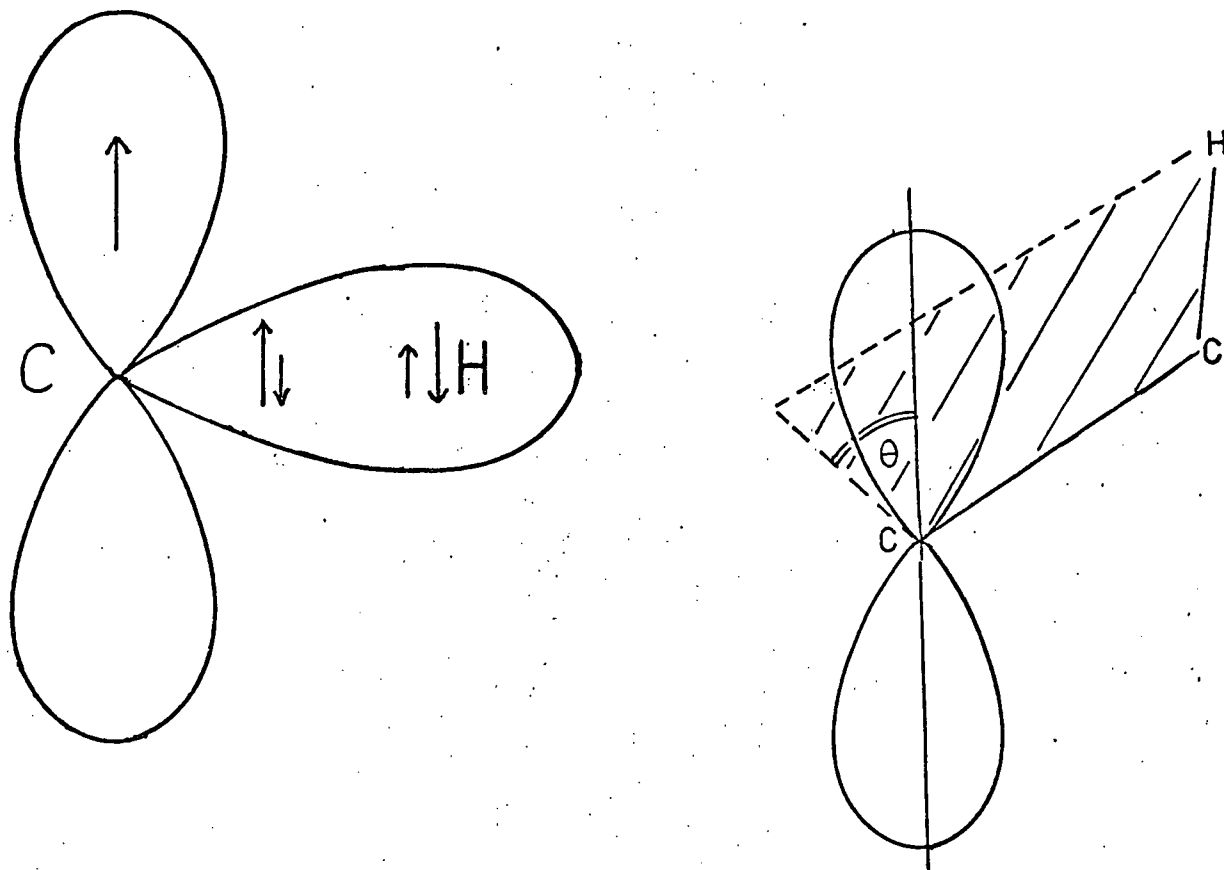


Fig. 4. (a) Schematic representation of isotropic couplings induced by σ - π polarisation. The arrows denote the relative amounts of α and β spin.
 (b) Dihedral angle θ used in calculating β proton couplings.

measurements of NMR contact shifts (86).

Similar relations hold for N-H bonds, and have been proposed with varying degrees of success for one centre ^{13}C and ^{14}N interactions, and for C-F bonds.

Several attempts have been made to generalise the McConnell relationship.

Colpa and Bolton (87) suggested the formula

$$a = Q_1\rho + Q_2\varepsilon\rho \approx Q_1\rho + Q_2\rho^2, \quad [2-44]$$

where ε is the charge in the C-H bond:

Giacometti, Nordio and Pavan (88), suggested

$$a = Q_1\rho + Q_2(\rho_2 + \rho_2') \pi$$

where ρ_2 and ρ_2' are the π spin densities on neighbouring carbon atoms.

Both equations were derived for aromatic radical ions, and the values of Q_2 change sign with the sign of the ion, so the applications to neutral radicals is not obvious. Melchior (89) has given a critical account of these and other forms in his study of the problem.

In practice the simple McConnell relationship is almost invariably used to obtain π electron spin densities, the value of Q being chosen empirically, in the range -60 to -80 MHz.

2.6 (c) β -Proton Couplings

The ethyl radical $\cdot\text{CH}_2\text{CH}_3$ can be regarded as a π radical with a substituent methyl group; the McConnell relation will explain the methylene (α) proton hyperfine interactions, but not the equally large methyl (β) couplings. Their origin cannot be σ - π polarisation as described above because of the C-C bond between the hydrogens and the spin on the methylene carbon. Instead hyperconjugation or the overlap of the π spin density with the C-H bonds is postulated (90, 92). The form of the interaction involves

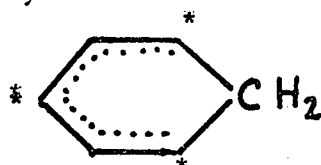
the exchange or overlap integral between the $2p\pi$ orbital containing the unpaired electron and the s-p hybrids comprising the C-H bonds; it leads to the semi-empirical relationship.

$$a = \rho(B_0 + B_1 \cos^2 \theta) \quad [2-45]$$

where θ is the dihedral angle between the π direction and the C-H bond as shown in Figure 4(b). The isotropic parts of the β proton couplings have been quite successfully interpreted using this formula with $B_0 = -9$ MHz and $B_1 = 122$ MHz.

Recently Maruani et al (93, 94) have given more general expressions and Kwiram et al (95) have discussed the physical interpretation of the two non-observables polarisation and overlap spin densities.

The cyclohexadienyl radical



has two β protons in a methylene group; in this case the formula becomes more complicated because there are now two centres of spin density β to the hydrogens. Bersohn (96) had derived expressions for the β couplings in semiquinone ions and Whiffen (97) showed that his results explained the unexpectedly large β couplings in cyclohexadienyl. Bersohn's formula showed that in this case $\rho(=c^2)$ would be replaced not by $(c_1^2 + c_2^2)$ but by $(c_1 + c_2)^2$. For cyclohexadienyl, $c_1 = c_2$, so the result, $4c^2$, is twice the expected spin density.

Examination of Bersohn's formula suggests that in the general case with $c_1 \neq c_2$ the relation [2-45] would have the form

$$a = (c_1 + c_2)^2 \cdot (B_0 + B_1 \cos \theta_1 \cos \theta_2)$$

Now, however, B_0 and B_1 themselves will be functions of the geometry since

this determines the hybridisation at the methylene carbon. Numerical results by Morukuma et al confirm this (98).

2.6 (d) Anisotropic Couplings

One-Centre terms

For the one-centre terms the unpaired electron is in a p or higher orbital centred on the magnetic nucleus itself, and the tensor \underline{B} is given by

$$\underline{B} = \mu_e \mu_N \langle \phi | \underline{\mathcal{O}} | \phi \rangle \quad [2-46]$$

where μ_e and μ_N are the respective electronic and nuclear moments, $\underline{\mathcal{O}}$ is the dipolar operator $(3\underline{u}\underline{u}-\underline{1})/r^3$. As an example we can take $\phi=2p_z$ which transforms as the vector \underline{z} ; \underline{B} takes its simplest form if \underline{u} is a unit vector along \underline{z} , in which case we have

$$B_{zz} = \mu_e \mu_N (3-1) \langle r^{-3} \rangle = 2 \langle r^{-3} \rangle \mu_e \mu_N \quad [2-47]$$

$$B_{xx} = \mu_e \mu_N (0-1) \langle r^{-3} \rangle = - \langle r^{-3} \rangle \mu_e \mu_N = B_{yy}$$

and all other terms are zero.

Thus \underline{B} is axial for the interaction with a p orbital; in many cases, depending on the magnitude of other terms in the Hamiltonian, the resulting angular variation of the anisotropic coupling has the form

$$B'(3\cos^2\theta - 1)$$

This point is discussed in more detail in Appendix 2.

One centre terms often dominate the dipolar tensors of heavier elements, but make no contribution to those of hydrogen atoms due to the absence of available p-orbitals.

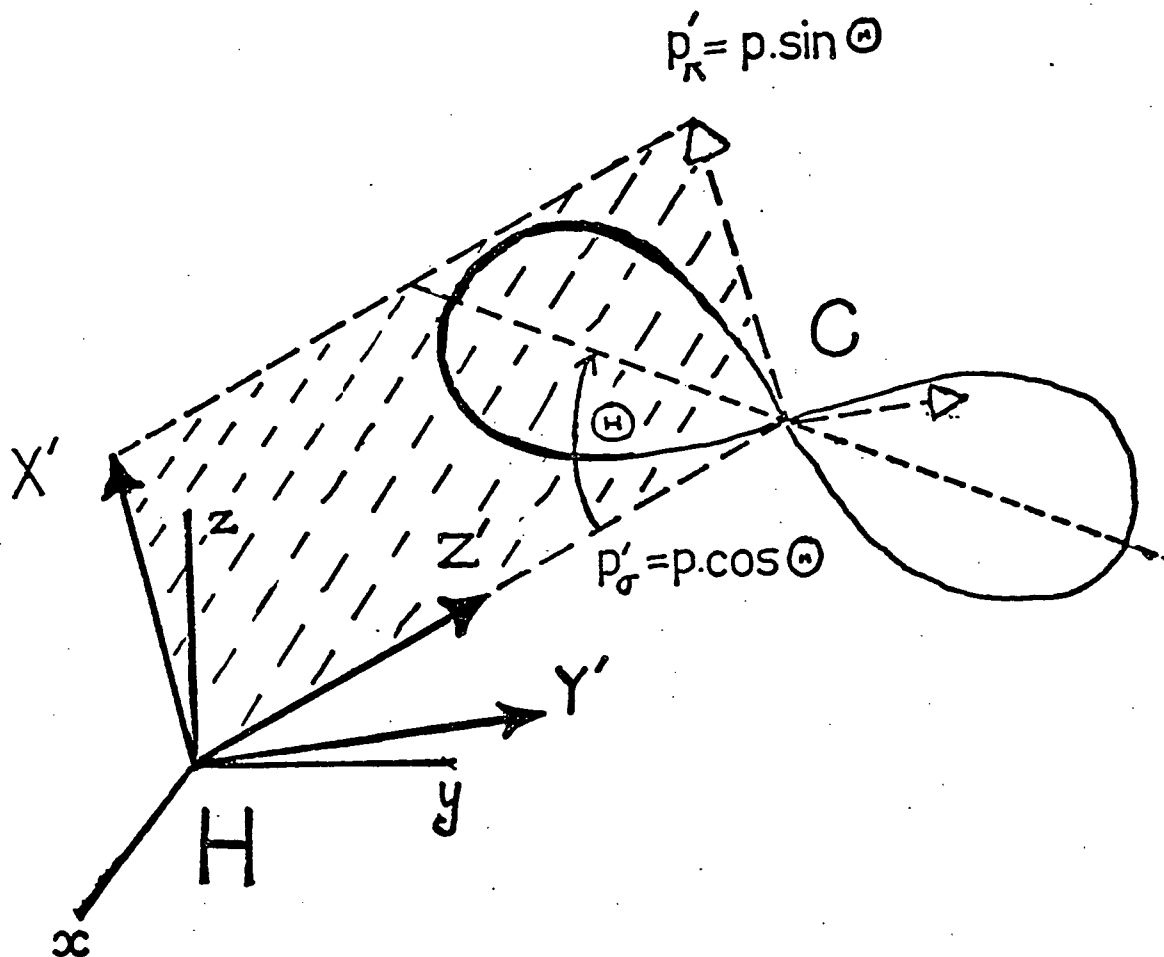


Fig. 5. Coordinate system used in McConnell-Strathdee calculations. The $X'Z'$ plane contains the axis of the p-orbital, and Z' is the internuclear direction.

2.6 (e) Multicentre Terms

These are the only source of anisotropy in proton hyperfine couplings, but are correspondingly less important for other elements. The two centre terms are usually sufficient and are considered first.

For these one has to evaluate the expectation value

$$\langle \phi^{(1)} | \mathcal{O}^{(2)} | \psi^{(1)} \rangle$$

where now ϕ and ψ have a common centre, different from that of \mathcal{O} . McConnell and Strathdee (99) originally tackled this problem for the case of a magnetic nucleus interacting with spin in a 2s or 2p Slater orbital; for the 2p case the internuclear vector was taken to be either in the nodal plane or along the axis of the p orbital (π and σ cases respectively).

Expanding the expression for ψ as a sum of Legendre polynomials, they were able to give expressions for the elements of \underline{B} in terms of the quantity $a=2rz$ where r is the internuclear separation and z is the effective nuclear charge or orbital exponent of the Slater orbital.

Pitzer et al (100) extended the results, including terms from δ -functions omitted in the original calculations. Corresponding expressions for $3p_{\pi}$ orbitals were derived recently (102). Barfield (101) has given a complete set of formulae for $\phi, \psi=1s, 2s, 2p_{\pi}, 2p_{\sigma}$.

For example if z is the bond direction

$$\begin{aligned} \langle 2p_y | \theta_{zy} | 2s \rangle = \langle 2p_x | \theta_{xz} | 2s \rangle = -(\frac{1}{2}\sqrt{3})R^{-3} \{ 15a - \\ [4a^4 + 10a^3 + 20a^2 + 30a + (15/a)] e^{-2a} \} . \end{aligned} \quad [2-48]$$

$$\langle 2s | \theta_{zz} | 2s \rangle = R^{-3} [1 - ((4/9)a^5 + (2/3)a^4 + (4/3)a^3 + 2a^2 + 2a + 1) e^{-2a}] . 2 \quad [2-49]$$

2.6 (e) Multicentre Terms

These are the only source of anisotropy in proton hyperfine couplings, but are correspondingly less important for other elements. The two centre terms are usually sufficient and are considered first.

For these one has to evaluate the expectation value

$$\langle \phi^{(1)} | \mathcal{O}^{(2)} | \psi^{(1)} \rangle$$

where now ϕ and ψ have a common centre, different from that of \mathcal{O} . McConnell and Strathdee (99) originally tackled this problem for the case of a magnetic nucleus interacting with spin in a 2s or 2p Slater orbital; for the 2p case the internuclear vector was taken to be either in the nodal plane or along the axis of the p orbital (π and σ cases respectively).

Expanding the expression for ψ as a sum of Legendre polynomials, they were able to give expressions for the elements of \underline{B} in terms of the quantity $a=2rz$ where r is the internuclear separation and z is the effective nuclear charge or orbital exponent of the Slater orbital.

Pitzer et al (100) extended the results, including terms from δ -functions omitted in the original calculations. Corresponding expressions for $3p_{\pi}$ orbitals were derived recently (102). Barfield (101) has given a complete set of formulae for $\phi, \psi=1s, 2s, 2p_{\pi}, 2p_{\sigma}$.

For example if z is the bond direction

$$\begin{aligned} \langle 2p_y | \theta_{zy} | 2s \rangle &= \langle 2p_x | \theta_{xz} | 2s \rangle = -(\frac{1}{2}\sqrt{3})R^{-3} \{ 15a - \\ &[4a^4 + 10a^3 + 20a^2 + 30a + (15/a)]e^{-2a} \} . \end{aligned} \quad [2-48]$$

$$\langle 2s | \theta_{zz} | 2s \rangle = R^{-3} [1 - ((4/9)a^5 + (2/3)a^4 + (4/3)a^3 + 2a^2 + 2a + 1)e^{-2a}] . 2 \quad [2-49]$$

All the integrals have the general form of an R^{-3} variation at large distances (corresponding to a point dipole interaction) modified by more complicated variation at short distances.

As long as the total dipolar interaction can be represented as a sum of two centre terms, these formulae can be used to evaluate the interaction at a given nucleus for any geometrical arrangement of 2s and 2p orbitals. This follows because an unpaired electron distribution given by, say, $c_x 2p_x + c_y 2p_y$ can be represented by the single term $(c_x^2 + c_y^2)^{1/2} 2p'$, where $2p'$ is the 'vector sum' of the x and y terms. $2p'$ itself can then be resolved into σ and π components.

Using this approach theoretical estimates of this dipolar coupling tensors can be made as described below; the method is that of the author's program Dipole which was used in the interpretation of the data presented in Chapters 4 and 5.

Since both the main radicals studied here were of simple π or σ symmetry it was sufficient to include only one 2s and one 2p orbital per atom. The distribution of spin density in CO_2^- also means that for both systems the all p-orbitals can be taken as parallel.

The spatial co-ordinates of the magnetic nucleus in question are read in together with those of all the atoms contributing spin density and the corresponding orbital exponents. The spin distribution is represented by the coefficients c_s and c_p of the s and p orbitals on each atom, and the total dipolar tensor is estimated as a sum of two-centre terms, as follows.

The vector between the magnetic nucleus and the i th atom is taken as the z-axis of a local co-ordinate system and the p orbital on atom i is resolved into π and σ components

$$p = p_\sigma \cos\theta + p_\pi \sin\theta \quad [2-50]$$

where θ is the angle between this z' -axis and the axis of the p-orbital as shown in Fig. (5).

The six terms such as

$$c_s c_p \langle 2s | \theta | 2p_\pi \rangle \cos \theta, \quad c_p^2 \langle 2p_\pi | \theta | 2p_\sigma \rangle \sin \theta \cos \theta$$

are now evaluated using Barfield's equations and summed to give the total contribution of atom i.

The resulting tensor is transformed into the original or 'lab' frame using the transformation given by Derbyshire (92); the contributions from other atoms are evaluated in the same way and added up in the lab. frame. Finally the total tensor is diagonalised to facilitate comparison with experiment.

2.6 (f) Three Centre Terms

Three centre terms are of the form,

$$B_z = \mu_N \mu_e \langle \phi^{(1)} | \theta^{(2)} | \psi^{(3)} \rangle \quad [2-60]$$

with ϕ , θ and ψ all on different centres. These terms are generally small since the integrand is significant only if ϕ and ψ have appreciable overlap in the neighbourhood of centre 2. The three centre integrals can be expressed in terms of two centre terms by Mulliken's approximation (103)

$$\langle \phi^{(1)} | \theta^{(2)} | \psi^{(3)} \rangle \approx \frac{1}{2} \langle \phi^{(1)} | \psi^{(3)} \rangle [\langle \phi^{(1)} | \theta^{(2)} | \phi^{(1)} \rangle + \langle \psi^{(3)} | \theta^{(2)} | \psi^{(3)} \rangle]. \quad [2-61]$$

Higher terms are generally undetectable.

2.6 (g) Applications

The theoretical importance of the anisotropic coupling tensor is

threefold. Firstly, the elements of B_z are proportional to c^2 (or, for cross terms, to the quantity $c_1 c_2$), so that the magnitude of the coupling can provide an estimate of the spin density distribution which is independent of the McConnell relation.

Secondly, it is a source of geometrical information. For π radicals two extreme cases are of most interest. For small r , as in the 'classic' C-H fragment only one centre of spin density is significant, and the principal values of the dipolar tensor approximate $(b, 0, -b)$ and the first two principal directions respectively define the bond and the axis of the p orbital. In general, whether or not the radical has π symmetry, the most positive principal value will correspond to the bond direction. The other extreme is the case of large r , when the spatial extent of the orbitals becomes insignificant and the interaction approaches that of two point dipoles; B_z is then axial and the largest principal value corresponds to the inter-dipole direction. This is useful in identifying the protons responsible for intermolecular couplings; and, if the spin density on the paramagnetic centre is known, the magnitude of the coupling can be used to estimate r .

Thirdly, if the sign of the spin density is known, as is usually the case, the form of the dipolar tensor determines the sign of the total coupling tensor. This is one of the few ways of determining the sign of A_z for small couplings.

Chapter 3

EXPERIMENTAL

3.1 ENDOR Spectrometer

The spectrometer used for the ENDOR measurements has been described in full elsewhere (78): the main features of the instrument together with a few modifications are given below, and summarised in Figure 6.

The spectrometer is built around an X-band EPR spectrometer and is capable of operating in either the homodyne or superheterodyne modes. Almost invariably, however, experiments at the usual temperatures of 77K or 4.2K require the use of such low microwave powers that the resulting afc instability and noise levels make homodyne operation impracticable. All the results reported here were obtained using the superheterodyne mode.

In this case single sideband detection is employed with an intermediate frequency of 30MHz.

The klystron frequency is stabilised by a Microwave Systems Inc. Model MOS-1 frequency synchroniser. Initially this frequency is matched to the resonant frequency of the microwave cavity, but is held constant thereafter, to an accuracy of a few kHz over a period of hours. If the cavity frequency drifts due to changes in temperature as the rf heating varies during a scan, the mis-match of frequencies will cause the noise level to rise. At 4.2K

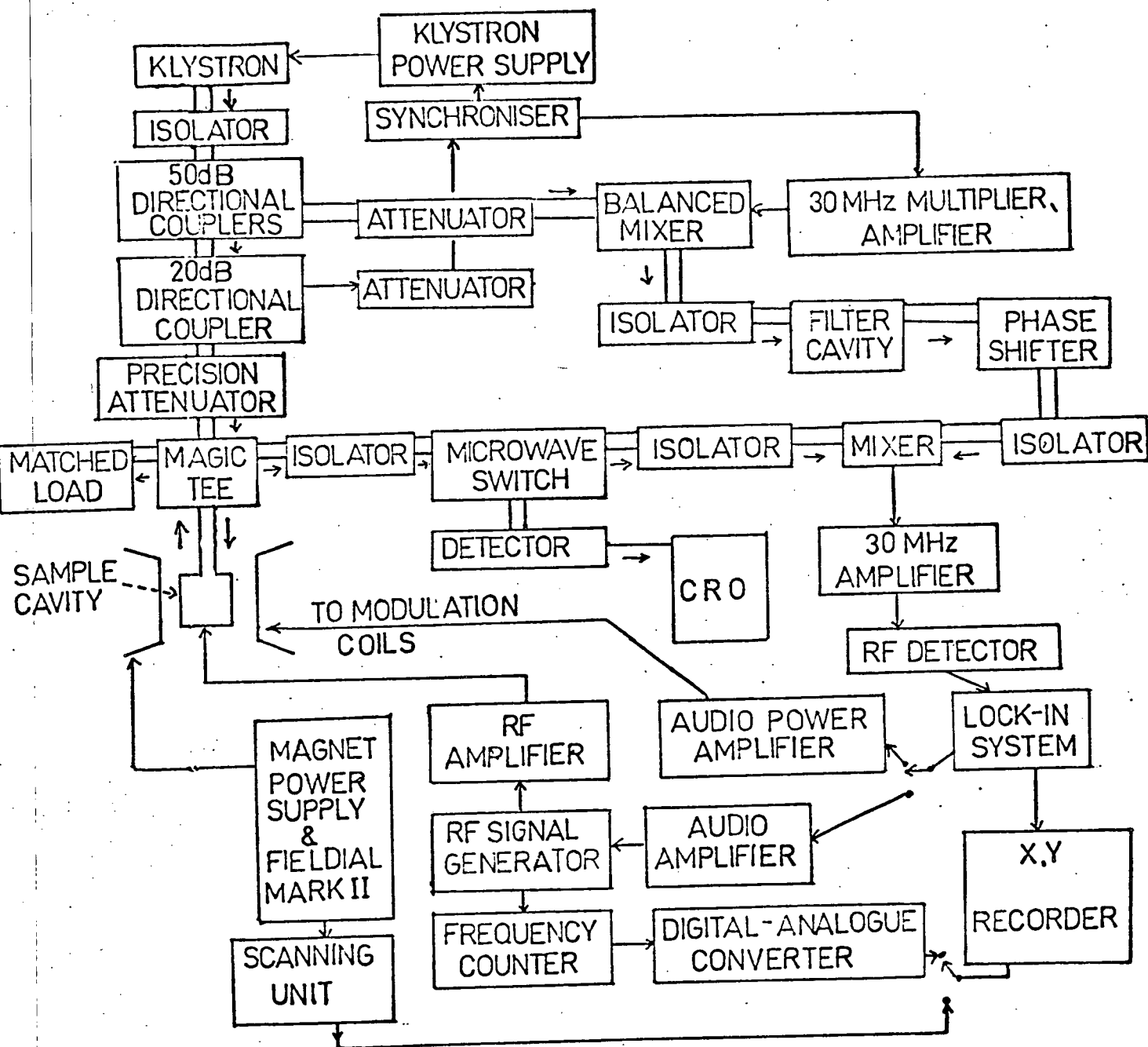


Fig. 6. Block diagram of ENDOR spectrometer.

this may need continual attention, but at 77K occasional adjustment of the fine tuning control on the synchroniser is sufficient to compensate for the drift.

The main branch of the microwave power at the carrier frequency is led through a series of microwave attenuators via a Magic T bridge to the cavity.

Two types of cavity were used. Both were rectangular, operating in the TE_{011} mode and were fitted with 3-turn coils of copper wire to produce the rf field; they differed in the position of the rf coils. In either case the crystal to be studied is mounted against the cavity wall beneath the rf coil. Vacuum grease is the usual adhesive. In one designated 'bottom mounting' the coil was on the cavity floor, so that the rf field at the sample is in the same plane as the rotation of the static magnetic field. In the 'side mounting' cavity, the rf coil is on the side end wall, so that the field it produced at the sample is vertical and thus always perpendicular to the static field. This end plate is removable and held by brass screws; as a result the cavity Q is somewhat reduced, but this is compensated by the greater ease and accuracy of mounting samples within the cavity.

Reflected microwave power from the cavity is led through the third arm of the Magic T to a balanced detector; it is detected at 30MHz, amplified, and passed to a PAR model 121 lock-in amplifier, for processing. The output from this amplifier is used to provide the Y-drive of a Hewlett Packard Moseley 7005A X-Y recorder. The X-drive is provided by either the field sweep from the Fieldial for EPR spectra, or by a signal generated by the frequency sweep for ENDOR. (See below)

Rf power for ENDOR is provided by an ENI Model 320L wideband amplifier rated at 25W for a 50 ohm load. For low frequency ENDOR measurements a

IP1 Model 500 amplifier was used in conjunction with low-pass filters.

The impedance of the rf load is not matched to the amplifier over the whole frequency range and optimum signals are given in the range 10-20 MHz; at higher frequencies the matching can be improved by suitable choice of connecting cables. The frequency sweep is provided by a Marconi TR1066B11 signal generator replaced by a Marconi-type 2002AS rf oscillator for frequencies below ~8 MHz, part of the output of which is fed to a Hewlett-Packard 5326C frequency counter driving a Hewlett-Packard HP 580A digital-analogue converter, which provides the X-drive of the X-Y recorder. In normal use the d-a converter scans modulo 10MHz in steps of 10kHz; this provides a limit on the resolution of the system, which is considerably less than the ENDOR linewidth in all cases encountered.

Frequency modulation is applied to the rf carrier by the lock-in amplifier, driving a Hewlett-Packard HP 450A amplifier, the output of which is fed to the Marconi oscillator.

The magnetic field is provided by a Varian rotatable electromagnet with 9" polepieces, controlled by a Mark II Fieldial. Magnetic field modulation was produced by modulation coils wound on the polepieces. The modulation coils were driven from the reference frequency output of the PAR lock-in after suitable power amplification; modulation frequencies were typically ~300 Hz at 77K and 50 Hz at 4.2K. The resonance mode of the cavities used means that for either cavity at a magnet orientation given by $\theta=0^\circ$, the static and microwave fields are parallel and the allowed EPR transitions become very weak. Also, when the bottom-mounting cavity is used, the static field becomes parallel to the rf field when $\theta=\pm 90^\circ$, so that ENDOR transitions become weak. Effective ranges of magnetic orientation are thus $\pm(20^\circ-90^\circ)$ for the side-mounting and $\pm(20^\circ-75^\circ)$ for the bottom-

mounting cavity.

The last half-metre of waveguide and the microwave cavity are enclosed in two concentric pyrex dewars. For low temperature operation the outer dewar contains liquid nitrogen, and the inner either liquid nitrogen or liquid helium. The cavity itself is cooled by conduction through a closed copper tube immersed in the liquified gas, designated to prevent the latter from entering the cavity.

A temperature of 4.2K has the advantage of producing a high Boltzmann factor, and a high cavity Q due to increased conductivity. On the other hand the system is then more sensitive to changes in temperature caused by rf heating; also, the boiling helium is a source of noise, and has to be replenished after about 2 hours if maximum rf power is used.

At 77K the nitrogen in the inner dewar is quiescent and will last indefinitely if the outer dewar is kept full. The effect of a lower Boltzmann factor is mitigated by the greater relaxation rates which permit a higher fm carrier frequency to be used. In general, operation at 77K is the more convenient alternative and most of the measurements described here were made at this temperature.

3.2 EPR Measurements

EPR spectra were obtained using a Varian E-3 spectrometer operating at X-band frequencies.

3.3 Field and Frequency Calibration

For EPR microwave frequencies were measured with a Hewlett-Packard 5245L frequency counter fitted with a plug-in unit HP5255A. Magnetic field strength was measured using home-made proton NMR probes containing glycerol.

The calibration points were reproducible to about 0.2kHz or less than 0.1G.

For ENDOR the radio-frequency was measured using the X-Y recorder trace as described above. Frequency markers were either added by hand after each spectrum had been run, or were included at 1MHz intervals by an automatic pip-marker built in the UBC Chemistry Department electronics shop.

Magnetic fields were calibrated using the symmetry of the proton ENDOR spectrum in the vicinity of the free proton NMR frequency. This frequency could generally be located to within 5kHz. Independent field calibration would provide slightly greater accuracy, but the greater inconvenience is rarely justified, particularly as an external field probe can measure only the field outside the cavity, while the ENDOR spectrum reflects the field strength at the sample itself. In a few cases small shifts in the value of H were made to optimise the ENDOR signal and their magnitudes were estimated from the calibration of the Fieldial.

The calibration of EPR or ENDOR transition fields or frequencies achieved by fitting the positions of the frequency markers to a quadratic expression, and using this function to interpolate the line positions. A least-squares fitting routine written by Dr. J.A. Hebden for a Monroe 1656 programmable desk calculator was used for this.

For ENDOR data at least 5 calibration points were fitted for each spectrum and the fit reproduced the frequencies of the calibration markers to within 5kHz; the quadratic term in the fitted expression was very small.

3.4 ENDOR Experiments

To obtain ENDOR, first an EPR signal was obtained; a point was selected on this spectrum, and the field scan and modulation were switched off.

Microwave power was increased to 18-20 dB below the 300mW output of the klystron. This power level was a compromise between the requirements of saturation at 77K and the noise produced in the superhet. detection. The radiofrequency amplifier was scanned until an ENDOR signal was seen, usually near 14 MHz, and then modulation frequency, lock-in phase, microwave power, and field strength were all optimised using the observed signal. Once established the optimum conditions were found to be quite reproducible from day to day.

A detailed study was not made, but in general the strongest ENDOR signals were obtained by saturating the centre of a given EPR line; for CO_2^- centres in irradiated sodium formate, a shift of 1-2 G produced as much as 50% change in the ENDOR intensity.

In most cases the achievement of a reasonable signal-to-noise ratio required an fm amplitude at least comparable to the ENDOR linewidth. The fm deviations used were 30kHz for the strong lines in the range 12-16 MHz, increasing to 80kHz at higher frequencies where the intensities were smaller and the lines less closely spaced. The fm carrier frequency was chosen on the basis of a maximum signal-to-noise ratio and was 1 kHz for sodium formate and 3kHz for potassium hydrogen bisphenylacetate at 77K; at 4.2K the carrier frequency was ~500Hz.

3.5 Irradiation Units

X-irradiation was carried out using a Machlett OEG-60 X-ray tube operating at 40kV, 40mA. Ultraviolet irradiation was carried out using either a Bausch and Lomb SP-200 or a Hanovia 679A high pressure mercury lamp. UV irradiation at low temperatures was carried out in a pyrex dewar fitted with quartz irradiation windows; the sample temperature was maintained by

either filling the dewar with liquid nitrogen or mounting the crystal on a copper rod cooled by conduction.

3.6 Sample Preparation

Sodium Formate

Commercial Reagent Grade NaHCO_2 (Eastman Kodak) was used and crystals were grown by slow evaporation of saturated aqueous solutions at room temperature. The crystals formed as colourless plates ca $0.5 \times 0.5 \times 0.1$ cm. in size and elongated along the (101) direction. (See Chapter 4) They were heated at $\sim 120^\circ \text{C}$ for about 20 minutes before irradiation to remove traces of moisture, and stored in a desiccator. Essentially similar spectra were obtained from samples not heated before irradiation.

Uv irradiation produced no change in the appearance of the crystals for any of the dosages used. After X-irradiation, however, the crystals were pale yellow in colour. This colouration increased slightly with time or on heating, but diminished after uv irradiation, and seems to be correlated with the presence of a second radical. (See Appendix 4)

Potassium Hydrogen Bisphenylacetate (KHBP)

Phenylacetic acid (Eastman Kodak) was crystallised from distilled water by evaporation at room temperature. Following the method of Smith and Speakman (107) weighed quantities of this were taken with $\frac{1}{4}$ -molar proportions of potassium carbonate (Malinkrodt 'Analar') and heated in ethanol until the potassium carbonate had dissolved. Evaporation and cooling of this solution yielded colourless platelets of KHBP, melting at 143°C . (Literature value 142°C (107)). Micro-analysis gave:

calculated for $\text{KC}_{16}\text{H}_{15}\text{O}_4$ C 61.9% H 4.9%

found: C 61.8 ± 0.3 H $5.1 \pm 0.3\%$. .

The platelets were dissolved in ethanol and larger crystals were obtained by slow evaporation at room temperature. These formed as colourless plates ca $1 \times 0.5 \times 0.1$ cm in size; smaller crystals ($0.5 \times 0.5 \times 0.1$ cm) were cut from these and used in the subsequent experiments.

On X-irradiation crystals of KHBP became slight brown in colour, with a slight reflective sheen. There was no apparent change in their appearance after 1-2 months' storage at room temperature; but over 6-7 months the crystals gradually became pale yellow in colour. Changes in the EPR and ENDOR spectra of X-irradiated crystals of KHBP were apparent on a time scale of the order of two weeks. Initially 1 hour's irradiation was used, but radical decay on storage became apparent in the course of the ENDOR measurements and a further $\frac{1}{2}$ hour's irradiation was necessary to complete the study.

3.7 Data Analysis

ENDOR data were taken in three orthogonal planes by rotating the magnet in intervals of 2.5° , 5° , or 10° depending on the density of lines.

3.7(a) Preliminary Analysis

In general the lines were very closely spaced and often overlapped so it was necessary to use a preliminary fitting procedure to pick out data points corresponding to a given tensor. A few points were selected visually and used to identify further points.

The preliminary fit was to the function given in equation [2-31] and used a least-squares fitting algorithm developed by the author and modified by Dr. J.A. Hebden who programmed it for the Monroe 1656.

If the relative anisotropy of the term $(\frac{1}{2}A + \nu_{\text{p}} U)$ is small, expansion

of the square root in [2-30] shows that the expression [2-31] reduces to simpler form

$$\nu = a' \sin^2 \theta + b' \sin 2\theta + c' \cos^2 \theta$$

and this form was used for the small couplings in sodium formate. For the KHBP analysis, the full form of [2-] was used, and for highly anisotropic tensors a value of 10000 MHz^2 was added to all ν^2 values before fitting, to minimise the preferential weighting of high frequency lines. This procedure shifts all ν^2 values equally but does not distort the angular variation.

3.7(b) Determination of Hyperfine Parameters

The extraction of Spin Hamiltonian parameters from experimental data was performed using the least squares fitting program LSF (108) written by Drs. J.R. Dickinson and J.A. Hebden, for an IBM 370/168 Computer.

For this program the values of S and I are read in, together with the nuclear magnetic moment and the other elements of the Spin Hamiltonian [2-] where these are non-zero. The values of these parameters can be treated either as fixed quantities or as initial guesses at values to be determined. For ENDOR the electronic g-tensor was put in the first category and in both studies was taken to be isotropic. (See Appendix 1). The hyperfine tensor was the only quantity refined in the ENDOR studies, but in the studies of uv-irradiated sodium formate both \underline{A} and \underline{g} were refined.

The experimental data are read in as a series of observed transition frequencies, with the corresponding fields strengths and directions. The latter can be defined by either two polar angles or a set of Euler angles. The Euler angle option was chosen here as it leant itself more easily to the correction of misalignments of the data planes. (See below)

For each value and orientation of H, the total spin Hamiltonian is

diagonalised numerically; the transition frequencies are calculated and compared to the experimental values, and the resulting set of residuals is used to make a first order correction to the parameters to be refined according to the least squares criterion. The whole process is cycled until the errors and parameters remain constant.

In general the initial guess at the required parameters need be accurate only to within an order of magnitude and convergence is achieved within 5 iterations.

It should be emphasised that the six independent elements of \underline{A} or \underline{g} , for instance, are refined separately, so that no assumption is needed about the magnitude or direction of any of the tensors.

The program FIELDS (109) written by Dr. J.A. Hebden was also used as a diagnostic device. This program is an inverse of LSF in the sense that it uses input Hamiltonian parameters to calculate transition fields or frequencies.

Like LSF it is based on a numerical diagonalisation of the Spin Hamiltonian, with no mathematical approximations. For the calculation of ENDOR frequencies, the appropriate field strength is read in and the difference between the specified energy eigenvalues gives the required transition. For field calculations at a given transition frequency, the input field is taken as an initial guess; the correction to the Hamiltonian from terms in $(H_{\text{True}} - H_{\text{Initial}})$ is treated as a perturbation taken to 7th order and used to refine the guess, and this process is cycled to convergence.

3.8 CNDO/INDO Calculations

CNDO and INDO calculations were performed on an IBM 370/168 computer using the program of Pople and Beveridge (110), obtained through the Quantum Chemistry Program Exchange.

3.9 Crystal Alignment

A well-formed crystal can be mounted quite accurately on the cavity wall with a suitable edge or face parallel to the cavity side. A pair of vernier calipers made a useful 'collimating slit' for this purpose and the estimated uncertainty is less than 2° . This is of the same order as the misalignments in the waveguide and cavity construction itself.

For large couplings the ENDOR frequency may vary by more than 100kHz per angular degree, so misalignments of this size could cause significant errors. However the symmetry of the crystal enables such errors to be estimated and approximate corrections made.

Both the crystals studied here had C2/c symmetry with 4 molecules per unit cell. An orthogonal axis system \underline{a} , \underline{b} , \underline{c} was used in each case, with $\underline{c}^* = \underline{a} \times \underline{b}$. The resulting spectra show two sites in the \underline{ab} and \underline{bc}^* planes (becoming degenerate in \underline{ac}^* and at the \underline{b} -axis), corresponding to two tensors $\underline{T}^{(1)}$ and $\underline{T}^{(2)}$ related by

$$T_{\alpha\alpha}^{(1)} = T_{\alpha\alpha}^{(2)} \quad \alpha = a, b, c^*$$

$$T_{ab}^{(1)} = -T_{ab}^{(2)} ; \quad T_{bc^*}^{(1)} = -T_{bc^*}^{(2)} ; \quad T_{ac^*}^{(1)} = T_{ac^*}^{(2)} .$$

In Appendix 3 expressions are derived for the transformation of $\underline{T}^{(1)}$ and $\underline{T}^{(2)}$ by a rotation matrix \underline{R} , when the rotations are small. In this case \underline{R} is approximately diagonal and rotations about the three axes commute and can be treated independently.

Such rotations relate the tensors $\underline{A}^{(1)}$ and $\underline{A}^{(2)}$ observed in the actual planes of observation to the true values $\underline{T}^{(1)}$, $\underline{T}^{(2)}$ which would be obtained by measurements in the true \underline{ab} , \underline{bc}^* and \underline{ac}^* planes.

In what follows $\underline{a}, \underline{b}$ and \underline{c}^* are taken to mean the pseudo $\underline{a}, \underline{b}, \underline{c}^*$ directions in the actual data planes.

A misalignment of \underline{ac} will cause a splitting of the lines; this was not observed in the KHBP study. A misalignment of the other two planes will shift the crossover points of the lines from $\underline{T}^{(1)}$ and $\underline{T}^{(2)}$. However, to first order in R_{ij} the crossover frequency is unshifted and allows comparison to be made of a given axis in two planes, provided that misalignments about the \underline{b} axis are small.

In principle the equations derived in Appendix 3 make it possible to calculate the misalignments; attempts to do this however for KHBP failed to give consistent results, probably due to imperfect data. In the case of sodium formate an approximate method was sufficient to reduce the effect of misalignment within that of the other errors. For the larger couplings measured in KHBP the following approach was finally adopted.

The \underline{a} -axis in the \underline{ab} plane was arbitrarily assumed to be accurate. (One needs a reference point like this because there is no symmetry direction in the \underline{ac} plane to define \underline{a} or \underline{c} ; the final result may be in error by 1 or 2° about \underline{b}) By definition, \underline{ab} was now accurate to within a rotation about \underline{a} . Comparison of the crossover frequencies in the \underline{ac} plane established the position of \underline{a} in the latter to within 0.3°. (The fact that there was no detectible misalignment of \underline{ac} was helpful but not essential: the average of split lines would serve the same purpose).

\underline{c}^* was then defined as the direction in \underline{ac} at 90° to \underline{a} , so that \underline{ac} was correct to within (very small) rotations about \underline{a} and \underline{c} . The corresponding frequencies were read off and compared to the crossover points in \underline{bc}^* . The ' \underline{c}^* ' crossovers must lie in the \underline{ac} plane, although those at \underline{b} may be shifted a considerable distance from the true axis. Comparison of \underline{ac}^* and \underline{bc}^* then established where the latter cut the former, and enabled \underline{bc}^* to be corrected

for misalignments about \underline{b} . All three planes were now (to within 0.3°) in error be rotations about \underline{a} and \underline{c}^* only.

The resulting rms error for the methylene coupling tensor in the benzyl radical in KHBP was reduced from 130 to 80kHz, by this procedure.

Appendix 3 shows that once misalignments about \underline{b} have been eliminated the numerical average of $A_{ij}^{(1)}$ and $A_{ij}^{(2)}$ is independent of \underline{R} to first order and is equal to $|T_{ij}|$. Such averages are used in the discussions of the results.

Chapter 4

EPR and ENDOR Studies of CO_2^- Centres in UV- and X-Irradiated Single Crystals of Sodium Formate

4.1 Introduction

In 1961 using EPR Ovenall and Whiffen (112) identified the CO_2^- radical ion in γ -irradiated single crystals of sodium formate at room temperature. They showed that the radical interacts with a single ^{23}Na nucleus, which gives rise to an almost isotropic, four line hyperfine pattern of splitting approximately 25 MHz. They measured the g-tensor and the hyperfine tensor due to ^{13}C ($I=\frac{1}{2}$) in natural abundance (ca 1%), and used the results to estimate the coefficients of the atomic orbitals comprising the Molecular Orbital containing the unpaired electron.

The electronic structure of the radical was assigned by analogy with the isoelectronic species NO_2 (also C_{2v}) for which the results of Molecular Orbital calculations were available, and is $[(1s)]^6, (1a_1)^2, (1b_2)^2, (2a_1)^2, (2b_2)^2, (3a_1)^2, (1b_1)^2, (3b_2)^2, (1a_2)^2, (4a_1)^1; {}^2A_1$ so that the radical has σ symmetry. Some non-axiality of the ^{13}C -A tensor was interpreted in terms of polarisation of the b_1 levels.

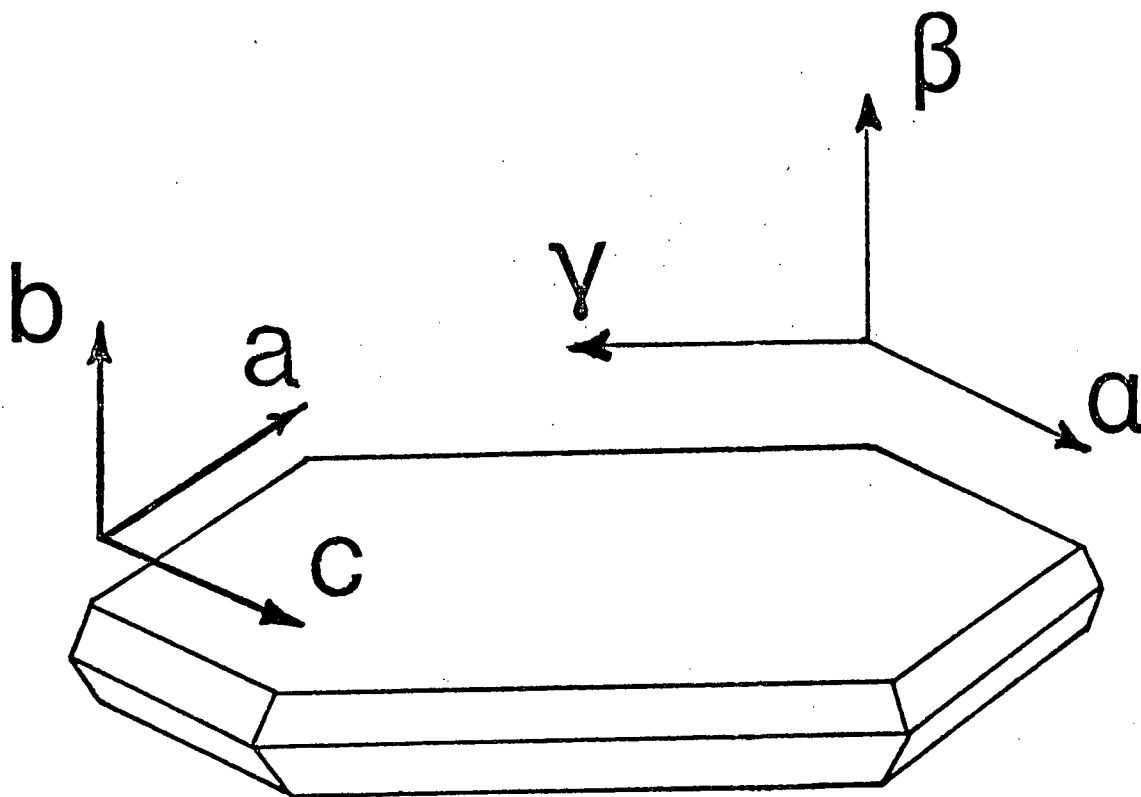


Fig. 7. Typical morphology and axis systems for sodium formate.
 a , b , c are the crystallographic axes determined by Markila;
 α , β , γ are the axes originally determined by Zachariasen in
Reference 122.

The odd-electron Molecular Orbital is concentrated in the carbon s and p orbitals ($c_s=0.39$ $c_p=0.67$) so that more than 50% of the spin is localised on the carbon atom. The ratio a_{iso}/B for the ^{13}C hyperfine interaction applied to the Coulson relationship (82) indicates hybridisation of the form sp^n ($n\sim 1.8$) for the odd-electron orbital on carbon and hence implies an OCO angle of $130\pm 5^\circ$, the uncertainty arising mainly from that in the value of B for the carbon 2p orbital.

Subsequently CO_2^- was studied in a range of environments, and by a variety of techniques, by other workers; the general conclusions of Ovenall and Whiffen were confirmed. Luz et al using ^{17}O -enriched sodium formate measured the ^{17}O hyperfine interactions, and determined the spin densities on the oxygens directly rather than relying on values inferred from the calculated g-shifts (113). Symons et al surveyed the EPR parameters of CO_2^- and NO_2 in a variety of matrices (114, 115), and discussed the effect of the environment on the hybridisation at the central atom. Hartmann and Hisatune studied the infra-red spectra of CO_2^- in alkali halide discs and estimated the OCO bond angle to be $127\pm 8^\circ$ from the effect of isotopic substitution on the vibrational frequencies (116). CO_2^- was also produced by the reaction between carbon dioxide and sodium metal (118).

CO_2^- is produced when alkali or alkaline earth formates or oxalates are irradiated, and also by irradiation of some carbonates notably calcite (126). In many of these cases the EPR spectrum of the CO_2^- ion shows hyperfine structure due to interaction with a metal cation, but also in many cases CO_2^- is neither the only product of irradiation nor the most stable one at room temperature (115). Evidently the small size of the radical ion requires an ionic environment to stabilise the species, but, as suggested by the appearance of metal hyperfine structures such ionic interactions tend to have covalent character as well. Thus if other atoms are present the radical centre tends

to stabilise itself by forming a larger species than CO_2^- : while CO_2^- is quite stable in calcite, other species tend to dominate in hydrated oxalates or formates. Similarly irradiation of acetates or salts of higher aliphatic acids produces mainly such species as H_2CCO_2^- although CO_2^- may also be present in small amounts particularly at low temperatures and in fact Iwasaki et al have studied CO_2^- radical pairs in X-irradiated lithium acetate (116). In this study there appears to be a significant difference in ^{13}C hyperfine parameters between single and paired CO_2^- ions - presumably the result of inter-radical forces which modify the geometry of the pairs.

Sodium formate is one of the simplest matrices in which to study CO_2^- . Unlike many other salts in which CO_2^- can be formed, NaHCO_2 is anhydrous and possesses a relatively simple crystal structure. As a result CO_2^- is the major product of irradiation and is formed in a particularly simple orientation, with its C_2 axis coinciding with the b axis of the crystal, and the radical is stable for several months at room temperature.

After the work of Ovenall and Whiffen, sodium formate itself received further attention; Whiffen and Chantry (119) obtained ultraviolet absorption spectra of single crystals. Bellis and Clough (120) used EPR to study the thermally induced reaction of CO_2^- in the sodium formate lattice to form a new paramagnetic species. Some new results concerning this reaction are presented in Appendix 4.

In 1967 Cooke and Whiffen made ENDOR measurements on γ -irradiated sodium formate at 77K (121); they determined the ^{23}Na hyperfine and quadrupole tensors, and showed that strong proton ENDOR enhancements could also be obtained, but did not make a detailed study of the latter.

Since the proton isotropic hyperfine coupling can be used as a sensitive measure of covalency in paramagnetic species (83) an ENDOR study of the unresolved proton superhyperfine structure seemed to offer a means of probing

the environment of the CO_2^- centre in sodium formate. A second motive for this study was the assignment of the sodium hyperfine structure. Although, as stated above, the EPR spectra show interaction with a single sodium nucleus, the crystal structure shows the formate ion to be roughly equidistant between two Na^+ ions, and no wholly convincing arguments had been presented to identify the nucleus responsible for the observed interaction.

The EPR results discussed so far had been interpreted in terms of the available crystal structure of sodium formate published by Zachariasen in 1941 (122); this structure did not show the positions of the hydrogen atoms, and we therefore requested a redetermination of the structure at this Department. This was carried out by Markila using X-ray diffraction techniques (123), and showed some significant differences from Zachariasen's results, most notably in the choice of axis systems.

The relation between Zachariasen's and Markila's axis systems is shown in Figure 7. Fortuitously, the orthogonal axes a, b, c^* chosen by Whiffen are within 1° of the true axes.

The precision of the X-ray data enabled the charges on all atoms to be refined by treating the core and valence shells of each atom separately, with the population of the latter taken as a parameter to be refined. The results, C: 0.16(3)e; O: -0.23(1)e; H: -0.49(10)e; Na: 0.79(14)e, indicate a considerable amount of covalency in the formally pure-ionic Na-O bonds, and a highly unusual $\text{Na}^+ \dots \text{H}^- \text{ -- } \text{C}^+$ hydrogen bond of opposite polarity to the usual forms such as $\text{F}^- \text{ -- } \text{H}^+ \dots \text{F}^-$.

As determined by Markila, crystals of sodium formate are monoclinic with $a=6.2590(6)$, $b=6.7573(16)$, $c=6.1716(5)$ Å; $\beta=116.140(6)^\circ$; $Z=4$; space group C2/c . The sodium formate molecule is planar with C_{2v} symmetry, and the formate ions lie in layers parallel to the b axis. Each sodium has six oxygen neighbours

at an average distance of 2.45\AA . Together with the $\text{Na}\dots\text{O}$ covalency mentioned above, the weak $\text{C-H}\dots\text{Na}$ hydrogen bonds form continuous rows of NaHCO_2 molecules along the b axis. The C-O bond length is $1.246(1)\text{\AA}$, the OCO bond angle $126.3(2)^\circ$.

Apart from the increased bond angle, the CO_2^- centre takes up essentially the same position as its formate ion precursor; this is shown quite clearly by the absence of site splittings for any of the g , hyperfine, or quadrupole tensors. Thus any change in the relative positions of the central carbon atom and the two nearest neighbour sodium ions must occur along the b -axis. This point is relevant to a discussion of the origin of the sodium hyperfine interaction.

4.2 EPR of uv-Irradiated Crystals.

After a few minutes' uv irradiation, crystals of NaHCO_2 showed the characteristic four-line EPR spectrum of the $\text{CO}_2^- \dots \text{Na}^+$ species. The spectra were identical to those obtained by X-irradiation, and those described by Whiffen et al for γ -irradiated crystals.

Prolonged irradiation with a Hanovia 679A mercury lamp gave sufficiently strong signals to show the ^{13}C hyperfine lines, from ^{13}C (with $I=\frac{1}{2}$) in natural abundance. EPR measurements in three perpendicular planes provided data from which the g - and ^{13}C A-tensors were calculated; their principal values are shown in Table I, where the results for γ -irradiated samples are included for comparison.

The signal-to-noise ratio for the ^{13}C satellites was low, and for orientations where the couplings were smallest, the satellites overlapped the wings of the main spectrum, making the line positions hard to determine precisely.

In view of this and the variation in the published parameters for irradiated sodium formate (112, 121) the agreement for both g and A is within the experimental uncertainty and serves to confirm that the products of uv and

γ -irradiation are the same.

Table I: EPR parameters for the CO_2^- centre produced
by γ and UV irradiation

	γ Irradiation ^a	UV Irradiation
^{13}C A-tensor MHz	546	544
	436	429
	422	410
g-tensor	2.0014	2.0022
	2.0032	2.0032
	1.9975	1.9980

^a Reference 112.

Interposing filters of Pyrex, Corex, or Vycor glass between the uv source and the crystal established that light of wavelength 260 ± 20 nm is necessary for the photolysis to occur. This value is based on the published transmission characteristics of the glasses, and a semi-quantitative estimate of the relative EPR intensities after equal irradiation times on a given crystal. The corresponding energy is 110 ± 10 kcal/mole, which is about 25 kcal/mole greater than the C-H bond strength in sodium formate.

It may be significant that there is a weak absorption band at 255 nm specific to the single crystal spectrum of sodium formate (119). The mechanism of photolysis does not seem to be simple. Several attempts to produce CO_2^- by uv irradiation at 77K failed to reveal any paramagnetic species, although CO_2^- was produced (in lower yield) at temperatures between 300 K and 238 K (1-2 dichloro ethane/liquid nitrogen slush). These results are consistent with a mechanism of radical formation in which absorption of energy by a sodium formate molecule produces an electronic excited state of the molecule which

will decay back to the ground state unless higher vibrational levels are populated, permitting dissociation to occur.

X-irradiation of sodium formate at 77K does produce CO_2^- ; this is consistent with the above observations since the primary products of X irradiation are high energy electrons which deposit energy relatively continuously in the lattice, and thus are capable of causing local heating effects as well as specific electronic transitions (124).

4.3 Proton ENDOR Studies

X-irradiated crystals were used for all ENDOR measurements since they had much stronger EPR signals than crystals irradiated by ultraviolet light. The duration of the X-irradiation was found to be important: 2-4 hours gave the strongest ENDOR signals. This point is discussed in more detail later.

Figure 10 shows a typical proton ENDOR spectrum, for which the magnetic field is oriented at 60° to the β axis in the $\gamma\beta$ plane. The spectrum shows the usual near-symmetry about the free proton frequency, ν_p , and also includes a single sodium ENDOR line which falls within the range of the scan.

The angular variation of the proton spectra in the planes of observation is shown in Figures 8, 9 where the site splittings in the $\alpha\beta$ and $\gamma\beta$ planes are clearly apparent. Approximately 90 measurements were used to fit each tensor, and the rms. error was typically 30kHz, slightly less than the ENDOR linewidth. The main sources of error are small residual misalignments of the crystal, and the uncertainty in the line positions due to the overlap of ENDOR lines.

The diagonalised forms of the proton hyperfine tensors obtained are given in Table II. Their assignments to specific protons were made by comparing the direction of the largest anisotropic principal value to the directions expected from the crystal structure. Since most of the spin density of the

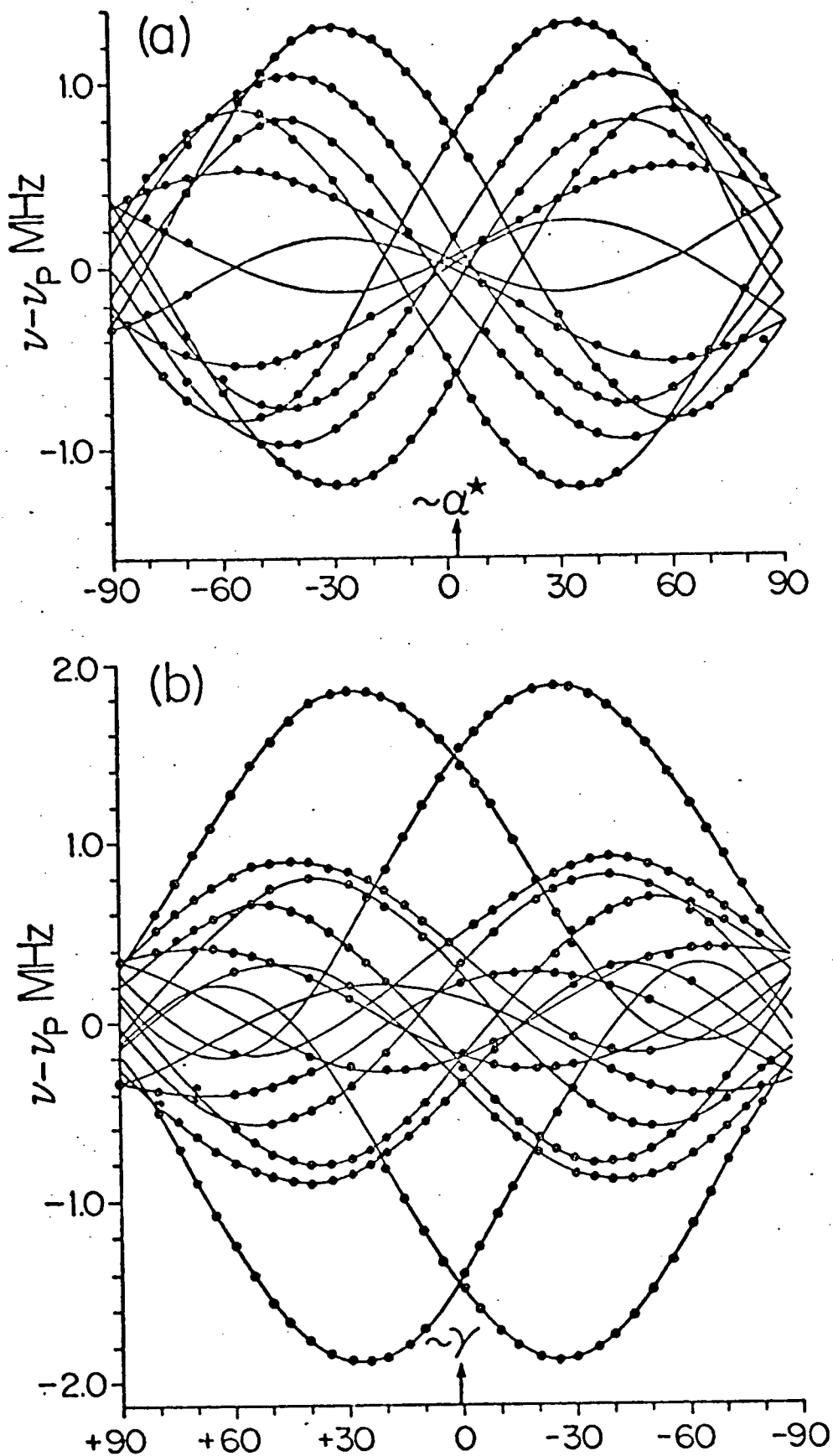


Fig. 8. Angular variation of proton ENDOR frequencies in (a) approximate $\alpha\beta$ and (b) the approximate $\gamma\beta$ plane. The ordinate is the difference between the ENDOR frequency and the free proton nmr frequency.

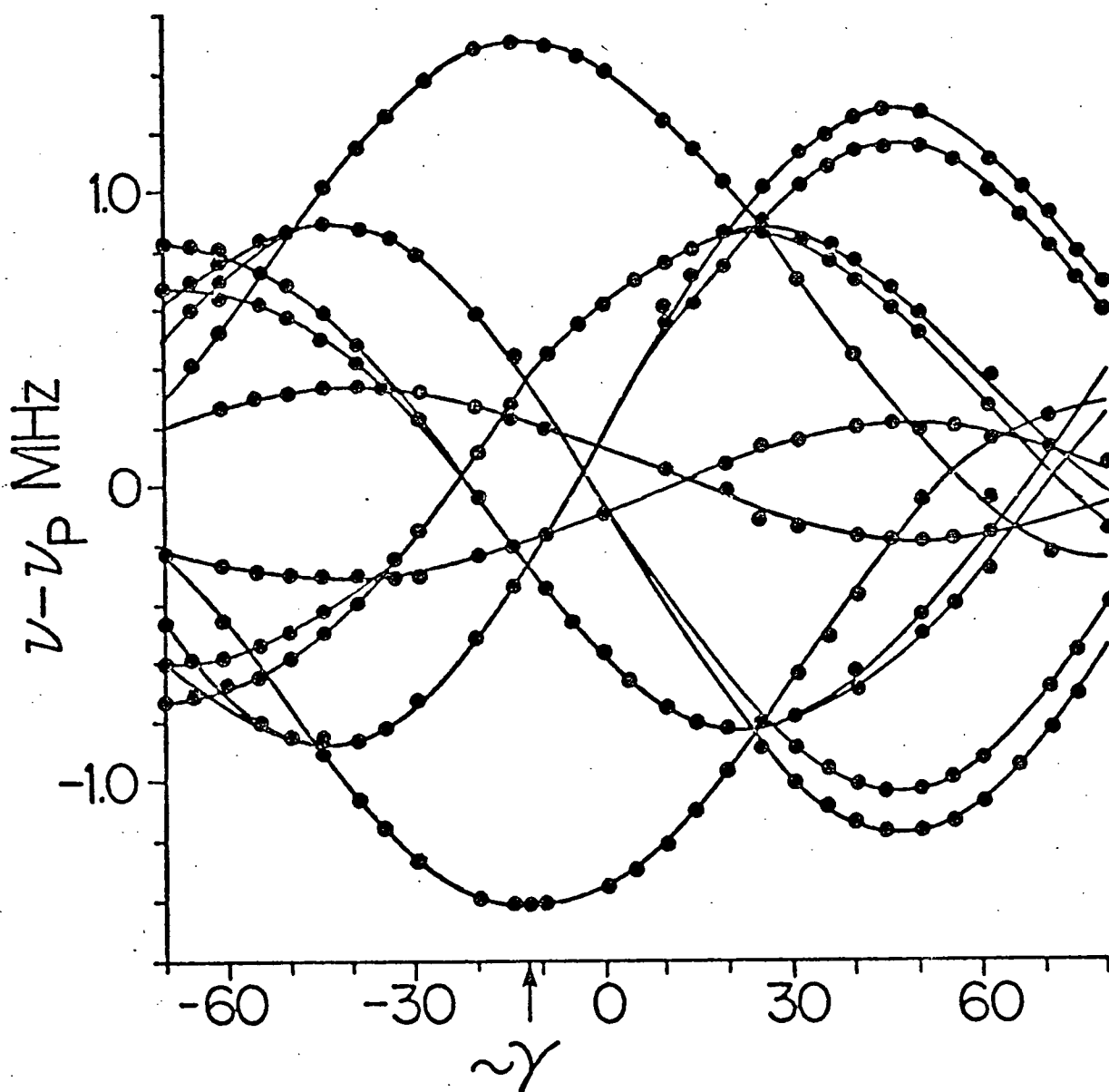


Fig. 9. Angular variation of proton ENDOR frequencies in the approximate $\alpha\gamma$ plane of sodium formate. The ordinate is the difference between the observed frequency and the free proton nmr frequency.

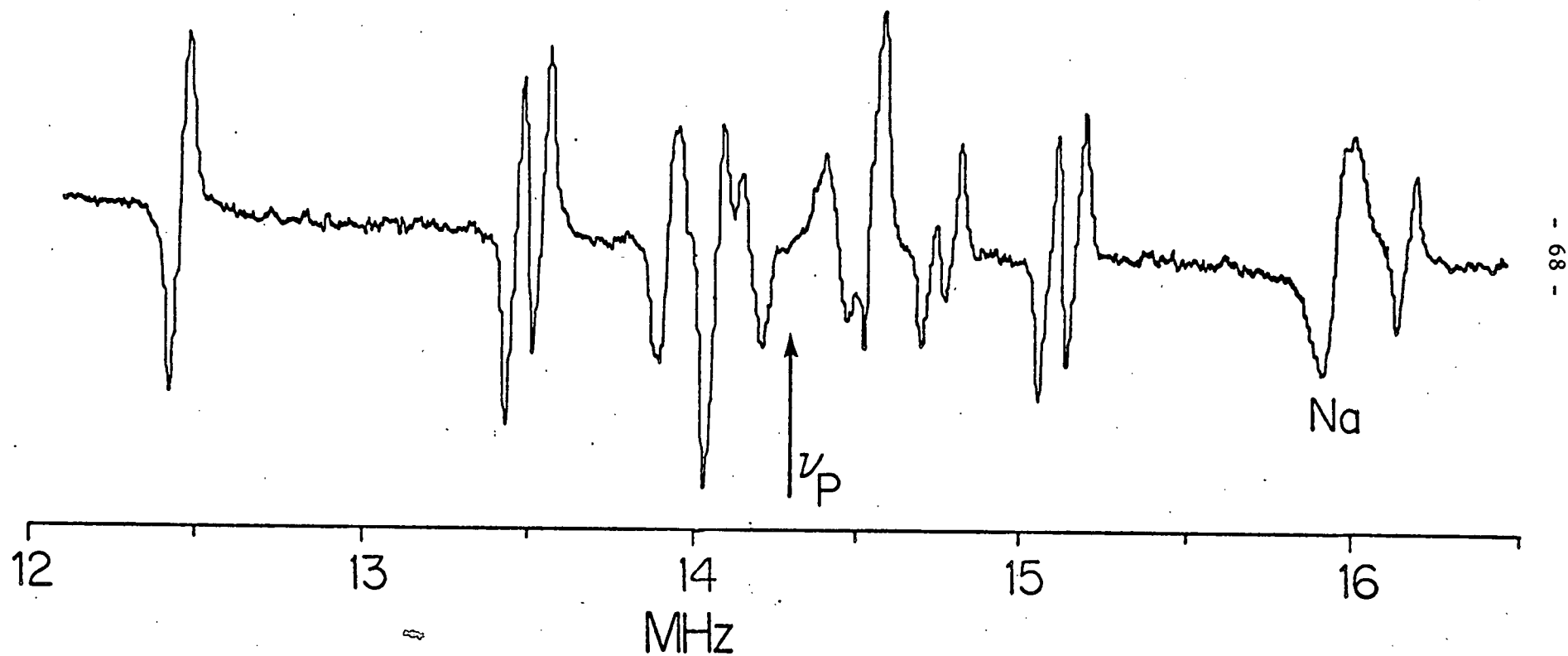


Fig. 10. A typical spectrum of X-irradiated sodium formate at 77K the magnetic field is oriented at 30° to the β axis, in the $\gamma\beta$ plane. A Sodium ENDOR line is shown near 16 MHz.

- 65 -

CO_2^- fragment is on the carbon atom, the intermolecular C...H directions serve to identify this tensor direction. As a refinement of this procedure we estimated the dipolar parts of the tensors themselves, using the McConnell-Strathdee equations (99), modified by Barfield (101) as described in Chapter 2. The results of these calculations were also used to determine the sign of the total tensor. All three atoms of CO_2^- were included, with the 2s and $2p_z$ orbitals (the latter being along the crystal b axis) contributing positive spin density; the radical geometry and spin densities were based on EPR data (113). The results of these calculations are also given in Table II. The quoted uncertainties in the experimental principal values are derived from either the deviation between equivalent crystal sites or the experimental rms error, whichever is the greater, and the assignments to specific protons are shown in Figure 11.

In general, the calculated dipolar tensors reproduce the observed values quite well. Some of the deviations are due to neglect of polarisation spin densities in the theoretical model. The most significant deviations occur for tensors 2 and 4, which are markedly less axial than the calculated tensors. In view of the agreement achieved for tensors 1 and 3 and the fact that even a point-dipole approximation should be quite good for the 5.4 Å C...H distance corresponding to proton 4, the discrepancies can hardly be due to using Slater orbitals in the calculations. Since no reasonable variation of parameters in the calculations reproduced the observed nonaxiality, and the two tensors are those with significant isotropic parts, we conclude that covalency contributes appreciably to these two hyperfine interactions. On this basis the form of tensor 2 can be explained as follows. The $2p_x$ orbital (perpendicular to the radical plane) of one of the oxygens of the CO_2^- is directed almost exactly at the carbon bonded to hydrogen 2, ($\angle \text{OCQ} = 97.5^\circ$) and similarly the $2p_x$ orbital of the CO_2^- carbons is directed at

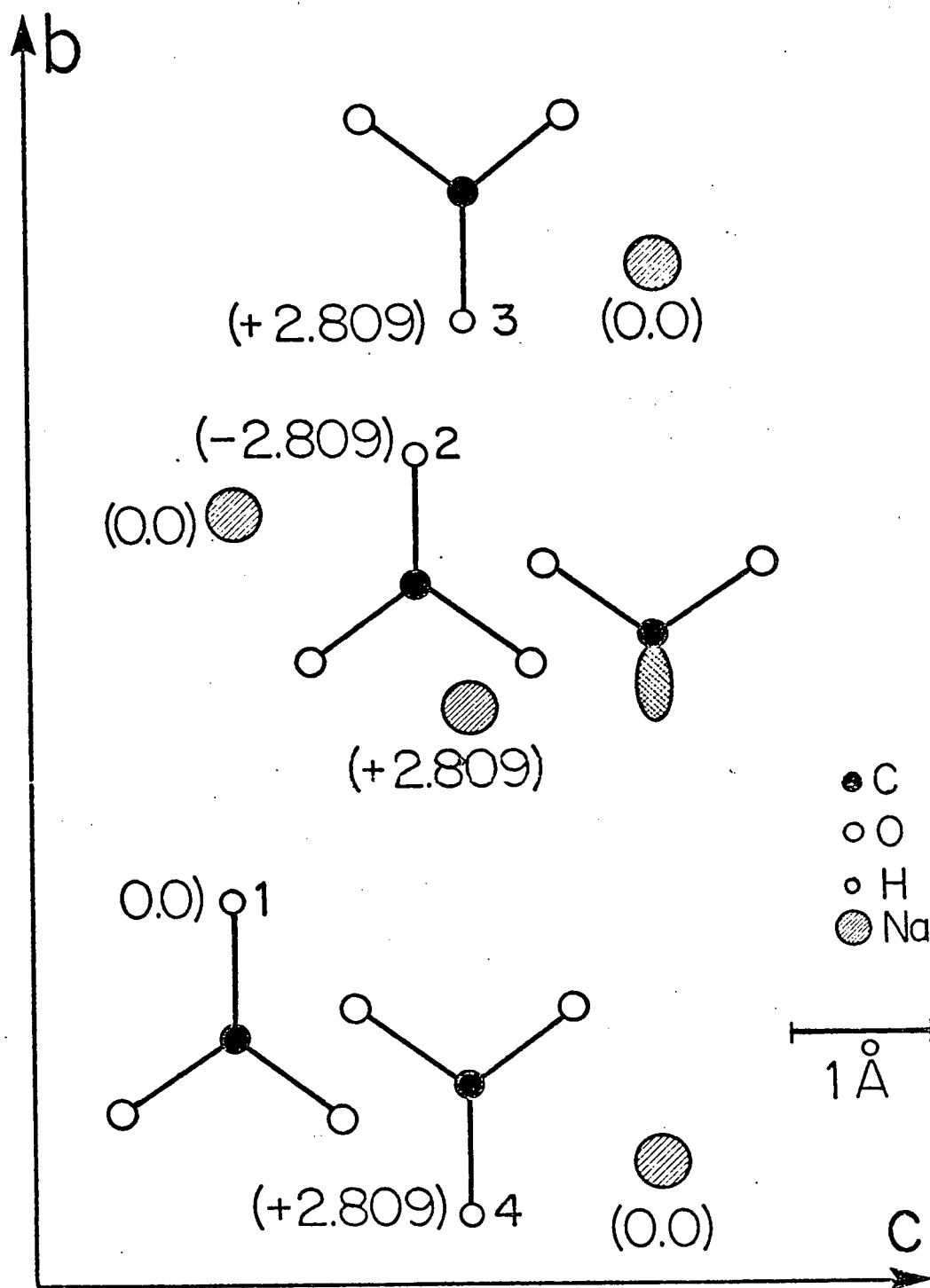


Fig. 11. Projection of part of the sodium formate lattice into the crystallographic bc plane, showing the hydrogen atoms corresponding to the hyperfine tensors listed in Table II. The figures in parenthesis are the distance in Å perpendicular to the bc plane from the plane containing the CO_2^- radical.

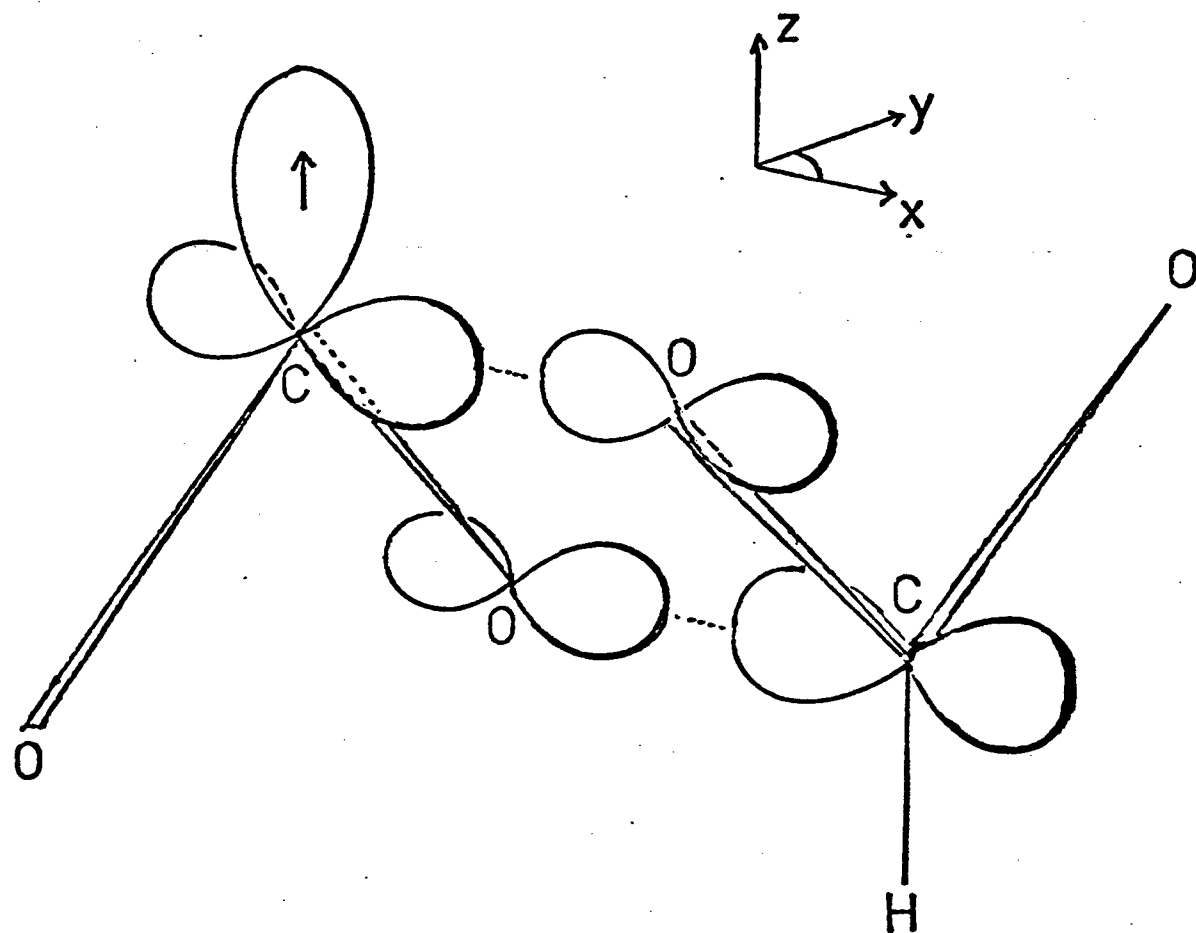


Fig. 12. Schematic representation of a p-orbital overlaps inducing spin density in an HCO_2^- neighbour of the CO_2^- radical ion.

an oxygen of the formate ion, so that intermolecular overlap of the p_x orbitals on both C and O is possible. Luz et al (113) find approximate spin densities of respectively +8% and -1% in the $2p_x$ orbitals of C and O in the CO_2^- fragment; hence such overlap can induce spin in the neighbouring molecule. However the carbon $2p_x$ orbital itself cannot be the main source of spin density on that molecule: to account for the positive contact term, such spin would have to be negative (by analogy with the 'classical' C-H fragment (111)), and this would make the tensor component closest to b more negative, in conflict with observation.

Instead we must postulate that electron correlation effects between CO_2^- and HCO_2^- ions induce positive spin density in the σ orbitals of this HCO_2^- ion. See Figure 12. This follows if we regard each pair of overlapping $2p_x$ orbitals as a single orbital in which the spin density due to polarisation changes sign between CO_2^- and HCO_2^- , as in the C-H bond of π -electron aromatic radicals. If the relative signs of the σ and π polarisations are the same in the formate ion as in CO_2^- this will then induce positive spin density in the σ orbitals of the formate.

The observed contact term is a little larger than one would expect if this were the only mechanism in effect; direct overlap of the σ orbitals of the two ions may make an additional contribution.

Essentially similar arguments should hold for tensor 4. The measured isotropic part in this case is however rather small, which makes it more difficult to assess the importance of the various mechanisms contributing to the spin density at H4.

A slight displacement of the CO_2^- fragment, as suggested by the Na hyperfine couplings, would add further complications but will not essentially change the interpretation.

Table II: Proton Hyperfine Tensors in X irradiated Sodium Formate

Experimental						Calculated			
TENSOR	a _{iso} MHz	Dipolar Part				Dipolar Part			
		Principal value MHz	Direction Cosines*			Principal value MHz	Direction Cosines*		
			l	m	n		l	m	n
1	-0.02 ±0.02	3.15 ± 0.04	-0.053	∓0.607	-0.793	3.18	-0.019	∓0.484	-0.875
		-1.65 ± 0.03	0.994	±0.042	∓0.016	-1.63	0.834	∓0.491	0.254
		-1.50 ± 0.01	∓0.105	0.793	∓0.600	-1.55	±0.557	0.724	∓0.413
2	0.85 ±0.02	2.95 ± 0.04	0.747	±0.437	0.502	2.66	0.767	±0.417	0.488
		-0.945 ± 0.04	-0.609	±0.752	0.253	-1.34	-0.600	±0.736	0.314
		-1.98 ± 0.004	±0.267	0.495	∓0.827	-1.32	±0.229	0.532	∓0.816
3	0.02 ±0.01	3.51 ± 0.06	0.785	∓0.481	-0.390	2.48	0.720	∓0.621	-0.308
		-1.82 ± 0.03	0.597	±0.414	0.687	-1.26	0.476	±0.120	0.871
		-1.69 ± 0.03	±0.168	0.773	∓0.612	-1.22	±0.505	0.774	∓0.383
4	0.127 ±0.006	1.145 ± 0.006	0.575	±0.779	-0.251	1.02	0.540	±0.800	-0.260
		-0.360 ± 0.010	-0.656	±0.622	0.428	-0.506	-0.558	±0.572	0.601
		-0.787 ± 0.005	±0.489	-0.082	±0.868	-0.517	±0.630	0.179	±0.755

* The direction cosines are referred to the crystal axis system as determined in reference 5; m and n corresponds to b and c of that system and l corresponds to the vector b x c.

The signs chosen consistently relate one distinguishable crystallographic site to the other.

4.4 Sodium Hyperfine Interaction

In an attempt to shed further light on the sodium hyperfine coupling which dominates the EPR spectrum of irradiated sodium formate, we investigated the ENDOR of the sodium nuclei at 77K. As mentioned earlier, Cooke and Whiffen (121) made a thorough ENDOR study of this coupling which appears as an almost isotropic quartet of splitting $\sim 8\text{G}$ in the EPR. Our experiments corroborated their results, but our main interest was to look for other sodium couplings, particularly those of the next-nearest-neighbour ions. We carried out a survey of the ENDOR spectra down to 2.5 MHz, the free sodium NMR frequency being approximately 3.8 MHz in our experiments. A typical spectrum for this frequency range is shown in Figure 13. In the early experiments the presence of 3rd and 5th harmonics of the main frequency generated in the rf amplifier at high gain, caused spurious signals to appear at 4.8 and 2.9 MHz from the free-proton region of the ENDOR spectrum; these signals were removed by the use of appropriate low band-pass filters, and the resulting spectra resembled that of Figure 13. The spectra obtained without filters showed no new lines above 5 MHz. Angular variation of the spectra was studied in three perpendicular planes. The high density of lines, coupled with the fact that each sodium nucleus is expected to give six ENDOR lines because of the quadrupole interaction, prevented us from analysing the spectra in detail, but the results show that an upper limit on the hyperfine coupling of the next-nearest neighbour sodium ion is approximately 2.5 MHz. Since the signal-to-noise ratio for the nearest neighbour couplings was ~ 30 , we can be confident that any couplings much larger than 2.5 MHz would have been observed.

This leads to the surprising result that the two nearest neighbour couplings differ by a factor of 10 or more, but does not tell us which sodium is responsible for the observed hyperfine structure. Nor is the dipolar part of

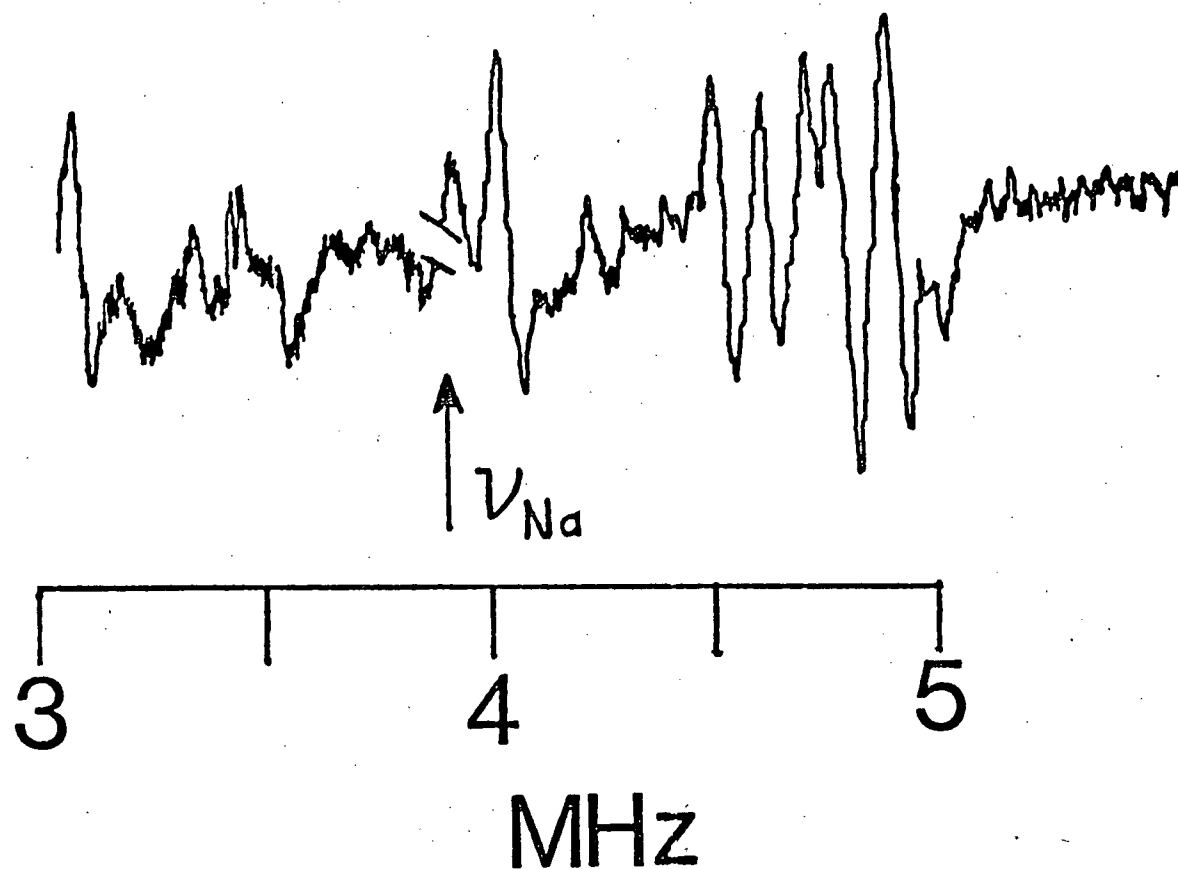


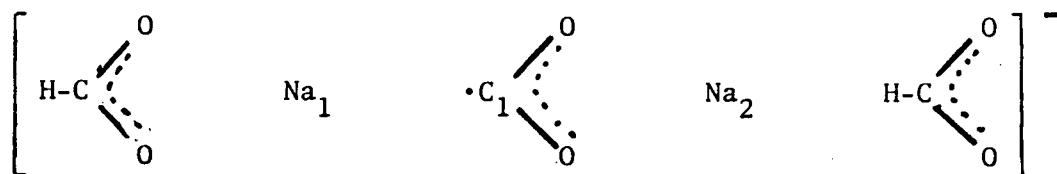
Fig. 13. Sodium ENDOR spectrum in the frequency range near the free sodium nmr frequency ν_{Na} . The break in the spectrum corresponds to a change in the filters used.

the observed coupling helpful here, for as discussed in Appendix 2 the observed 3.7 MHz coupling (121) is too great by a factor of almost three to be a through-space interaction across $\sim 3\text{\AA}$, and must be attributed to the presence of spin density in the sodium p or d orbitals.

From the crystal structure it seems that the sodium closest to the two oxygens is the nearest neighbour, since the corresponding C-Na distance is only 2.8\AA , and the observed Na...O interactions would provide another source of spin density at the sodium; on the other hand, some 60% of the spin density in CO_2^- is in the carbon $2p_z$ orbital directed towards the other Na, and although this C-Na distance is 3.9\AA , the centre of gravity of the sp^n hybrid orbital will be only $\sim 3.0\text{\AA}$ from that sodium. Because of this ambiguity, we intuitively expected some relative shift of the CO_2^- and sodium ions to have produced the large difference in sodium couplings, and we tried to find evidence for such a rearrangement. The ENDOR studies show that the largest principal value of the main sodium hyperfine tensor lies along the crystal b-axis, which is also the C_2 axis of the formate ion so as mentioned earlier, any translation must leave the Na-C-Na direction parallel to the b-axis.

The observed proton tensors provided no clear-cut evidence that the CO_2^- itself had moved; and indeed the interpretation given above for the form of two of the tensors suggests that a significant displacement of the fragment has not occurred. The calculated dipolar tensors are too sensitive to small uncertainties in geometry and spin density to provide convincing evidence, and we therefore attempted to calculate the relative spin densities on the two sodium ions directly.

We based our calculations on the fragment



and used the computer program written by Pople and Beveridge (110), in the CNDO approximation.

As a check on the quality of the method we also performed a calculation on the 'undamaged' fragment, with all three formate ions complete; the calculated charges on the atoms were C: 0.43e; O: -0.48e; H: -0.11e; Na: 0.45e, reproducing the trend of Markila's results.

In the subsequent calculations on the paramagnetic fragment we assumed various values for the two C_1 -Na distances, corresponding to displacements of the CO_2^- or sodium ions along the b-axis, and compared the calculated s-orbital spin densities on these three atoms with their experimental values. Because of the approximations inherent in the abstraction of a small part of the lattice and in the calculations themselves we made no attempt to optimise the geometry for minimum energy.

With the atoms at their crystallographic positions the sodium spin densities were Na_1 2.1% and Na_2 2.6%, and carbon s-orbital spin density was 7.3%, in comparison to the experimental values, Na: 2.6%, C: 15%.

The variation of these quantities with the positions of the three ions does not lend itself to a graphical or algebraic presentation; however some typical results are given in Table III, and the main trends are as follows.

Displacement of the CO_2^- fragment towards Na_1 did not alter the ratio of sodium spin densities appreciably and lowered the carbon spin density still further. Displacing Na_1 towards C_1 increased both sodium spin densities to about 0.04 but left their ratio close to unity; thus it seems unlikely that the sodium ion further from the CO_2^- oxygens is responsible for the large hyperfine interaction.

Displacement of the CO_2^- towards Na_2 by distances of order of 1 Å altered the sodium spin densities to 0.02 and 0.004 in favour of Na_2 and brought

Table III: CNDO Spin densities as functions of geometry

Y_{Na_1}	-3.932	-3.732	-3.232	-3.932	-3.932	-4.132
Y_{Na_2}	2.825	2.825	2.825	2.625	2.825	2.625
Y_C	0.0	0.0	0.0	0.0	1.0	0.1
Δr_1	0.0	-0.2	-0.5	0.0	1.0	0.3
Δr_2	0.0	0.0	0.0	-0.2	-1.0	-0.3
ρ_{Na_1}	0.021	0.034	0.038	0.025	0.004	0.019
ρ_{Na_2}	0.026	0.039	0.036	0.037	0.021	0.036
ρ_C	0.073	0.067	0.056	0.078	0.111	0.090

The Y values are the coordinates in Å of the respective atoms.

Δr_1 is the change in $Na_1 \dots C$ distance from the crystallographic value.

Δr_2 is the corresponding value for $Na_2 \dots C$.

ρ is the CNDO s-orbital spin density.

the carbon spin density closer to the observed value; similarly displacement of Na_2 towards the CO_2^- increased the sodium spin density ratio and the C_1 spin density.

A further possibility, displacement of Na_1 away from C_1 (the result of removing the C-H...Na hydrogen bond) gave a similar result. From these results it seems likely that the sodium ion nearest the oxygens of the CO_2^- fragment is the one responsible for the observed hyperfine couplings, and that the inequivalence of the sodium couplings results from shifts of both Na_1 and Na_2 (and possibly a small shift of the CO_2^- radical itself) along the b-axis in such a way as to increase C- Na_1 and decrease C- Na_2 .

This conclusion is supported by the EPR experiments of Bennet, Mile and Thomas (118), who prepared CO_2^- by depositing sodium on the surface of solid carbon dioxide. This method of preparation practically ensures that $\text{CO}_2^- \text{-Na}^+$ ion pairs are easily formed, and that the Na partner is the one responsible for the dominant hyperfine structure in the EPR spectra of CO_2^- . Similar results were obtained in vibrational studies by Jacox and Jilligan (125).

It is interesting to note also that the Na hyperfine tensor is not quite axial about the formate C_2 axis. A similar though more pronounced nonaxiality is shown by the quadrupole coupling as determined by Cook and Whiffen. These observations suggest that in sodium formate the CO_2^- centre is held rigid in the lattice, a conclusion which is reinforced by comparing the EPR parameters measured at room temperature and 77K (121, 112). For sodium formate there is no significant change in the parameters between these two temperatures, in contrast to observations of CO_2^- in calcite (126) where marked temperature dependences of the EPR linewidth and g-value are attributed to torsional oscillations of the radical; also in lithium acetate (116) the form of the ^{13}C hyperfine tensor is interpreted in terms of motional averaging by nearly free

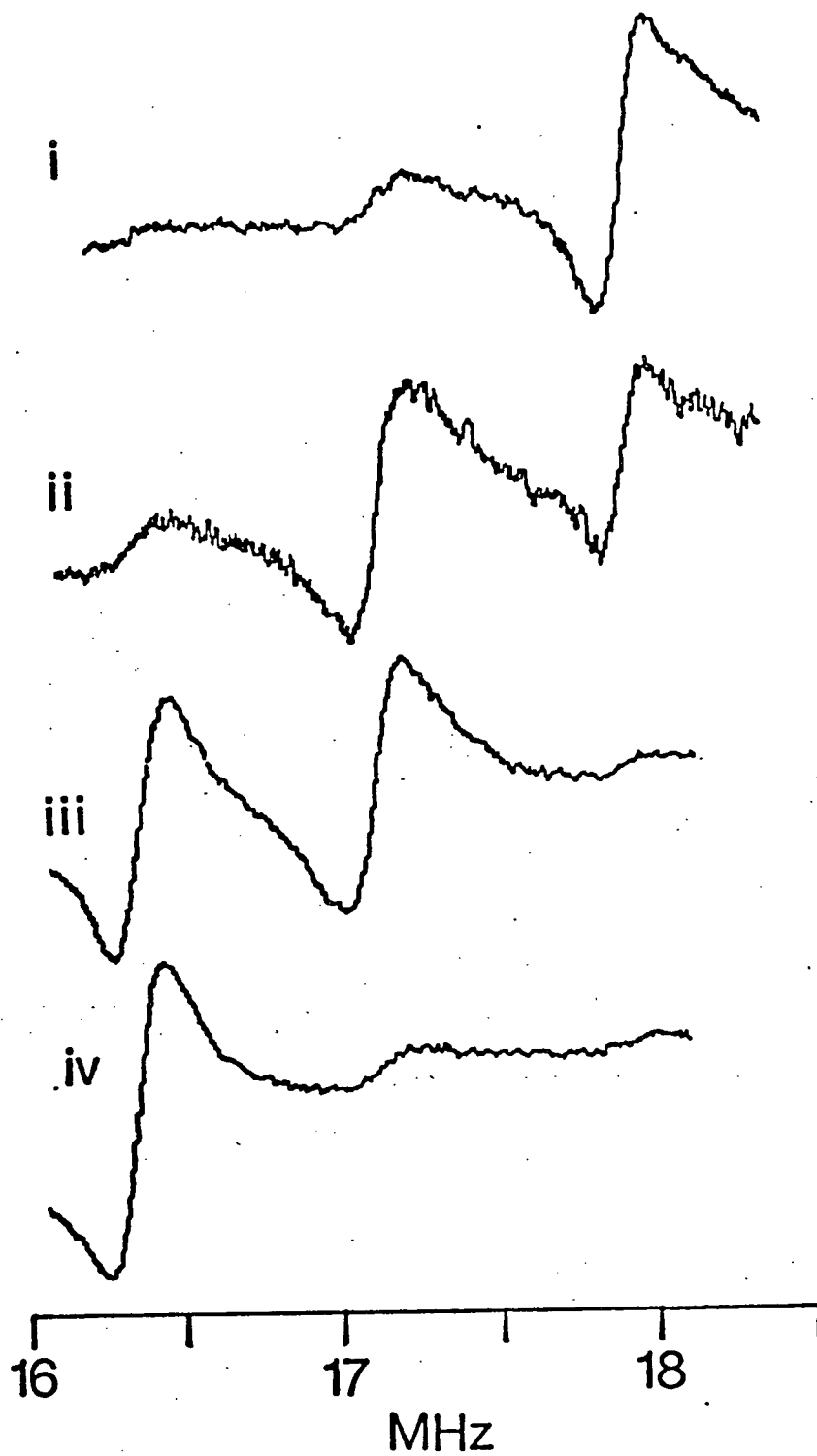


Fig. 14. Sodium ENDOR spectra obtained by irradiating EPR lines i - iv in turn, in order of decreasing field.

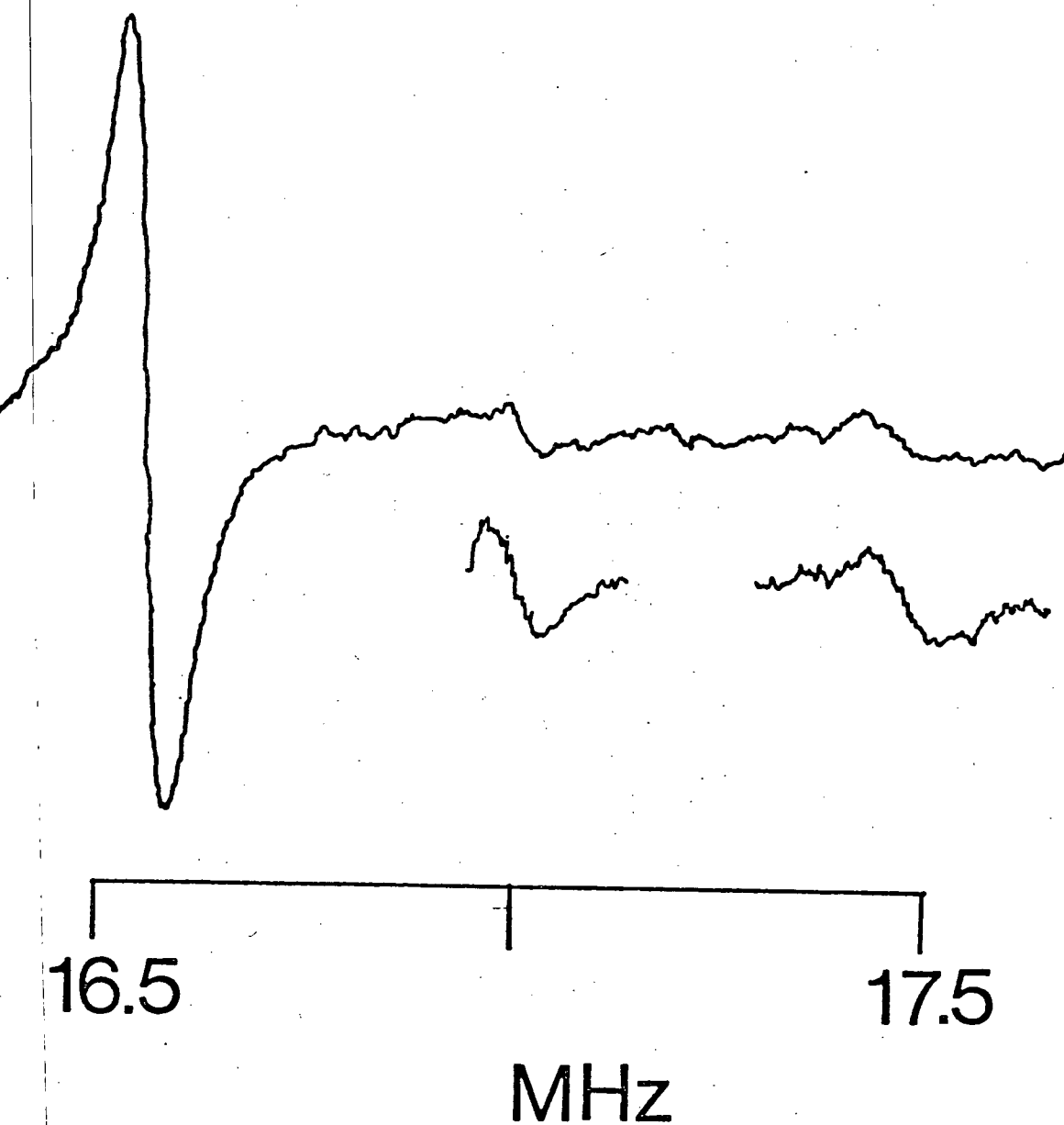


Fig. 15. Appearance of all three sodium ENDOR lines obtained by irradiating the lowest field EPR line. The two weak lines are also shown at higher gain.

oscillations about the 0...0 directions.

4.5 ENDOR Intensities and Relaxation Mechanisms

During the ENDOR studies of the nearest neighbour Na nuclei some effects were observed which cannot be explained in terms of the simplest model of ENDOR (references (59, 7)). and thus have a bearing on the ENDOR mechanism itself.

The first of these effects concerns the ENDOR spectra observed when each of the four EPR lines was saturated in turn. Typical results are shown in Figure 14, where it can be seen that not only does the intensity of the strongest line vary, but also that other, normally 'forbidden' lines appear. ('Forbidden' in the sense that the simple model of ENDOR enhancements predicts no such lines but rather when as here $a/2 < \nu_{Na}$, saturation of the $m_I = \pm 3/2$ lines within a given m_S manifold is expected to give one ENDOR transition each, and saturation of the $m_I = \pm 1/2$ lines to give two equally intense lines separated from the first pair by the quadrupole interaction.) This effect also appears without comment in the spectra published by Cook and Whiffen (121). Figure 15 shows the appearance of all three high frequency ENDOR lines obtained by saturating the lowest field EPR transition. The 'expected' ENDOR line is at 16.5 MHz. It should be emphasised that the results presented in Figures 14 and 15 were quite reproducible, and essentially independent of the position of the saturation point within a given EPR line. Electronic T_2 mechanisms are thus not the cause of this effect.

We attempted to model the relaxation behaviour by a set of coupled equations in which the rates of change of population of the eight multiplet levels were given in terms of the population differences and first order rate constants representing microwave transitions and T_1 , T_{1N} and T_x processes,

these rate constants being treated as adjustable parameters. Requirement that the system be in a steady state produced eight linear simultaneous equations which were then solved numerically for the populations of the eight levels. We did not succeed in developing a quantitative description of the observed ENDOR intensities, but were able to draw some qualitative conclusions.

The observed intensity ratios of the strong ENDOR transitions varied too unsymmetrically with m_I to be the result of simple T_1 processes ($\Delta m_S = \pm 1$, or $\Delta m_I = \pm 1$).

The most likely relaxation mechanisms are through vibrational modulation of the sodium quadrupole and hyperfine tensors, and cross relaxation. The quadrupolar and anisotropic hyperfine interactions are too small for their contributions to be dominant, but the total hyperfine interaction can be written fairly accurately as

$$a \cdot [S_z I_z + \frac{1}{2}(S_+ I_- + S_- I_+)]$$

so that its time variation can induce transitions with $\Delta m_S = \pm 1$, $\Delta m_I = \mp 1$; in contrast, the cross-relaxation mechanism can induce the forbidden transitions $\Delta m_S = \pm 1$, $\Delta m_I = \pm 1$, and can result from interaction with neighbouring paramagnetic centres (127, 128). As has been discussed by Kwiram et al (127), this latter mechanism can be the dominant one in molecular crystals when irradiation results in the formation of several paramagnetic species, and the effective relaxation rate is likely to be primarily due to modulation of the g-tensor of the most anisotropic species.

Some evidence for the importance of cross relaxation is provided by our second main observation -- the variation of ENDOR intensity with irradiation dose. The optimum ENDOR signal-to-noise ratio was obtained with irradiation times of 2-4 h. Longer irradiations resulted in a rapid decrease in the intensity of the main ENDOR spectrum while shifting intensity to the 'distant

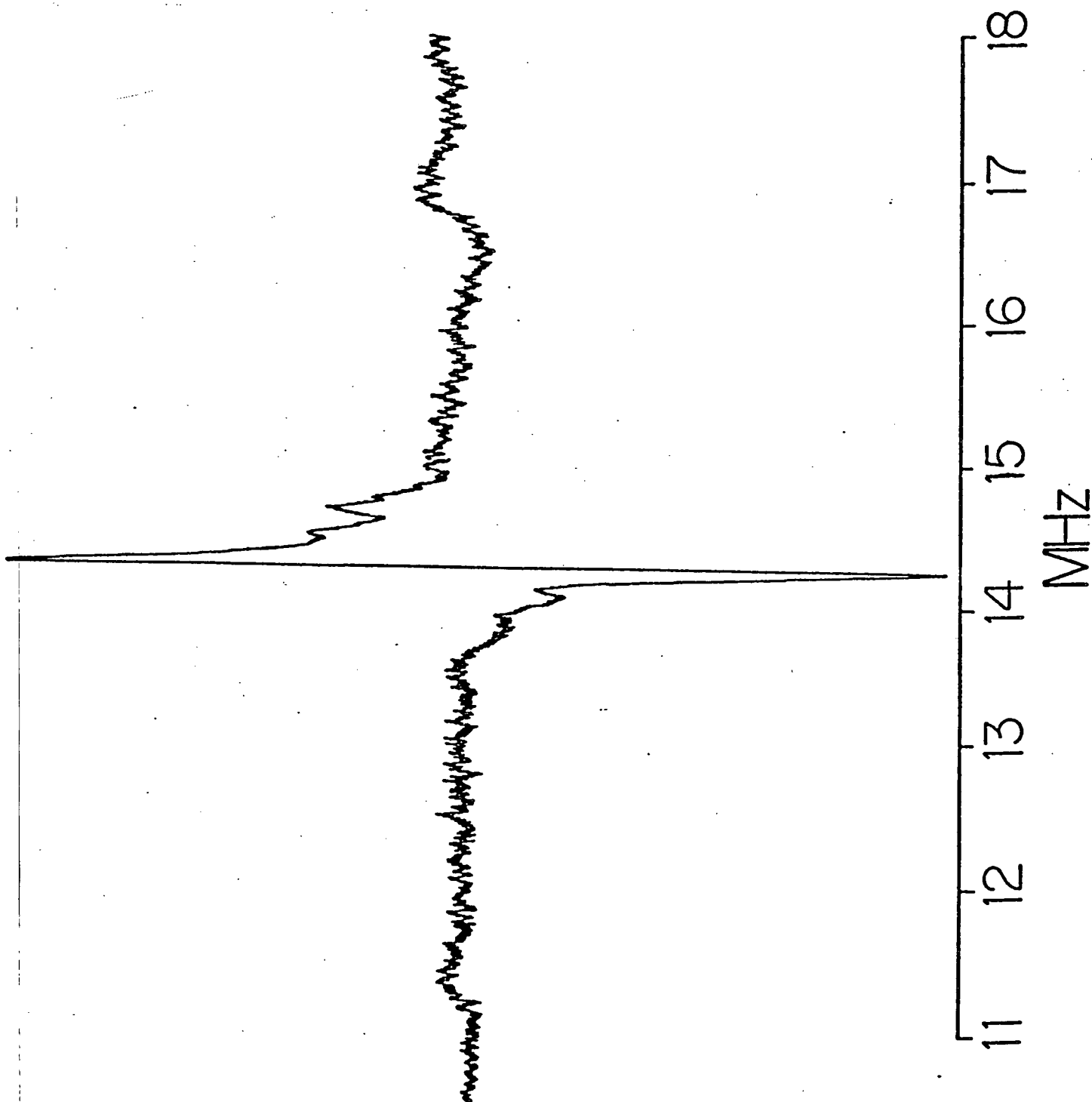


Fig. 16. ENDOR spectrum obtained from sodium formate crystal after 11.5 hr X-irradiation, showing the strong 'distant ENDOR' proton resonance line.

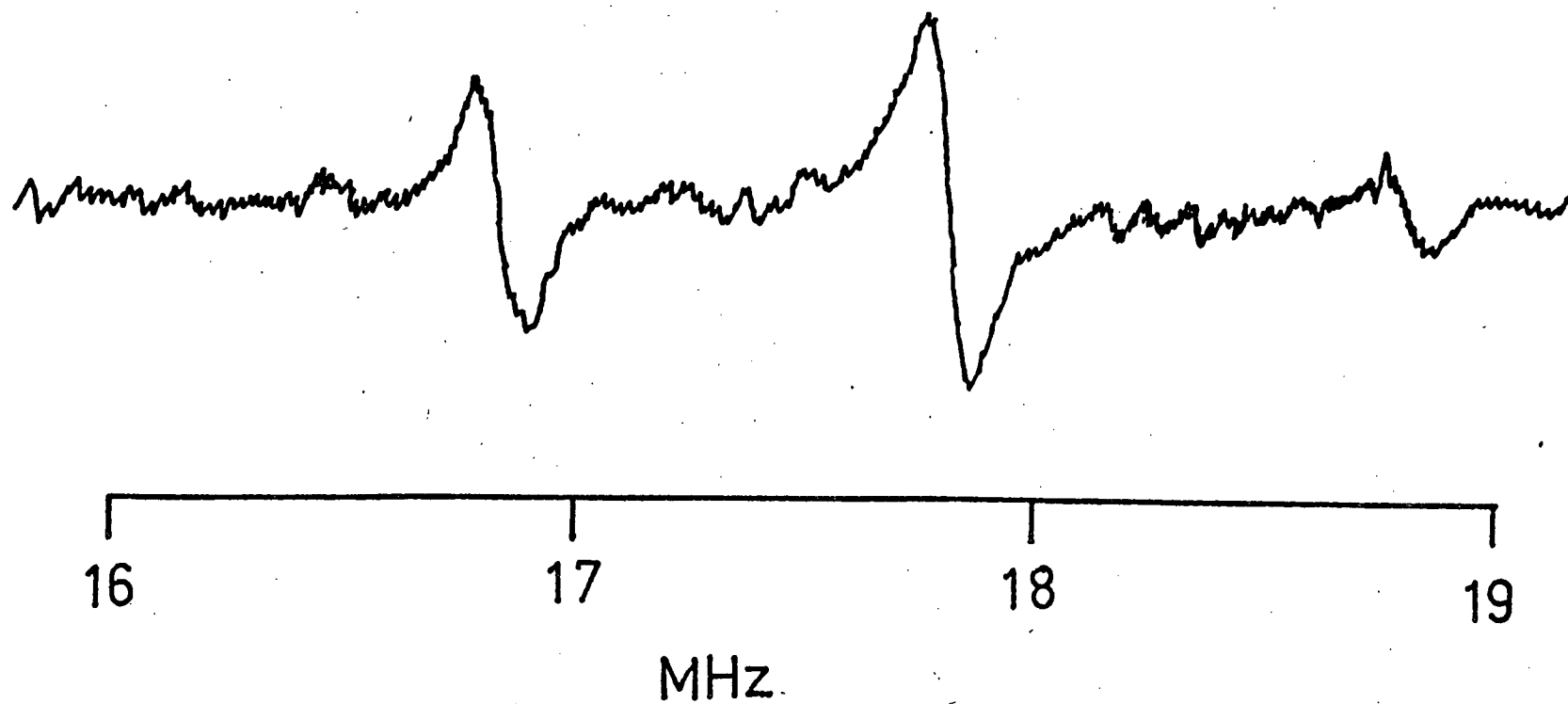


Fig. 17. Sodium ENDOR lines obtained by irradiating the second lowest field EPR line at 4.2K.

ENDOR' line (79). Finally after 11-12 hours of irradiation, the spectrum shown in Figure 16 was obtained. Comparison with Figure 10 shows that the former spectrum is completely dominated by the distant ENDOR line. The EPR spectra of heavily irradiated crystals revealed a significant increase in the concentration of another paramagnetic species, evidently that described by Bellis and Clough (120), for which the g-tensor has the principal values 2.002, 2.006, 2.006. Further support for this interpretation comes from the results of ENDOR experiments at 4.2K, in which the sodium ENDOR enhancements were qualitatively similar to those observed at 77K (See figure 17). The molecular motions such as torsional oscillations which are responsible for spin-lattice relaxation are generally very temperature dependent, and hence such motions cannot provide the dominant relaxation mechanism here. On the other hand cross-relaxation is relatively temperature independent, and has been shown to provide the primary relaxation pathway at very low temperatures (129). Similarly the nonaxiality of the g-, hyperfine, and quadrupole tensors for CO_2^- implies that molecular motion is restricted in the sodium formate lattice.

Thus these results are consistent with the suggestion that cross relaxation is a dominant relaxation route in irradiated sodium formate, and its relation to the irradiation dose may well explain the frequent failures to detect ENDOR signals in molecular crystals.

Chapter 5

ENDOR Studies of an X-irradiated Single Crystal of Potassium Hydrogen Bis Phenylacetate

5.1 Introduction

This study was undertaken to clarify an incomplete earlier study in these laboratories (130) in which the benzyl radical was identified in the single crystal EPR spectra of irradiated potassium hydrogen bis phenylacetate, $(C_6H_5CH_2COO)_2KH$, (KHBP). The spectral resolution in that case was limited by the inherent linewidths and by overlapping spectra from other species, and proved inadequate for detailed analysis. An ENDOR study of this system thus seemed to offer the best chance of determining the spectral parameters and hence of comparing calculated spin densities with experimental results. As discussed below the benzyl radical has received much theoretical attention, while there have been relatively few experimental results available for comparison.

The crystal structure of KHBP has been determined by Manojlović and Speakman (131) using X-ray diffraction methods and a single plane projection of the structure has been studied at 300 K and 120 K using neutron diffraction by Bacon and Curry (132, 133). There are small differences in the values obtained by neutron and X-ray diffraction, and comparable changes in the neutron

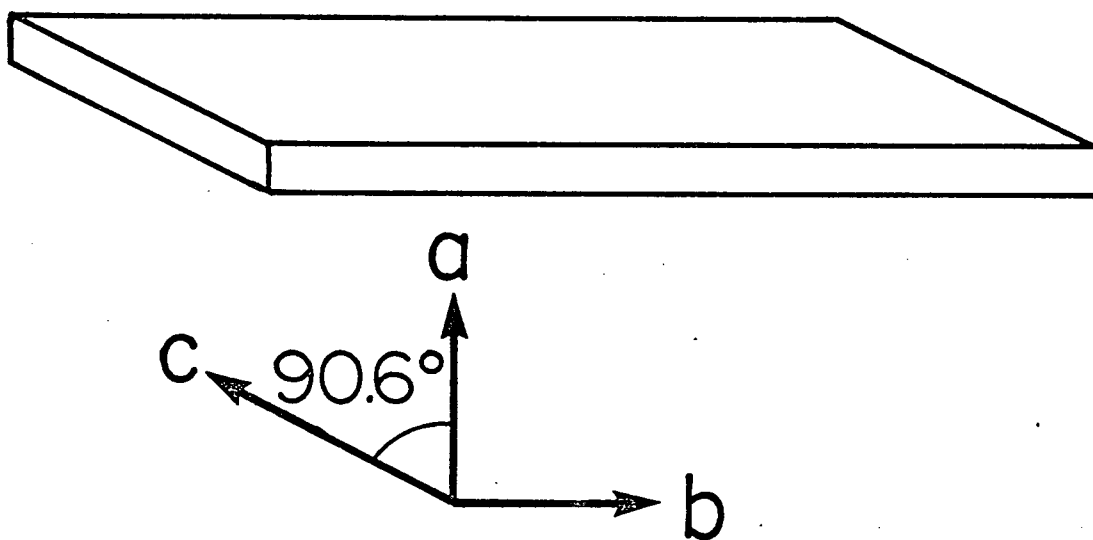


Fig. 18. External morphology and axis system for a single crystal of KHBP.

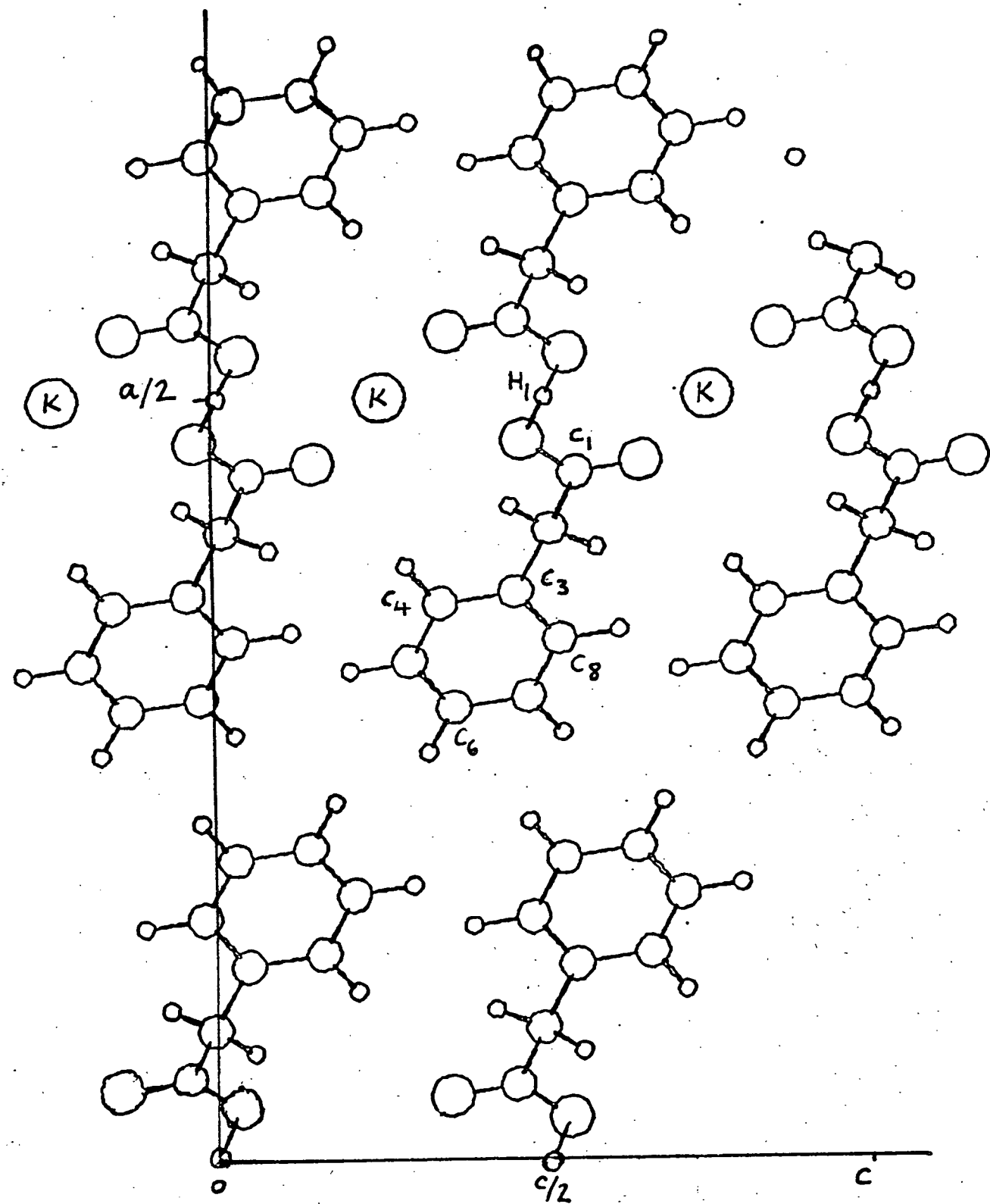


Fig. 19. Projection of part of the KHBP crystal lattice onto the ac plane.

diffraction results at the two temperatures studied. The results of Manojlović and Speakman showed that the crystal was monoclinic: space group $I2/a \equiv C2/c$, $Z=4$, $\beta=90.6^\circ$, $a=28.40$, $b=4.49$, $c=11.90$ Å. The crystal structure is shown in Fig. 19; the hydrogen atom H_1 lies at a centre of inversion and forms a symmetric $O...H...O$ hydrogen bond connecting the two phenylacetate residues.

In the course of the analysis, the direction cosines of C-H bonds inferred from ENDOR data were compared with the results of the crystal structure analysis. The agreement was generally good, except that the c components determined by the two methods differed by a sign, suggesting that some misassignment of axes had occurred.

Dr. J. C. Speakman (134) kindly confirmed that his published data were slightly in error, and that the correct value of β is 89.6° . This makes only a very small change in the numerical results but does invert the sign of third component of each vector (135) bringing the crystallographic results into agreement with the ENDOR findings.

Since an additional but undetermined small change in crystal structure occurs on cooling the crystal, no attempt was made to correct Speakman's parameters and his room-temperature results were used to interpret the ENDOR data after correction of the sign of the third direction cosine.

KHBP crystals had the form of plates elongated along the b axis; this feature together with the characteristic monoclinic site splittings in the bc and ab planes (Ch. 3) enables the axes to be located quite easily (Fig. 18). The orthogonal axis system $\underline{a}, \underline{b}, \underline{c}^*$ was chosen with $\underline{a} \times \underline{b} = \underline{c}^*$, and the magnetic field rotated in the three planes \underline{ab} , \underline{ac}^* , \underline{bc}^* as described in Ch. 3. Since β is close to 90° the orthogonal axes are of course essentially the same as the monoclinic axes $\underline{a}, \underline{b}, \underline{c}$.

5.2 The Benzyl Radical

The benzyl radical is one of the simplest odd-alternate neutral hydrocarbon radicals, and has been the object of considerable theoretical interest. Much of this attention has been devoted to calculation of the π electron spin densities since they provide a detailed test of the wave function which can thus, in principle, be compared with experimental results. Carrington and Smith (136) summarised some of the early work in this direction. Subsequently, Pople et al (137) developed the INDO approximation and calculations using this method have been repeatedly applied to spin density calculations on the benzyl radical (137, 138, 139). Kruglyac and Mozdor (140) performed self consistent configuration interaction calculations to various levels of approximation and discussed the significance of the different methods. More recently Raimondi et al (141) carried out an extensive Valence Bond calculation and compared the results with those of other calculations and of experiment.

The experimental estimates of the spin densities have hitherto been based on electron paramagnetic resonance studies of the benzyl radical undergoing free rotation either in solution (136, 142, 143) or in an adamantane matrix (144, 145). A recent study by Jones and Wood et al employed ^{13}C enrichment at the methylene and bridgehead carbons to infer the corresponding π -spin densities from the corresponding isotropic ^{13}C hyperfine couplings. This method relies on a McConnell-type relation (85) to estimate the effects of σ - π polarisation inducing spin in the carbon s-orbitals. All previous work used the simple McConnell relationship to obtain carbon π spin densities from the isotropic coupling of the corresponding α proton.

In addition to assuming the validity of the McConnell relationship or its ^{13}C analogue these methods have the limitation that they provide no direct structural information about the benzyl radical.

The conformation and geometry of the benzyl radical and its analogues have been the subject of several theoretical studies. Shansal (146) studied the SCF energy as a function of the geometry and orientation of the methylene group and showed that the in-plane configuration predicted by simple valence theory gave the minimum energy.

Lloyd and Wood (144) obtained the INDO-minimum energy geometry as a function of the positions of all 14 atoms. Their results again led to a planar geometry, but the H-C-H angle was reduced to 112° , and the carbon skeleton showed considerable quinonoid character. Hitherto there was no experimental evidence available with which direct comparison of any of these results could be made.

A major inadequacy of the results of calculations of the spin density distribution in the benzyl radical has been the relative size of the ortho and para spin densities. The isotropic proton couplings are in the ratio $a_{\text{para}}/a_{\text{ortho}}=1.22\pm0.03$, while the corresponding calculated spin density ratio is generally less than 1.

The great majority of INDO calculations show this trend, the calculated spin densities being typically $\rho_{\text{para}}\sim 0.25$, $\rho_{\text{ortho}}\sim 0.26$ for a ratio ~ 0.96 . In cases where the calculated spin densities have reflected the relative sizes of the proton couplings, the calculation have usually been questionable on other grounds. Thus Nanda and Narasimhan (147) in their UHF calculations obtained ortho and para couplings of 7.07 and 7.52G respectively, in reasonable agreement with experiment, but at the expense of a meta coupling calculated as 5.11 G compared with the experimental 1.95 G.

Similarly in their CI calculations Kruglyak and Mozdor (140) did obtain $\rho_{\text{para}} > \rho_{\text{ortho}}$ by including only six configurations, but they then comment, "This is an agreement with the experimental splittings if the simple McConnell

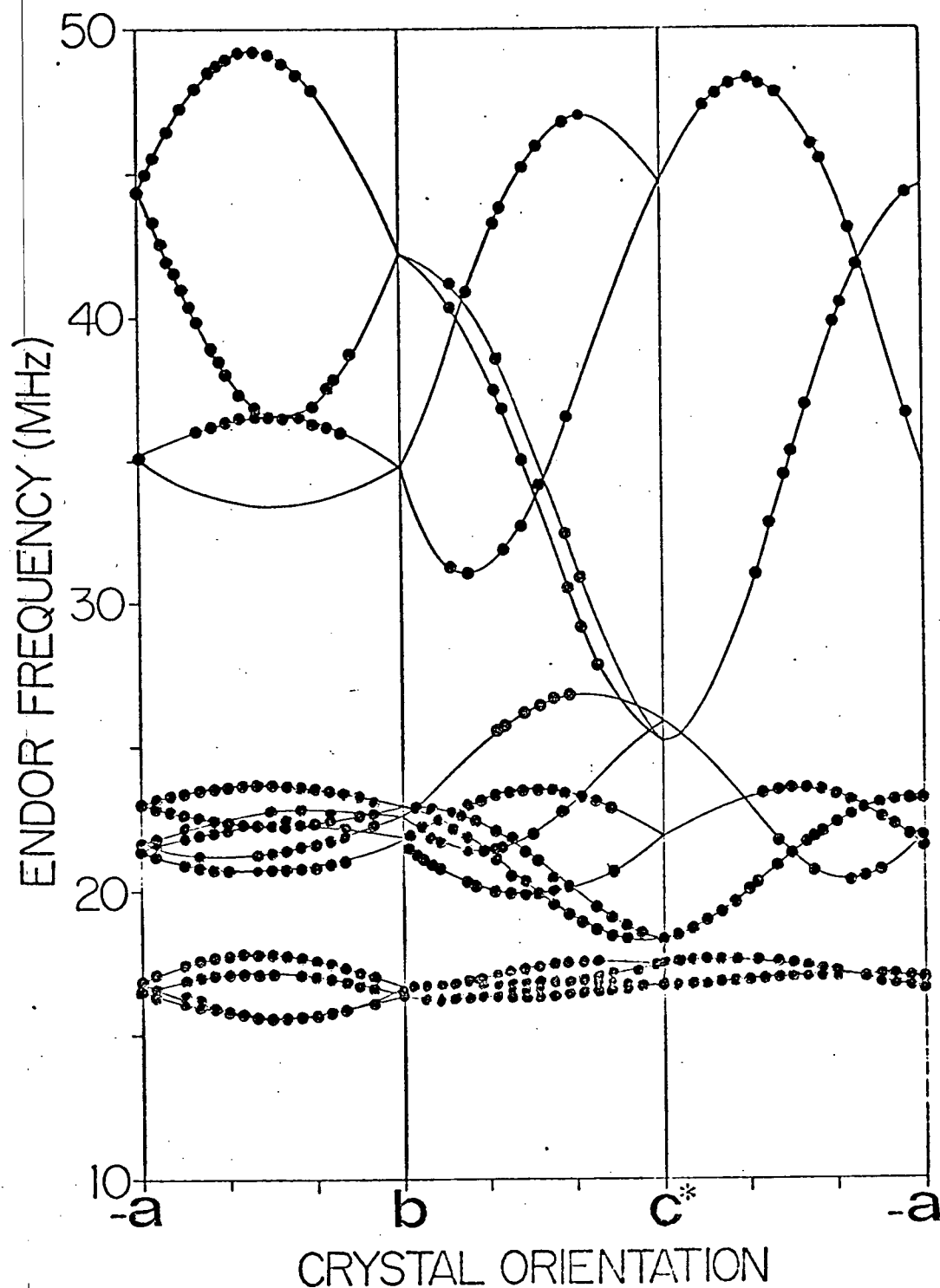


Fig. 20. Angular variation of the observed ENDOR frequencies for the protons of the benzyl radical in X-irradiated KHBP. The frequencies have been adjusted to a common free proton frequency of 14.3 MHz; the ENDOR linewidth, in all cases less than 0.1 MHz, is too small to be resolved on the scale of the Figure.

equation is used. This agreement must be considered as to be [sic] accidental for a more precise definition of the wavefunction by an extension of the CI basis as well as the use of open shell orbitals leads to an opposite relation between the spin densities on para- and ortho-atoms." In 1970 Kuprievich, Kruglyac and Mozdor (154) suggested that the McConnell relationship may be unreliable as an estimate of proton hyperfine couplings which differ by less than 1-2 G.

The main exceptions to this trend are the calculations of Simonetta et al (141) in which increasing the number VB structures from 14 to 784 altered the ratio $\rho_{\text{ortho}}/\rho_{\text{para}}$ from 0.599 to 1.075.

The advantage of an ENDOR study on the benzyl radical trapped in a crystalline matrix is that it enables the total, anisotropic proton coupling tensors to be determined. The dipolar parts can then be related to the radical geometry, and also used to provide an estimate of the spin density distribution which is independent of the validity of the McConnell relationship.

5.3 Results and Discussion: Benzyl Radical

The EPR spectra of X-irradiated crystals of KHBP at room temperature or 77K were ~120 G wide and poorly resolved (See Fig. 21). Preliminary ENDOR studies, saturating different parts of the EPR spectrum, established that more than one radical was present. In addition to a very large number of lines near the free proton n.m.r. frequency (~14.3 MHz), ENDOR transitions were observed at frequencies up to 50 MHz. The angular dependence of the ENDOR spectra studied by changing the orientation of the magnetic field by intervals of 2.5°, 5°, or 10°, depending on the density of lines, in the three perpendicular planes, ab, bc*, ac*. Fig. 20 shows the angular variation of the ENDOR transitions due to the benzyl radical in the planes of observation. For this

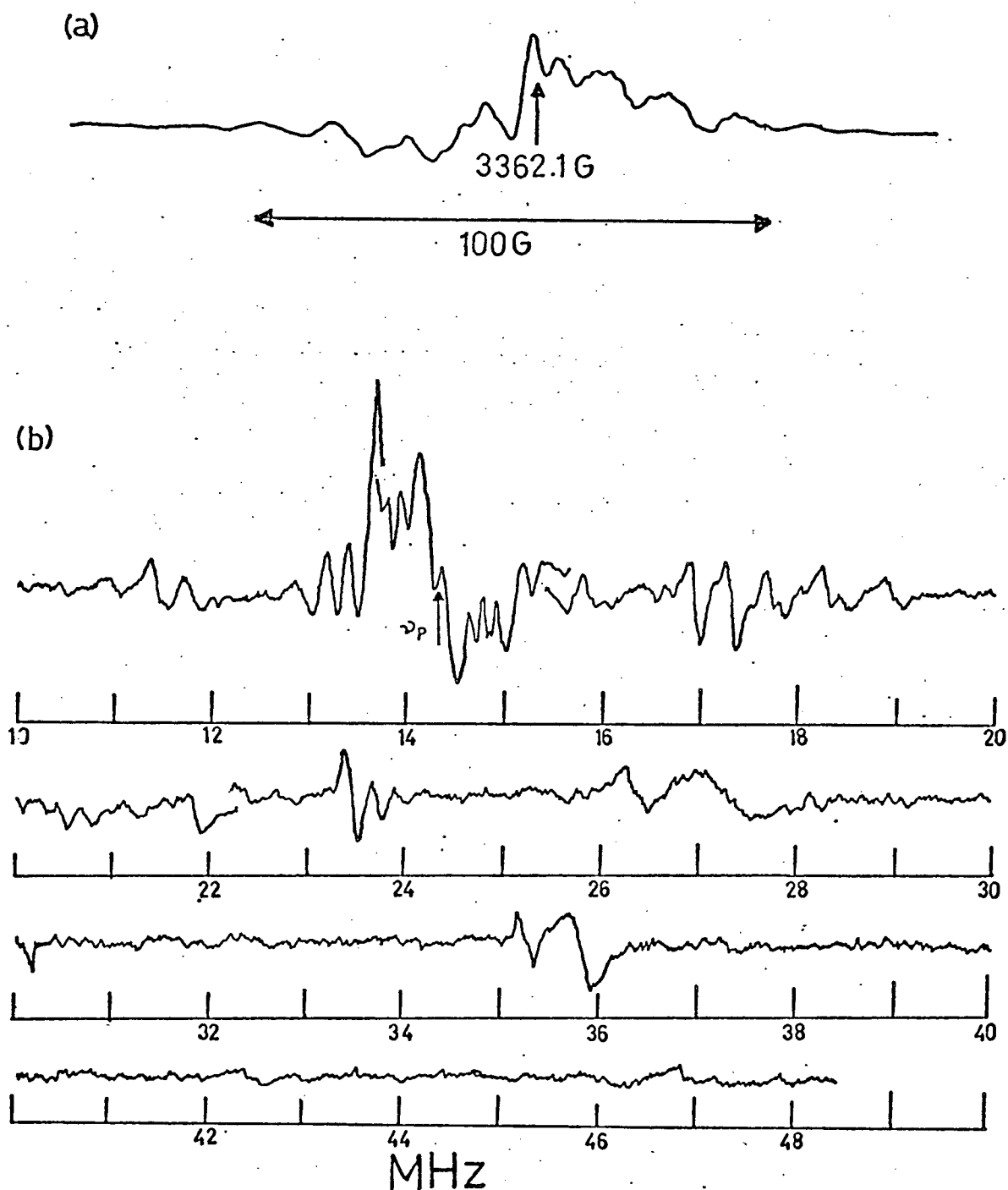


Fig. 21. Typical EPR (a) and ENDOR (b) spectra of X-irradiated KHBP obtained at 77K. The ENDOR spectrum was obtained by saturating the EPR spectrum at the point shown by the arrow. The breaks in spectrum (b) correspond to a change in oscillator band at 22 MHz, and a reduction in gain between 14 and 15.5 MHz.

figure the transition frequencies have been corrected to a free proton nmr frequency $\nu_p = 14.30$ MHz. The angular variation can be described by the usual spin Hamiltonian,

$$\mathcal{H} = \beta H \cdot \underline{g} \cdot \underline{S} + \sum (I^{(i)} \cdot \underline{A}^{(i)} \cdot \underline{S} - g_N \beta_N \sum H \cdot I^{(i)})$$

where \underline{g} is the electron g-tensor, \underline{S} the unpaired electron spin operator and $\underline{A}^{(i)}$ and $\underline{I}^{(i)}$ are respectively the hyperfine coupling tensor and nuclear spin operator for the i^{th} proton. This Hamiltonian does not contain the nuclear-nuclear dipolar term $\underline{I}_1 \cdot \underline{d} \cdot \underline{I}_2$ which has been observed in similar systems containing methyl or methylene groups (148, 149). The contribution of the dipolar interaction in such systems is less than 50 kHz, which is within the linewidth for the methylene proton ENDOR signals.

The anisotropic g-tensor components for the benzyl radical have not been reported; the results given in Appendix 1 suggest that it might be possible to estimate the g-anisotropy from its effect on the ENDOR frequencies. Attempts to do this by allowing the program LSF to refine the g-tensor were unsuccessful, however, the calculations failing to converge. Accordingly \underline{g} was taken as $g_{\text{iso}} = 2.0023$ for the analysis of the ENDOR data; this approximation is expected to introduce a negligible error. For the meta proton couplings both ENDOR transitions were used, but for the other couplings of the benzyl radical only the high frequency transition was observed.

Apart from the approximations mentioned above we made no assumption regarding the magnitude or orientation of any of the hyperfine tensors. The minimum number of points used to fit a tensor was 37, the maximum 84 and the rms error varied from ~100 kHz for the large couplings to ~20 kHz for the meta proton couplings. The main source of error is probably residual misalignment of the crystal, after the corrections described in Ch. 3 had been applied.

After the methylene proton couplings had been identified as belonging to the benzyl radical it was possible to assign the ortho and para couplings by comparing their isotropic parts to the values obtained by EPR. However, in order to pick out the ENDOR transitions of the meta protons from the large number of lines below 25 MHz it was necessary to predict their approximate angular variation. Accordingly the spin density obtained by EPR for the meta carbon was used in the equations of McConnell and Strathdee (99) and the approximate total hyperfine tensors reconstructed. The corresponding angular variation of the ENDOR frequencies was then calculated using the program FIELDS and used to select the appropriate set of data points. The self consistency of the results and their agreement with earlier work serve to justify this procedure.

The diagonalised forms of the hyperfine tensors so obtained are given in Table IV; in Table V the corresponding isotropic parts are compared with the values from EPR data. In both cases the signs of the tensors are chosen to be consistent with INDO results. Comparison of our results with those of other workers shows that there is only a small variation of the isotropic coupling constants with the environment of the radical. This allows us to neglect the effects of the crystal matrix and is consistent with the observations of Manojlović and Speakman (131) and of Bacon and Curry (133) that the benzene ring interacts relatively weakly with neighbouring molecules. The direction cosines in Table IV show that all the proton tensors have a common π direction (perpendicular to the ring). Apart from that of meta(2) ($\Delta\theta=6.5^\circ$) all the ' π ' vectors are within 3.6° of the mean, which itself is 7° from the normal to the benzene ring in the undamaged molecule. This result confirms the planarity of the benzyl radical and shows that no major reorientation in the crystal occurs as a result of radical formation. Similarly the ' σ ' direction for the para

Table IV Proton Hyperfine Tensors in the Benzyl Radical

Proton	rms Error, kHz	Principal Value MHz		Direction cosines [†]		
				ℓ	m	n
Methylene(1)	74.0	A_{π}^*	-40.22	0.6173	± 0.7855	0.0442
		A_{σ}	-20.29	-0.6587	± 0.5467	0.5175
		A_{\perp}	-70.31	-0.4303	± 0.2901	0.8548
Methylene(2)	90.0	A_{π}	-44.08	0.6372	± 0.7707	0.0022
		A_{σ}	-21.23	-0.0425	± 0.0315	0.9986
		A_{\perp}	-69.96	0.7697	± 0.6361	0.0534
Ortho(1)	50.0	A_{π}	-16.21	0.6758	± 0.7371	0.0020
		A_{σ}	- 7.78	-0.5689	± 0.5232	-0.6346
		A_{\perp}	-19.08	-0.4688	± 0.4277	0.7729
Ortho(2)	44.0	A_{π}	-15.85	0.6615	± 0.7496	0.0197
		A_{σ}	- 7.76	-0.0728	± 0.0903	-0.9933
		A_{\perp}	-18.77	0.7463	± 0.6556	0.1142
Meta(1)	23.5	A_{π}	2.69	0.6726	± 0.7397	0.0192
		A_{σ}	4.80	-0.5639	± 0.5292	-0.6340
		A_{\perp}	7.15	0.4791	± 0.4157	0.7731
Meta(2)	23.1	A_{π}	2.49	0.6543	± 0.7368	0.1703
		A_{σ}	4.86	-0.1297	± 0.1126	0.9852
		A_{\perp}	7.00	0.7450	± 0.6751	0.0190
Para	49.0	A_{π}	-17.05	0.6176	± 0.7841	0.0622
		A_{σ}	- 9.98	-0.7113	± 0.5230	0.4696
		A_{\perp}	-26.28	-0.03356	± 0.3342	-0.8807

* A_{σ} corresponds to the direction closest to the CH bond; A_{π} to the axis of the $2p_x$ orbital and A_{\perp} is perpendicular to both.

† The direction cosines are referred to the axis system a,b,c*, and the \pm signs chosen consistently relate one distinguishable crystal site to the other.

Table V Proton Isotropic Coupling Constants (MHz)
for the Benzyl Radical in Different Media

Medium	KHBP ^a	Aqueous Soln. ^c	Adamantane ^d
Methylene	-45.02 ^b	-45.78	-43.90
Ortho	-14.25 ^b	-14.39	-14.22
Meta	4.83 ^b	4.90	4.76
Para	-17.78	-17.19	-16.80

a This work b Average of (1) and (2) c Reference 136 d Reference 145.

Signs are chosen to be consistent with INDO results.

Table VI Angles ϕ_i° between σ vector of proton tensor i
and σ vector of para proton tensor

Tensor	Methylene(1)	Methylene(2)	Ortho(1)	Ortho(2)	Meta(1)	Meta(2)
ϕ°	120.8	121.0	111.6	112.3	67.7	60.3

proton coupling is within $5\frac{1}{2}^\circ$ of the corresponding direction in the undamaged crystal. This vector is expected to be the C_2 axis of the benzyl radical. Table VI lists the angles ϕ between the ' σ ' vector of the para coupling and the corresponding directions for the other couplings, and shows that the C_{2v} symmetry of the radical is essentially maintained in the KHBP lattice. The slight anomaly represented by the meta(2) proton is evidently a reflection of a small solid-state interaction; the published neutron scattering factors (133) show the two meta protons to be slightly inequivalent. The difference in the ENDOR parameters however is too small to affect the interpretation.

Since the methylene protons are much further from all other centres of spin density than from the methylene carbon and this is the largest spin density in the radical, these ' σ ' directions should lie very close to the true C-H bond directions. Calculations using the McConnell-Strathdee model suggest that the perturbations due to the other spin densities will shift the σ direction by 0.5° or less. The methylene σ directions thus imply an H-C-H bond angle of $118 \pm 2^\circ$. This of course is expected from simple valence theory but is in contrast to the result of the INDO calculation of Lloyd and Wood in which the minimum energy configuration corresponded to an HCH angle of 112° (144).

By symmetry the σ direction of the para coupling lies along the bond direction as shown above, but for the ortho and meta proton couplings, the presence of significant spin density on neighbouring carbon atoms will in general shift the ' σ ' direction of the hf tensor slightly away from the bond, and prevents us from inferring the CH bond directions directly.

In order to interpret the anisotropic parts of the hyperfine tensors we made use of the McConnell-Strathdee equations mentioned above, and attempted to reconstruct the anisotropic tensors using calculated and experimental spin densities. Using a Q value of -74 MHz and the McConnell relationship $a_i = Q\rho_i$ we estimated the π electron spin densities from the ENDOR coupling

constants. Using these values and an assumed spin density of -0.1 at the bridgehead carbon we obtained the tensor components shown in Table VII b where the experimental values are also shown for comparison. The $2p_{\pi}$ spin densities on all seven carbon atoms were included in the calculation of each tensor.

It can be seen that the agreement with experiment is quite good but that the calculated value of the para coupling is too large, and the sign of the π component of the methylene proton tensor is wrong. In an effort to remove the discrepancies, we considered three effects not included in the McConnell-Strathdee model. Firstly σ polarisation, inducing positive spin density in the carbon $2p_{\sigma}$ orbital can be ruled out because it would add an axial component to the hf tensor in a sense which would increase the discrepancy. Earlier work too has shown that σ polarisation can be neglected in such calculations. (99, 159)

A second possibility is motional averaging of the tensor components by torsional oscillations. This can be considered by the following model. Consider a tensor \underline{T} in a general axis system x, y, z . If the tensor is rotated in this frame by an angle θ about z , where $\theta(t)$ is the instantaneous angular displacement, the new tensor in the x, y, z frame is

$$\underline{T}'(t) = \underline{R}^T(\theta) \cdot \underline{T} \cdot \underline{R}(\theta) \quad (5.1)$$

where \underline{R} is the rotation matrix

$$\begin{bmatrix} \cos\theta & -\sin\theta & 0 \\ \sin\theta & \cos\theta & 0 \\ 0 & 0 & 1 \end{bmatrix}$$

$T'(t)$ is thus readily obtained in terms of θ . The 'observed' tensor \bar{T} will be the time average of T' . To evaluate this one assumes a simple harmonic oscillation so that $\theta = \theta_0 \cos \omega t$, and expands the trigonometric functions as power series in θ .

Thus for example

$$\begin{aligned}\sin \theta &= \theta - \frac{1}{6} \theta^3 + \dots = \theta_0 \cos \omega t - \frac{1}{6} \theta_0^3 \cos^3 \omega t + \dots \\ \cos \theta &= 1 - \frac{1}{2} \theta^2 + \dots = 1 - \frac{1}{2} \theta_0^2 \cos^2 \omega t + \dots\end{aligned}\quad (5.2)$$

The time averages of these functions are now obtained by integrating t over one period and dividing by 2π . The calculation is simplified by noting that $\sin \theta$ is an odd function of $\cos \omega t$ and hence must average to zero. For $\theta_0 \lesssim 0.5$ radians the cosine series converges rapidly and the final result for the elements of \bar{T} is, to terms in θ_0^2 ,

$$\begin{aligned}\bar{T}_{\alpha\alpha} &= T_{\alpha\alpha} (1 - \frac{1}{2} \theta_0^2) + T_{\beta\beta} \frac{1}{2} \theta_0^2 \\ \bar{T}_{\alpha z} &= T_{\alpha z} (1 - \frac{1}{4} \theta_0^2), \quad \alpha, \beta = x, y \\ \bar{T}_{xy} &= T_{xy} (1 - \theta_0^2). \\ \bar{T}_{zz} &= T_{zz}.\end{aligned}\quad (5.3)$$

Note that the trace is conserved, the xx and yy elements are mixed and the off diagonal elements reduced in magnitude.

The motional parameters for KHBP obtained by neutron diffraction (133) indicate that θ_0 decreases from $\sim 5^\circ$ to $\sim 4^\circ$ between 300 K and 120 K, so at 77 K we can safely take $\theta_0 < 0.1$ rad, with the result that motional averaging cannot produce an effect greater than ~ 0.2 MHz for even the methylene coupling.

The third contribution we considered was the effect of off-diagonal elements of the spin density matrix. Our INDO calculation showed that several of these were significant, (Fig.22) notably values of $\rho = -0.23$ from the ortho-

Table VII Proton Dipolar Coupling Tensors in Benzyl Radical (MHz)

		a	b	c	d
Methylene	D_{π}	0.86	-0.15	-0.09	-3.40
	D_{σ}	24.26	26.93	26.48	26.79
	D_{\perp}	-25.12	-26.78	-26.39	-23.39
	ϕ°	121	121	121	121
Ortho	D_{π}	-1.79	-2.29	-2.27	-1.85
	D_{σ}	6.47	7.61	7.26	6.25
	D_{\perp}	-4.68	-5.32	-4.99	-4.40
	ϕ°	112	109	110	109
Meta	D_{π}	-2.24	-2.66	-2.66	-2.28
	D_{σ}	-0.01	0.47	0.47	0.14
	D_{\perp}	+2.25	2.19	2.19	2.14
	ϕ°	64	66	66	79
para	D_{π}	0.72	-0.77	-0.76	-0.32
	D_{σ}	7.79	11.27	11.04	8.27
	D_{\perp}	-8.51	-10.50	-10.28	-7.95
	ϕ°	0	0	0	0

a Experimental b Calculated using spin densities from McConnell relationship.

c As for b, plus terms due to off-diagonal spin densities.

d Calculated using the following spin densities: methylene 0.64, bridgehead -0.11 ortho, para 0.16 meta -0.05.

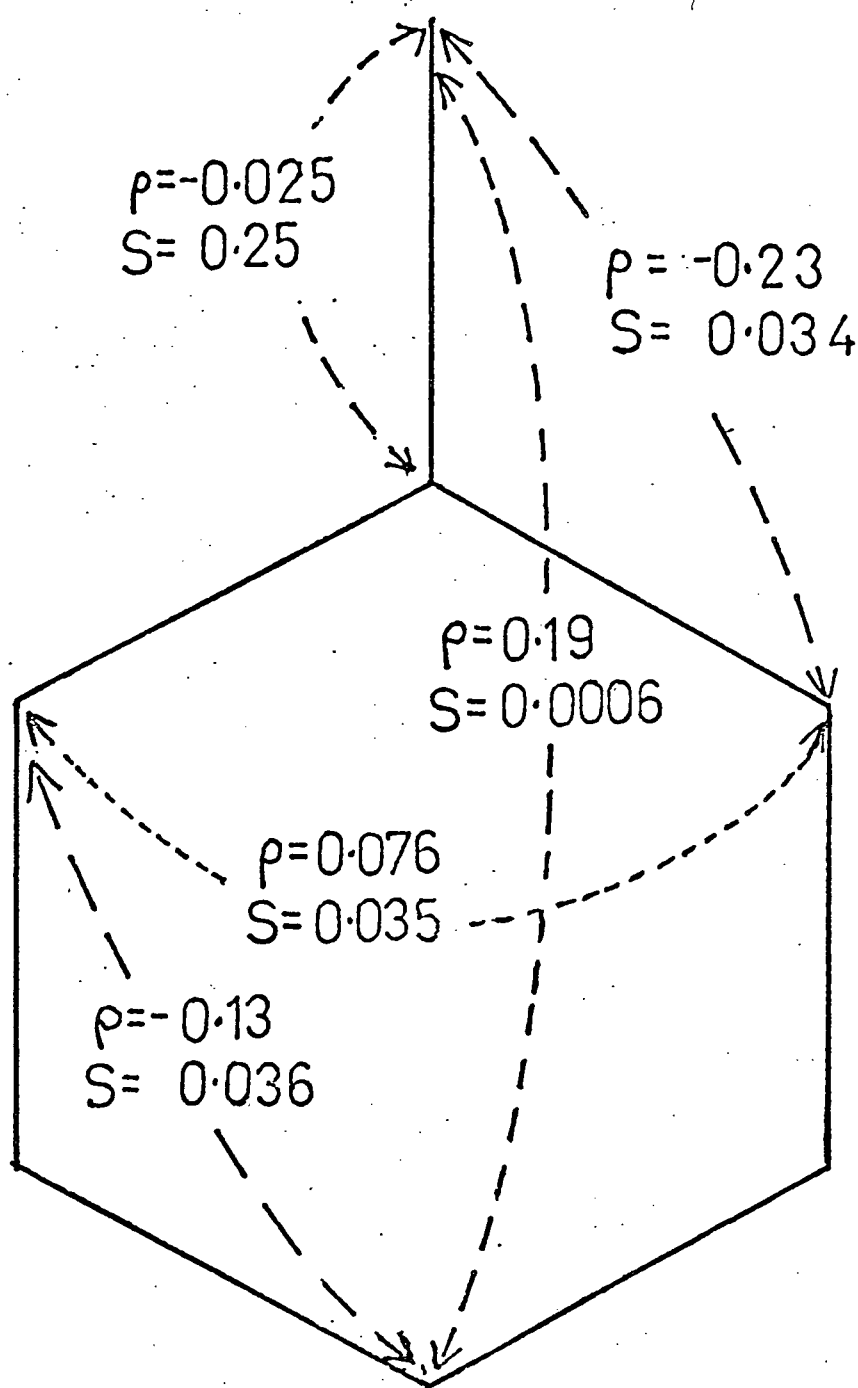


Fig. 22. INDO overlap spin densities in the benzyl radical. The corresponding overlap integrals, S , are also shown.

methylene π orbitals and $\rho = +0.19$ from the methylene-para overlap. Comparison with the corresponding values of the products $c_i c_j$ of the molecular orbital coefficients showed that these off diagonal spin densities were predominantly overlap rather than polarisation terms. We estimated their contribution to the total tensors using Mulliken's approximation (103). The overlap integral $S \equiv \langle 2p_x^A | 2p_x^B \rangle$ was obtained from the INDO results, and the one-centre integrals were evaluated using the McConnell Strathdee equations. The result of adding these terms is shown in Table VII where it can be seen that a small improvement in the calculated values results.

It is interesting to compare these results with the valence bond calculations of Raimondi et al (141), in which increasing the number of participating valence bond configurations strikingly improved the calculated spin densities. Formally the effect of off-diagonal spin densities in an LCAO approach is equivalent to the contribution of different valence bond structures as cross terms in the evaluation of the dipolar tensors, as outlined in Ch. 2.

However after including these terms the calculated para coupling is still significantly larger than experimental value. No reasonable variation of parameters in the McConnell-Strathdee model reproduced this trend without requiring the ortho and para spin densities to be approximately equal; the results of one such calculation are given in Table VIId. This observation recalls the tendency of most calculations (136-7, 140-1, 144, 150-1) to predict $\rho_{\text{ortho}} > \rho_{\text{para}}$ and suggests that there may be some physical significance to the result. Although the valence bond configurations included by Raimondi clearly do contribute as shown above, some doubt remains as to the magnitude of their effect. This is particularly true since there is no marked trend in the ratio $\rho_{\text{ortho}}/\rho_{\text{para}}$ when the benzyl radical is studied in environments of

different polarity (Table V) or undergoes F or Cl substitution (144, 152-3). The strong variation in $\rho_{\text{ortho}}/\rho_{\text{para}}$ with the number of ionic configurations in the valence bond model makes this observation a little surprising.

It seems possible then that part of the discrepancy between the majority of INDO calculations and the isotropic proton coupling tensors determined experimentally is due to a failure of the simple McConnell relationship for the para coupling. This suggestion has also been made by Kuprievich, Kruglyak and Mozdor (154). A direct way of deciding this point would be to measure the ^{13}C hyperfine couplings at the ortho and para positions. We know of no such studies, although Lloyd and Wood et al (14b) have measured the ^{13}C couplings of the methylene and bridgehead carbons.

Recent EPR studies of the similar nitrobenzene anion radical have determined ^{13}C and ^1H hyperfine couplings (158); in this case however the experimental results seem consistent with the qualitative predictions of calculations.

5.4 Other Radicals

This study of KHPB illustrates the level of complexity which can result when ENDOR studies are made on a system with a large number of protons. Since the characterisation of the benzyl radical was the main object, ENDOR lines above 50 MHz were not studied. But even in the frequency range studied, 10-50, MHz, a total of the order of 5000 data points were obtained. This volume of data presented considerable difficulty in analysis; preliminary fitting to assign points to a given coupling was essential but often difficult.

Excluding the frequency range $14 \pm 3\text{MHz}$ which is likely to contain lines from intermolecular couplings there were indications of at least 40 couplings in the frequency range studied. The majority of these must be intramolecular,

and imply the existence of at least five radicals. However, low signal-to-noise ratios prevented the angular variation of most of these couplings from being followed far enough to determine the tensors; radical decay caused many lines to appear in one plane only. Thus, in addition to the difficulty of extracting coupling tensors from the data there is the problem of assigning them to individual radicals. Saturation of different points on the EPR spectrum was not of great help here: the resulting variation in the ENDOR spectra confirmed the existence of more than one radical but with the exception of a very few lines the spectra themselves were too complex for correlations to be made.

For these reasons the interpretation of the results must be a little more tentative than for the benzyl radical. Nevertheless, an interpretation was possible, and the 8 couplings given in Table VIII were assigned using the following arguments.

Tensors 1, 2, and 3 of Table VIII show the large, almost isotropic character of typical β proton couplings in a π radical. (For these large tensors there is an ambiguity as to whether the observed ENDOR line is $\nu <$ or $\nu >$ i.e. $|a/2 + \nu_p|$ or $|a/2 - \nu_p|$, but this question can usually be resolved by varying ν_p and noting whether the ENDOR line shifts in the same or opposite sense.) The size of the isotropic parts suggests that these β protons are interacting with two centres of spin density (cf Ch. 2); the markedly non axial character of the dipolar parts leads to the same conclusion and implies that the radicals containing these β protons are formed by the addition of a hydrogen atom to the benzene ring. In such a radical the three main centres of spin density are ortho and para to the point of H-addition.

The radical so formed would be analogous to the cyclohexadienyl radical described in Ch. 2, and the results for this can be used in interpreting the

Table VIII
Hyperfine Tensors for Radicals I and II

Tensor	a_{iso} MHz	Dipolar Part. MHz	Direction Cosines		
1	119.3	5.06	-0.972	∓ 0.029	0.232
		-0.06	0.232	∓ 0.019	0.973
		-5.01	-0.024	± 0.9994	0.02515
2	115.02	4.08	0.342	∓ 0.783	0.520
		-0.441	-0.533	± 0.294	0.793
		-3.64	0.774	± 0.548	0.317
3	120.77	6.05	0.784	∓ 0.462	0.413
		-0.02	-0.213	± 0.426	+0.879
		-6.04	-0.581	∓ 0.776	0.235
4	-37.49	18.38	0.688	± 0.409	0.600
		0.03	-0.450	± 0.878	-0.090
		-18.40	0.571	± 0.209	-0.795
5	7.08	-3.63	-0.542	∓ 0.833	-0.114
		0.18	0.840	∓ 0.534	-0.096
		3.44	0.019	∓ 0.147	0.989
6	7.16	-3.60	-0.556	∓ 0.829	-0.0532
		0.356	-0.019	∓ 0.077	0.997
		3.24	-0.831	∓ 0.553	0.059
7	21.17	-1.16	-1.16	∓ 0.086	-0.911
		-4.32	-4.32	∓ 0.850	0.146
		5.48	5.48	∓ 0.520	0.385
8	40.39	-1.66	-1.66	∓ 0.721	-0.683
		-1.82	-1.82	∓ 0.529	0.472
		3.47	3.47	∓ 0.441	0.552

Table IX Hyperfine Tensors in the Cyclohexadienyl
and α -Naphthyl Radicals

Cyclohexadienyl		α -Naphthyl		Dipolar part. (MHz)
Proton	a(MHz)	a(MHz)		
Methylene	+133.6	+101.8, 90.4		
o	-25.17	-30.15	15.36	
			1.16	
			-16.5	
m	7.42	7.7	0.12	
			3.8	
			-3.92	
p	-36.57	-36.41	19.17	
			0.88	
			-20.08	

present data. Table IX shows the isotropic couplings obtained by Fessenden and Schuler (155) in their EPR study of cyclohexadienyl, together with the total proton tensors derived from the ENDOR study by Böhme and Wolf (156) of the closely related α hydronaphthyl radical. (INDO calculations on related systems give similar results, but predict almost equal spin densities at the three main centres.) The main features of these results in addition to the large β couplings are the characteristic α couplings to the three centres of positive spin density, and the relatively large negative spin densities at the two meta positions.

The β couplings in KHBP can be tentatively assigned by their dipolar parts.

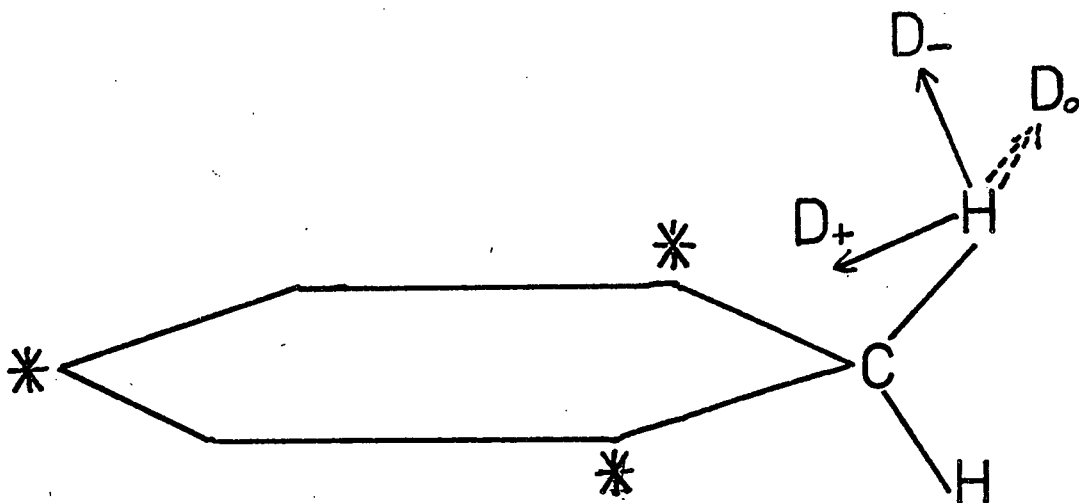


Fig. 23. Proton dipolar hyperfine principal vectors in cyclohexadienyl. The three main centres of positive spin density are starred.

Because of the sp^3 hybridisation of the methylene carbon, which causes the methylene hydrogens to lie above and below the ring, the dipolar directions will not lie in the radical plane. This makes β couplings in an aromatic system harder to assign than α couplings; however, simple consideration of the dipolar interaction between such a methylene proton and the two β centres of spin density (Fig.23) shows that the most negative principal value, D_- , of the dipolar tensor will be inclined at $20-30^\circ$ to the perpendicular to the ring. Similarly one of the positive principal values, D_+ , will correspond to a direction inclined at $20-30^\circ$ to the original aromatic C-H bond, but its projection in the ring plane will be along that bond. By projecting the principal vectors of the coupling tensors onto the radical plane it is possible to assign tensor 1 to hydrogen addition at C_6 (Radical I) and tensors 2 and 3 to hydrogen addition at C_4 or C_7 . (Radical II)

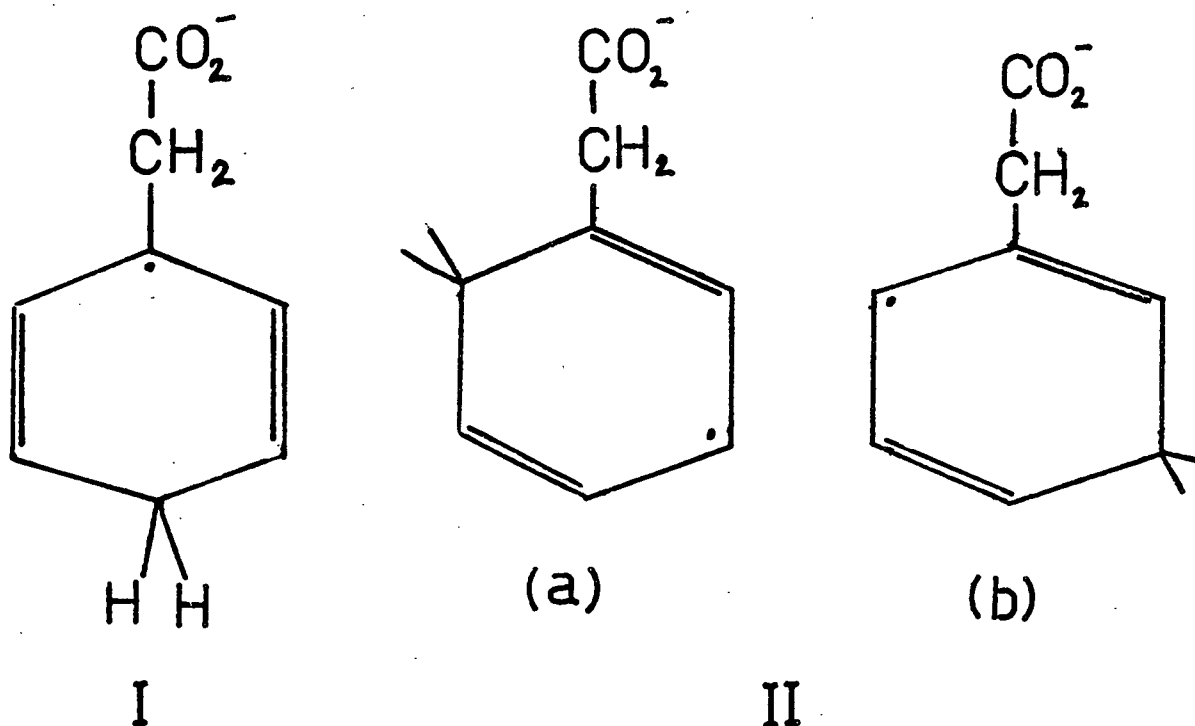


Fig. 24. Assignment of hydrogen addition radicals I and II.

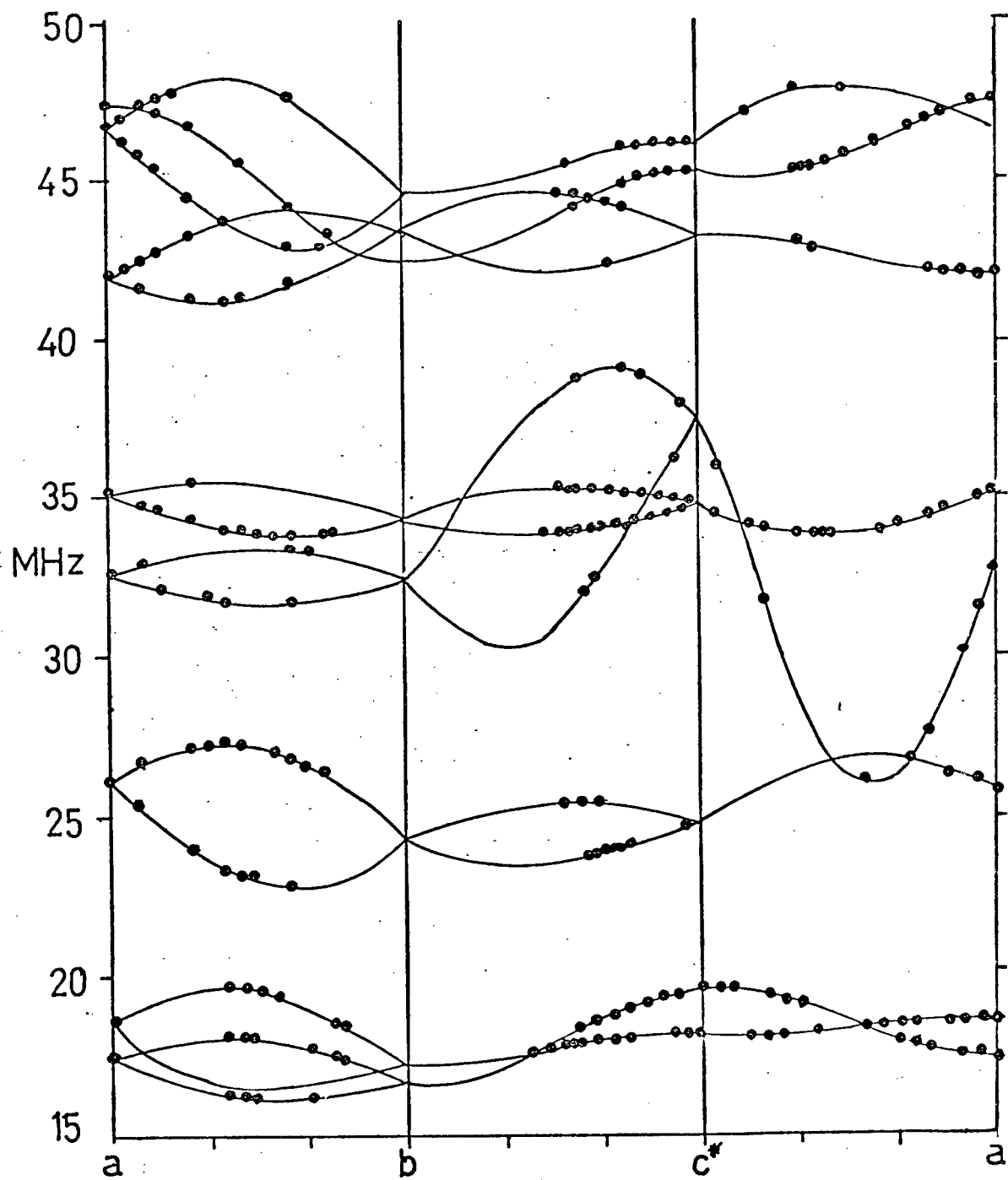


Fig. 25. Angular variation of ENDOR spectra for radicals I and II.

These latter two possibilities cannot be distinguished by the β couplings alone as the C_4-H_4 and C_7-H_7 directions are essentially colinear. The addition at C_6 is relatively unambiguous, since the only alternative would be H addition at the bridgehead carbon which is highly unlikely because of steric hindrance.

The α coupling, 4 has its direction parallel to C_4H_4 or C_7H_7 and its magnitude is similar to the para coupling of cyclohexadienyl; thus 4 is assigned to the para position of radical II, viz C_7 or C_4 .

The ENDOR lines associated with tensors 5, 6 and 7 weakened simultaneously when the saturation point of the EPR spectrum was altered; these three tensors are therefore assigned to the same radical. Of these, tensors 5 and 6 are typical meta couplings of a cyclohexadienyl type radical, while 7 is a β type coupling in which the proton interacts with a single centre of spin density.

This latter coupling is consistent with proton H_2 of the original methylene group in KBHP. The ' β ' spin density would be at the bridgehead carbon: this could arise from H-addition at either C_6 or C_4 but not at C_7 ; furthermore H-addition at C_7 would give rise to only one 'meta' coupling, the other position of negative spin density being the bridgehead carbon. Thus the tensors 5, 6 and 7 are consistent with hydrogen addition at either C_6 or C_4 but not at C_7 . The latter possibility is also opposed by chemical intuition which would predict addition to occur o- and p- to the CH_2COO group rather than m- and p-. The final assignments of these three tensors is less certain and must be based on the directions of the 'meta' dipolar tensors. By analogy with the meta couplings of the benzyl and α naphthyl radicals, the dipolar value closest to zero corresponds to the bond direction. Projecting the corresponding principal vectors onto the ring plane shows that C_6 and C_4 rather than C_8 and C_4 are the more likely assignments, so tensors 5, 6, 7

are tentatively assigned to radical II(a).

The spin density at the bridgehead carbon in radical II is likely to be ~0.4 from the data in Table IX; using this value in equation 2-45 with $B_0=9$ $B_1=122$ MHz predicts a dihedral angle of 53° , in reasonable agreement with the value 64° for H_2 from the room temperature crystal structure data. Uncertainties in B_0 and B_1 and a possible reorientation of the radical at low temperatures make this estimate reasonable. In particular B_1 may be too low; a value of 150 MHz (157) has been suggested and would give better agreement with the values at C_6 , C_4 .

The dihedral angle corresponding to proton H_3 is 139° and would lead to an isotropic coupling ~30-40 MHz. The tensor 8 with $a=40.4$ MHz is in reasonable agreement, but its anisotropic part is anomalous; the positive principal direction is 23° from C_3H_3 and so the assignment of tensor 9 to proton H_3 of radical II must remain conjectural.

REFERENCES

1. C.D. Jeffries in Progress in Cryogenics (Heywood & Co. Ltd., London, 1961).
2. A. Abragam in The Principles of Nuclear Magnetism (Clarendon, Oxford, 1961).
3. C.D. Jeffries, Phys. Rev., 117, 1056 (1960).
4. A.W. Overhauser, Phys. Rev., 92, 411 (1953).
5. T.R. Carver and C.P. Slichter, Phys. Rev., 102 (1956).
6. A. Abragam, Phys. Rev., 98, 1729 (1955).
7. G. Feher, Phys. Rev., 103, 500 (1956).
8. G. Feher, Phys. Rev., 103, 834 (1956).
9. G. Feher, Phys. Rev., 114, 1219 (1959).
10. W.C. Holton, H. Blum and C.P. Slichter, Phys. Rev. Letters, 5, 197 (1960).
11. R.J. Cook and D.H. Whiffen, Proc. Roy. Soc. A, 295, 99 (1966).
12. see for instance I.L. Bass and R.L. Mieher, Phys. Rev., 175, 421 (1968).
13. H. Seidel and H.C. Wolf in Physics of Color Centres, ed. W.B. Fowler (Academic Press, New York, 1968).
14. H. Seidel and H.C. Wolf, Phys. Stat. Solidi, 11, 3 (1965).
15. V.G. Grachev, M.F. Deigen, G.I. Neimark and S.I. Pekar, Phys. Stat. Solidi B, 43, K93 (1971).
16. see for example C.P. Scholes, R.A. Isaacson and G. Feher, Biochim., Biophys. Acta, 263, 448 (1972).
17. G.H. Rist, J.S. Hyde and T. Vanngard, Proc. Nat. Acad. Sci. U.S., 67, 79 (1970).
18. G.H. Rist and J.S. Hyde, J. Chem. Phys., 49, 2449 (1968).
19. see for example C.A. Hutchison and G.A. Pearson, J. Chem. Phys., 43, 2545 (1965).
20. C.A. Hutchison, J. Phys. Chem., 71, 203 (1967).
21. C.A. Hutchison, Pure Appl. Chem., 27, 327 (1971).
22. S.N. Rustgi and H.C. Box, J. Chem. Phys., 59, 4763 (1973).

23. J.N. Herak and C.A. McDowell, J. Mag. Reson., 16, 434 (1974).
24. M. Iwasaki and H. Muto, J. Chem. Phys., 61, 5315 (1974).
25. F.Q. Ngo, E.E. Budzinski and H.C. Box, J. Chem. Phys., 60, 3373 (1974).
26. J.Y. Lee and H.C. Box, J. Chem. Phys., 59, 2509 (1973).
27. H.C. Box, E.E. Budzinski and K.T. Lilga, J. Chem. Phys., 57, 4295 (1972).
28. H.C. Box, H.G. Freund, K.T. Lilga and E.E. Budzinski, J. Phys. Chem., 74, 40 (1970).
29. S.N. Rustgi and H.C. Box, J. Chem. Phys., 60, 3343 (1974).
30. J.N. Herak, D.R. Lenard and C.A. McDowell, J. Mag. Reson. (to be published).
31. H.C. Box, E.E. Budzinski and W.R. Potter, J. Chem. Phys., 61, 1136 (1974).
32. A.L. Kwiram, J. Chem. Phys., 49, 2860 (1968).
33. L.R. Dalton and A.L. Kwiram, J. Chem. Phys., 57, 1132 (1972).
34. J.S. Hyde, G.H. Rist and L.E.G. Eriksson, J. Phys. Chem., 72, 4269 (1968).
35. R.D. Allendoerfer, Chem. Phys. Letters, 17, 172 (1972).
36. J. Helbert, L. Kevan and B.L. Bales, J. Chem. Phys., 57, 723 (1972).
37. L.E.G. Eriksson, J.S. Hyde and A. Ehrenberg, Biochem. Biophys. Acta, 192, 211 (1969).
38. J.R. Norris, M.E. Druyan and J.J. Katz, J. Amer. Chem. Soc., 95, 1680 (1973).
39. H.L. Van Camp, C.P. Scholes and C.F. Mulks, J. Amer. Chem. Soc., 98, 4094 (1976).
40. D.E.B. Kennedy, Ph.D. Thesis, University of British Columbia, 1974.
41. H. van Willigen, M. Plato, R. Biehl, K.P. Dinse and K. Möbius, Mol. Phys., 26, 793 (1973).
42. R.A. Allendoerfer in Magnetic Resonance, ed. C.A. McDowell (MTP Reviews of Science, Butterworths, London, 1974).
43. R.J. Cook and D.H. Whiffen, Proc. Phys. Soc. (London), 84, 845 (1964).
44. N.S. Dalal, S.R. Srinivasan and C.A. McDowell, Chem. Phys. Letters, 6, 617 (1970).
45. K.P. Dinse, R. Biehl and K. Möbius, J. Chem. Phys., 61, 4335 (1974).

46. I.Y. Chan, J. Schmidt and J.H. van der Waals, Chem. Phys. Letters, 4, 269 (1969).
47. L.T. Cheng, J. van Lee and A.L. Kwiram, Bull. Am. Phys. Soc., 15, 268 (1970).
48. M.J. Buckley, C.B. Harris and A.H. Maki, Chem. Phys. Letters, 4, 591 (1970).
49. P.D. Parry, T.R. Carver, S.O. Sari and S.E. Schnatterly, Phys. Rev. Letters, 22, 326 (1969).
50. A. Abragam and B. Bleaney in Electron Paramagnetic Resonance of Transition Metal Ions (Clarendon, Oxford, 1970) Ch. 1, 4.
51. A.L. Kwiram, Ann. Rev. Phys. Chem. 22, 133 (1971).
52. N.S. Dalal, C.A. McDowell and J.M. Park, J. Chem. Phys., 63, 1856 (1975).
53. J.M. Park and C.A. McDowell, Mol. Phys. (in Press).
54. M.H.L. Pryce, Proc. Phys. Soc. (London), A63, 25 (1950).
55. A. Abragam and M.H.L. Pryce, Proc. Roy. Soc. (London), A205, 135 (1951).
56. G.E. Pake and T.L. Estle in The Physical Principles of Electron Paramagnetic Resonance, 2nd Ed. (Benjamin, Reading, 1973).
57. C.P. Slichter in Principles of Magnetic Resonance (Harper and Row, New York, 1963) Ch. 4 and 7.
58. A. Carrington and A.D. McLachlan in Introduction to Magnetic Resonance (Harper and Row, New York, 1967) Ch. 9.
59. A. Abragam and B. Bleaney in Electron Paramagnetic Resonance of Transition Metal Ions (Clarendon, Oxford, 1970) Ch. 1, 4.
60. J.M. Baker and F.I.B. Williams, Proc. Roy. Soc., A267, 283 (1962).
61. N.S. Dalal, J.A. Hebden and C.A. McDowell, J. Mag. Reson., 16, 289 (1974).
62. H.F. Hameka in The Triplet State, ed. A.B. Zahlan et al, (Cambridge U.P., London, 1967), A.J. Stone, Proc. Roy. Soc. A 271, 424 (1963).
63. J.B. Farmer, private communication.
64. C.P. Slichter in Principles of Magnetic Resonance (Harper and Row, New York, 1963) Ch. 6.
65. L.R. Walker, G.K. Wertheim and V. Jaccarino, Phys. Rev. Letters, 6, 98 (1961).
66. A.L. Kwiram, J. Chem. Phys., 55, 2484 (1971).

67. M. Iwasaki, J. Mag. Reson., 16, 417 (1974).
68. W.C. Lin, Mol. Phys., 25, 1163 (1973).
69. A. Rockenbauer and P. Simon, Molec. Phys., 28, 1113 (1974).
70. R. Skinner and J.A. Weil, J. Mag. Reson., 21, 271 (1976).
71. D.H. Whiffen, Mol. Phys., 10, 595 (1965).
72. N.M. Atherton and D.H. Whiffen, Mol. Phys., 3, 1 (1960); H.A. Farach and C.P. Poole, Adv. in Mag. Reson., 5, 229 (1971).
73. R.E. Bellis and S. Clough, Mol. Phys., 4, 135 (1961).
74. J.A.R. Coope, N.S. Dalal, C.A. McDowell and R. Srinivasan, Mol. Phys., 24, 403 (1972).
75. K. Minakata and M. Iwasaki, Mol. Phys., 23, 1115 (1972).
76. V.V. Teslenko, Y.S. Gromovoi and V.G. Krivenko, Mol. Phys., 30, 425 (1975).
77. A. Carrington and A.D. McLachlan in Introduction to Magnetic Resonance (Harper and Row, New York, 1967) Ch. 1.
78. N.S. Dalal, Ph.D. Thesis, University of British Columbia (1971).
79. J. Lambe, N. Laurant, E.C. McIrvine and R.W. Terhune, Phys. Rev., 122, 1161 (1961). T. Cole, C. Heller and J. Lambe, J. Chem. Phys., 34, 1447 (1961).
80. J.M. Baker and W.B.J. Blake, J. Phys. C: Solid St. Phys., 6, 3501 (1973).
81. J.H. Freed, Ann. Rev. Phys. Chem., 23, 265 (1972).
82. C.A. Coulson in Valence (O.U.P., 1961, London), Ch. VIII.
83. N.S. Dalal, C.A. McDowell and R. Srinivasan, Chem. Phys. Letters, 4, 97 (1969).
84. G. Fraenkel and B. Venkataraman, J. Chem. Phys., 24, 737 (1956).
85. H.M. McConnell and D.B. Chestnut, J. Chem. Phys., 28, 107 (1958).
86. D.R. Eaton and W.D. Phillips, Adv. in Mag. Reson., 1, 103 (1965).
87. J.P. Colpa and J.R. Bolton, Mol. Phys., 6, 273 (1963).
88. G. Giacommetti, P.L. Nordio and M.W. Pavan, Theor. Chim. Acta, 1, 404 (1963).
89. M.T. Melchior, J. Chem. Phys., 50, 511 (1969).

90. A.D. McLachlan, Mol. Phys., 3, 233 (1960).
91. C. Heller and H.M. McConnell, J. Chem. Phys., 32, 1535 (1960).
92. W. Derbyshire, Mol. Phys., 5, 225 (1962).
93. J. Maruani, A. Hernandez-Laguna and Y.G. Smeyers, J. Chem. Phys., 63, 4515 (1975).
94. J. Maruani, Mol. Phys., 30, 1685 (1975).
95. D.H. Marcellus, E.R. Davidson and A.L. Kwiram, Chem. Phys. Letters, 33, 522 (1975).
96. R. Bersohn, J. Chem. Phys., 24, 1066 (1956).
97. D.H. Whiffen, Mol. Phys., 6, 223 (1963).
98. K. Morokuma and K. Fukui, Bull. Chem. Soc. Japan, 36, 534 (1963).
99. H.M. McConnell and J. Strathdee, Mol. Phys., 2, 129 (1959).
100. R.M. Pitzer, C.W. Kern and W.N. Lipscomb, J. Chem. Phys., 37, 267 (1962).
101. M. Barfield, J. Chem. Phys., 53, 3836 (1970).
102. F.G. Herring, C.A. McDowell and J.C. Tait, J. Chem. Phys., 57, 4564 (1972).
103. R.S. Mulliken, J. Chem. Phys., 46, 497 (1949).
104. M.H.L. Pryce, Nuovo Cimento, Suppl. 6, 817 (1957).
105. J.S. Griffiths, Theory of Transition Metal Ions (Cambridge University Press, London, 1961).
106. N.M. Atherton, Electron Spin Resonance (Ellis-Horwood, London, 1973).
107. N. Smith and J.C. Speakman, Trans. Farad. Soc., 44, 1031 (1948).
108. J.R. Dickinson, Ph.D. Thesis, University of British Columbia, 1974.
see also J.A. Hebden, Ph.D. Thesis, University of British Columbia, 1970
and N.S. Dalal, J.R. Dickinson and C.A. McDowell, J. Chem. Phys., 57, 4254 (1972).
109. J.A. Hebden, Ph.D. Thesis, University of British Columbia, 1970. Also
C.R. Byfleet, D.P. Chong, J.A. Hebden and C.A. McDowell, J. Mag. Reson. 2, 69 (1970).
110. J.A. Pople and D.L. Beveridge, Approximate Molecular Orbital Calculations (McGraw Hill, New York, 1970).

111. A. Carrington and A.D. McLachlan, Introduction to Magnetic Resonance (Harper and Row, New York, 1967) p. 106.
112. D.W. Ovenall and D.H. Whiffen, Mol. Phys., 4, 135 (1961).
113. S. Schlick, B.L. Silver and Z. Luz, J. Chem. Phys., 54, 867 (1971).
114. P.W. Atkins, N. Keen and M.C.R. Symons, J. Chem. Soc., 2873 (1962).
115. J.H. Sharp and M.C.R. Symons, J. Chem. Soc. (A), 3075 (1970).
116. K. Nunome, K. Toriyama and M. Iwasaki, J. Chem. Phys., 62, 2927 (1975).
117. K.O. Hartman and J.C. Hisatune, J. Chem. Phys., 44, 1913 (1966).
118. J.E. Bennet, B. Mile and H. Thomas, Trans. Faraday Soc., 61, 2357 (1965).
119. G.W. Chantry and D.H. Whiffen, Mol. Phys., 5, 189 (1962).
120. R.E. Bellis and S. Clough, Mol. Phys., 10, 23 (1965).
121. R.J. Cook and D.H. Whiffen, J. Phys. Chem., 71, 93 (1967).
122. W.H. Zachariasen, J. Amer. Chem. Soc., 62, 1011 (1940).
123. P.L. Markila, M.Sc. Thesis, University of British Columbia, (1974).
124. J.H. O'Donnell and D.F. Sangster in Principles of Radiation Chemistry (American Elsevier, New York, 1970).
125. M.E. Jacox and D.E. Milligan, Chem. Phys. Letters, 28, 163 (1974).
126. J.A. McMillan and S.A. Marshall, J. Chem. Phys., 48, 467 (1968).
127. L.R. Dalton, A.L. Kwiram and J.A. Cowen, Chem. Phys. Letters, 14, 77 (1972).
128. S.K. Wong and J.K.S. Wan, J. Chem. Phys., 55, 4940 (1971).
129. L.R. Dalton, A.L. Kwiram and J.A. Cowen, Chem. Phys. Letters, 17, 495 (1972).
130. W.C. Lin and C.A. McDowell, unpublished results.
131. L. Manojlović and J.C. Speakman, Acta Cryst., B(24), 323 (1968).
132. G.E. Bacon and N.A. Curry, Acta Cryst., 10, 524 (1957).
133. G.E. Bacon and N.A. Curry, Acta Cryst., 13, 717 (1960).
134. J.C. Speakman, private communication.
135. J. Trotter, private communication.

136. A. Carrington and I.C.P. Smith, *Molec. Phys.*, 9, 137 (1965).
137. J.A. Pople, D.L. Beveridge and P.A. Dobosh, *J. Amer. Chem. Soc.*, 90, 4201 (1968).
138. see for example J. Tino and V. Klimo, *Chem. Phys. Letters*, 25, 427 (1974).
139. H.G. Benson and A. Hudson, *Molec. Phys.*, 20, 185 (1971).
140. Y.A. Kruglyak and E.V. Mozdor, *Theoret. Chim. Acta*, 15, 365 (1969).
141. M. Raimondi, M. Simonetta and G.F. Tantardini, *J. Chem. Phys.*, 56, 5091 (1972).
142. W.T. Dixon and R.O.C. Norman, *J. Chem. Soc.*, 4837 (1964).
143. H. Fischer, *Z. Naturforsch.*, 20, 488 (1965).
144. R.V. Lloyd and D.E. Wood, *J. Amer. Chem. Soc.*, 96, 659 (1974).
145. A.M. Ihrig, P.R. Jones, I.N. Jung, R.V. Lloyd, J.L. Marshall and D.E. Wood, *J. Amer. Chem. Soc.*, 97, 4477 (1975).
146. M. Shansal, *Molec. Phys.*, 23, 441 (1972).
147. D.N. Nanda and P.T. Narasimhan, *Internat. J. Quant. Chem.*, VIII, 451 (1974).
148. R.J. Cook and D.H. Whiffen, *J. Chem. Phys.*, 43, 2908 (1965).
149. K. Toriyama, K. Nunome and M. Iwasaki, *J. Chem. Phys.*, 64, 2020 (1976).
150. A. Hinchliffe, *Chem. Phys. Letters*, 13, 594 (1972).
151. J.C. Shug and D.H. Phillips, *J. Chem. Phys.*, 59, 1616 (1973).
152. P. Neta and R.H. Schuler, *J. Phys. Chem.*, 77, 1368 (1973).
153. L.D. Kispert, H. Lin and C.U. Pittman, *J. Amer. Chem. Soc.*, 95, 1657 (1973).
154. V.A. Kuprievich, Y.A. Kruglyak and V. Mozdor, *Intern. J. Quantum Chem.*, 4, 73 (1970).
155. R.W. Fessenden and R.H. Schuler, *J. Chem. Phys.*, 39, 2147 (1963).
156. U.R. Böhme and H.C. Wolf, *Chem. Phys. Letters*, 17, 582 (1972).
157. J.N. Herak, D. Krilov and C.A. McDowell, *J. Mag. Reson.*, 23, 1 (1976).
158. G.L. Swartz and W.M. Gulick, *Mol. Phys.*, 30, 869 (1975); R.P. Mason and J.E. Harriman, *J. Chem. Phys.*, 65, 2274 (1976).
159. P. Gloux and B. Lamotte, *Mol. Phys.*, 25, 161 (1973).

Appendix 1 The Effect of g-Anisotropy on ENDOR Frequencies

In the high-field approximation one replaces \underline{s} by $m_s \underline{h}$ where \underline{h} is a unit vector parallel to the static field H . If g-anisotropy is significant we should use $m_s \underline{h}'$ where

$$\underline{h}' = \underline{h} \cdot \underline{g} / (\underline{h} \cdot \underline{g}^2 \cdot \underline{h})^{1/2} \quad (A-1.1)$$

If the relative anisotropy is small we can write

$$\underline{h}' = \underline{h} + \underline{\lambda} \quad (A-1.2)$$

where $\underline{h} \cdot \underline{\lambda} = 0$ and $\lambda^2 \ll 1$. The high-field ENDOR Hamiltonian then becomes

$$\mathcal{H} = (m_s \underline{h}' \cdot \underline{A} - \nu_p \underline{h}) \cdot \underline{I} \quad (A-1.3)$$

with transition frequencies given by

$$\nu_{m_s} = [m_s^2 \underline{h}' \cdot \underline{A}^2 \cdot \underline{h}' - 2m_s \nu_p \underline{h}' \cdot \underline{A} \cdot \underline{h} + \nu_p^2]^{1/2} \quad (A-1.4)$$

Using the fact that \underline{A} and \underline{A}^2 are symmetric, substitution of (A.1-2) gives

$$\begin{aligned} \nu_{m_s} &= [m_s^2 (\underline{h} \cdot \underline{A}^2 \cdot \underline{h} + 2\underline{h} \cdot \underline{A}^2 \cdot \underline{\lambda} + \underline{\lambda} \cdot \underline{A}^2 \cdot \underline{\lambda}) \\ &\quad - 2m_s \nu_p (\underline{h} \cdot \underline{A} \cdot \underline{h} + \underline{\lambda} \cdot \underline{A} \cdot \underline{h}) + \nu_p^2]^{1/2} \\ &\equiv [\nu_{iso}^2 + \Delta]^{1/2}, \end{aligned} \quad (A-1.5)$$

where ν_{iso} is the frequency corresponding to an isotropic g (i.e. $\lambda=0$) and Δ is the sum of terms containing λ .

Since λ and hence Δ are assumed small we can neglect terms in λ^2 and approximate the frequency shift, $\delta\nu \equiv \nu_{m_s} - \nu_{iso}$, by

$$\delta v \approx \frac{\partial v}{\partial \Delta} \Delta = \frac{1}{2} [v_{iso}^2 + \Delta]^{-1/2} \Delta \approx \Delta / 2v$$

$$\therefore |\delta v| \approx \frac{1}{4v} [\lambda \cdot A \cdot h + 2v \lambda \cdot A \cdot h] \quad (A-1.6)$$

Note that in the axis system defined by $(h, \lambda, h \times \lambda)$, $\lambda \cdot A \cdot h$ is an off-diagonal element of A multiplied by λ ; the same holds of course for A^2 . Thus if either h or λ lies along a principal axis of A , δv is zero; hence there will be no effect on an isotropic A tensor.

So far the treatment has been quite general and holds for any λ such that $\lambda^2 \ll 1$. To evaluate λ in terms of g we take $g = gU + \delta$, written for short as $g + \delta$, with $g \sim 2$ and $\delta_{ij} \ll 1$ for all i, j .

Then

$$h' = (gh + h \cdot \delta) / |gh + h \cdot \delta| ;$$

to first order in δ this becomes

$$h' = h + \frac{1}{g} [h \cdot \delta - (h \cdot \delta \cdot h) h]$$

or

$$\begin{aligned} \lambda &= \frac{1}{g} [h \cdot \delta - (h \cdot \delta \cdot h) h] \\ &= \frac{h}{g} [\delta - h \cdot \delta \cdot h U] \end{aligned} \quad (A-1.7)$$

The requirement that $\lambda \cdot h = 0$ is satisfied since $h \cdot U = h$. Also, if h lies along a principal axis of δ , $h \cdot \delta = (h \cdot \delta \cdot h) h$, and λ vanishes. Combining this with the result in equation (A-1.6) shows that the effect of g anisotropy is greatest in directions away from the principal vectors of both A and g and hence the effect would be most marked if A and g have a common axis system.

As an example we take g axial, with principal values 2.000, 2.000, 2.000+ ϵ , and let

$$\underline{h} = \underline{\lambda}\underline{i} + \underline{m}\underline{j} + \underline{n}\underline{k} \quad \text{in the g-frame.}$$

$$\begin{aligned} \text{Then } \underline{h} \cdot \underline{g} &= 2\underline{\lambda}\underline{i} + 2\underline{m}\underline{j} + (2\underline{n} + \underline{\epsilon}\underline{n})\underline{k} \\ &= 2\underline{h} + \underline{n}\underline{\epsilon}\underline{k} \quad , \end{aligned}$$

$$\text{so that } \underline{h}' = (2\underline{h} + \underline{n}\underline{\epsilon}\underline{k}) / |2\underline{h} + \underline{n}\underline{\epsilon}\underline{k}| \quad . \quad (\text{A-1.8})$$

After evaluating the denominator and using the binomial theorem to retain only terms in ϵ this becomes

$$\underline{h}' \approx \underline{h} + \frac{1}{2}\underline{n}\underline{\epsilon}(\underline{k} - \underline{n}\underline{h}) \quad (\text{A-1.9})$$

$$\text{i.e. } \underline{\lambda} = \frac{1}{2}\underline{n}\underline{\epsilon}(\underline{k} - \underline{n}\underline{h}) \quad . \quad \text{Again } \underline{\lambda} \cdot \underline{h} = 0 \text{ since } \underline{k} \cdot \underline{h} = \underline{n}.$$

We can estimate the magnitude of λ in terms of ϵ as follows:

$$\begin{aligned} \lambda &= (\underline{\lambda} \cdot \underline{\lambda})^{\frac{1}{2}} = \frac{1}{2}\underline{n}\underline{\epsilon}(1 - 2\underline{n}\underline{h} \cdot \underline{k} + \underline{n}^2)^{\frac{1}{2}} \\ &= \frac{1}{2}\underline{n}\underline{\epsilon}(1 - \underline{n}^2)^{\frac{1}{2}} \quad . \end{aligned} \quad (\text{A-1.10})$$

$$\text{Since } |\underline{n}| < 1, \quad |\underline{n}|(1 - \underline{n}^2)^{\frac{1}{2}} = \sin\theta\cos\theta = \frac{1}{2}\sin 2\theta \leq 0.5$$

$$\therefore \lambda \leq |\epsilon|/4 \quad . \quad (\text{A-1.11})$$

For a numerical estimate of δv we consider the \underline{A} tensor given by

$$\underline{A}_{yy} = \underline{A}_{zz} = 30\text{MHz}, \quad \underline{A}_{xx} = 50\text{MHz}, \quad \underline{A}_{xy} = 25\text{MHz}, \quad \underline{A}_{yz} = \underline{A}_{xz} = 0; \quad \underline{h} = \frac{1}{\sqrt{2}}(1, 1, 0).$$

$$\text{These values give } \underline{h} \cdot \underline{A} \cdot \underline{h} = 65\text{MHz}; \quad \underline{h} \cdot \underline{A}^2 \cdot \underline{h} = 4325(\text{MHz})^2. \quad \text{Thus using (A-1.5)}$$

$$\text{with } \underline{v}_p = 14.3\text{MHz and } m_s = -\frac{1}{2}$$

$$\underline{v}_{\text{iso}} = 47.07 \text{ MHz.}$$

By (A-1.6)

$$|\delta v| = \frac{1}{94.14} [\underline{\lambda} \cdot \underline{A}^2 \cdot \underline{h} + 28.6 \underline{\lambda} \cdot \underline{A} \cdot \underline{h}] \quad .$$

$$\text{If } \underline{\lambda} = \frac{\lambda}{\sqrt{2}}(1, 0, 1) \text{ this becomes,}$$

$$|\delta\nu| = \frac{1}{94.14}[\lambda(2563 + 1072.5)] = \lambda(39) \text{ MHz} .$$

For $\delta\nu \gtrsim 100 \text{ kHz} = 0.1 \text{ MHz}$ we require $\lambda \gtrsim 0.0025$. By (A-1.11) this implies a g-anisotropy $\gtrsim 0.01$ which is large for an organic free radical but not totally unreasonable. Since the angular variation of ν_{m_s} will be slightly different from that of ν_{iso} , it may be possible in favourable cases to estimate the relative g-anisotropy from ENDOR data in any event, if the g-tensor is known to be highly anisotropic, allowance must be made for this when large anisotropic hyperfine tensors are to be determined.

Appendix 2 Some Aspects of the Dipolar Hyperfine Interaction

The dipolar hyperfine interaction has the form

$$-\langle \underline{\mu}_e \cdot \left(\frac{3\underline{r}\underline{r} - U}{r^3} \right) \cdot \underline{\mu}_N \rangle \quad [\text{A-2.1}]$$

where the angular brackets denote a spacial average over the wavefunction of the unpaired electron. If we take $\underline{\mu}_N = +g_N \beta_N \underline{I}$ and $\underline{\mu}_e = \rho g \beta \underline{S}$ where ρ is the spin density, both $\underline{\mu}_e$ and $\underline{\mu}_N$ are independent of the spacial variables and can be taken outside the brackets. Comparison with the standard form $\underline{S} \cdot \underline{B} \cdot \underline{I}$ then shows that

$$\begin{aligned} \underline{B} &= \rho g \beta g_N \beta_N \left\langle \frac{3\underline{r}\underline{r} - U}{r^3} \right\rangle \\ &= \rho \frac{\mu_e}{S} \frac{\mu_N}{I} \left\langle \frac{3\underline{r}\underline{r} - U}{r^3} \right\rangle \end{aligned} \quad [\text{A-2.2}]$$

Thus for a given geometry and spin density, the hyperfine interactions of different nuclei will scale as $g_N \mu_N / I$.

For $^{23}\text{Na} (I=3/2, \mu_N=2.2161\beta_N)$ and $^1\text{H} (I=1/2, \mu_N=2.7917\beta_N)$, the g_N values are in the ratio 0.265:1, so for a given spin distribution the dipolar tensor for a ^{23}Na nucleus will be only 26.5% of that for a proton at the same position.

For an interatomic distance $r \approx 2.5\text{\AA}$ and $\rho=1$, the largest principal value of a proton coupling tensor is ~ 5 MHz, the exact value depending on the spatial distribution of the local spin density; thus for unit spin density the corresponding maximum value for a sodium hyperfine tensor would be ~ 1.3 MHz. For $\rho \sim 0.6$ as in the $\text{Na}^+ \dots \text{CO}_2^-$ ion pair in sodium formate the maximum through-space dipolar coupling to the sodium atom would be ~ 1 MHz.

For a system with cylindrical symmetry about an axis defined by \underline{u} (A-2.2) can be written

$$\underline{B} = g\beta g_N \beta_N (3\underline{u}\underline{u} - \underline{U}) \cdot \left\langle \frac{1}{r^3} \right\rangle .$$

One-centre interactions between a nucleus and spin in one of its p orbitals form the simplest example. The dipolar energy is then proportional to β given by

$$\beta = \underline{\mu}_e \cdot (3\underline{u}\underline{u} - \underline{U}) \cdot \underline{\mu}_N .$$

If one makes the first order substitution $\underline{\mu}_e = \mu_e \underline{h} (\mp g\beta m_s H/H)$ this becomes

$$\beta = \underline{\mu}_e \cdot (3(\underline{h} \cdot \underline{u})\underline{u} - \underline{h}) \cdot \underline{\mu}_N .$$

Two extreme cases of most interest:

(a) The nuclear spin is quantised along \underline{H} : unless \underline{B} is very small (so that the nuclear Zeeman energy dominates); this requires a large isotropic hyperfine term. Then $\underline{\mu}_N \approx \mu_N \underline{h}$ and

$$\beta = \mu_e \mu_N (3(\underline{h} \cdot \underline{u})^2 - 1) = \mu_e \mu_N (3\cos^2\theta - 1)$$

$$\text{where } \underline{h} \cdot \underline{u} = \cos\theta .$$

(b) The nucleus experiences a field dominated by the dipolar interaction itself, so that $\underline{\mu}_N$ is quantised along the vector $3(\underline{h} \cdot \underline{u})\underline{u} - \underline{h}$. In this case

$$\begin{aligned} \beta &= \mu_e \mu_N | (3(\underline{h} \cdot \underline{u})\underline{u} - \underline{h}) | \\ &= \mu_e \mu_N [9(\underline{h} \cdot \underline{u})^2 - 6(\underline{h} \cdot \underline{u})^2 + 1]^{1/2} \\ &= \mu_e \mu_N [3\cos^2\theta + 1]^{1/2} . \end{aligned}$$

In general if there is an isotropic hyperfine interaction, a , and a significant nuclear Zeeman term as well as the dipolar field, μ_N will be

quantised along the resultant of all three effective fields:

$$g_N \beta_N H_{\text{eff}} = \frac{(3(\underline{h} \cdot \underline{u})\underline{u} - \underline{h}) \mu_e \mu_N \langle r^{-3} \rangle}{2SI} + \frac{(a + v_p)}{2} \underline{h}$$

$$= b \cos \theta \underline{u} + c \underline{h}$$

where $b = 3\mu_e \mu_N \langle r^{-3} \rangle / (2SI)$, $c = \frac{1}{2}a + v_p - \frac{1}{2}\mu_e \mu_N \langle r^{-3} \rangle / (2SI)$

The corresponding unit vector is

$$\underline{h}' = \frac{b \underline{u} \cos \theta + c \underline{h}}{(c^2 + b^2 \cos^2 \theta + 2bc \cos \theta)^{1/2}} = \frac{b \underline{u} \cos \theta + c \underline{h}}{[c^2 + (b^2 + 2bc) \cos^2 \theta]^{1/2}}$$

Then β varies as

$$\beta = \mu_e \mu_N [3 \cos \theta \underline{u} - \underline{h}] \cdot \underline{h}'$$

$$= \mu_e \mu_N \frac{[(2b + 3c) \cos^2 \theta - c]}{[c^2 + b(b + 2c) \cos^2 \theta]^{1/2}}$$

which reduces to case (a) when $c \gg b$ and to case (b) when $c = -b/3$.

Appendix 3 Misalignment of Planes of Observation

We assume that data have been taken in three planes close to the orthogonal crystallographic planes \underline{ab} , \underline{bc}^* , \underline{ac}^* . 'Close' in this context means $<5^\circ$. \underline{b} is the unique axis of the crystal, and the symmetry requires that the elements of two symmetry related tensors $T_{ii}^{(1)}$ and $T_{ii}^{(2)}$ obey the relationships

$$T_{ii}^{(1)} = T_{ii}^{(2)} \quad \text{all } i$$

$$T_{23}^{(1)} = -T_{23}^{(2)} \quad T_{12}^{(1)} = -T_{12}^{(2)}$$

$$T_{13}^{(1)} = +T_{13}^{(2)}$$

(The subscripts 1, 2, 3 are associated with vectors \underline{a} , \underline{b} , \underline{c}^* respectively.)

This implies that there will be 'site splittings' in the \underline{ab} and \underline{bc}^* planes, with the sites becoming degenerate at the 'crossover' points at the \underline{a} , \underline{b} , \underline{c}^* axes, and everywhere in the \underline{ac} plane. If the planes of observation are slightly misaligned, these crossover points will be shifted. Those corresponding to \underline{a} and \underline{c}^* will - necessarily - remain in the \underline{ac} plane, but will be shifted by rotations about \underline{b} . The cross-over point corresponding to \underline{b} will be shifted in an arbitrary direction due to rotations about the other axes. A misalignment of \underline{ac}^* will result in the line being split.

The misalignment can be represented by a rotation matrix R , which in general will be different for each plane. The data observed in a given plane of observation correspond to an 'apparent' tensor A which is related to the true tensor T via the misalignment; thus

$$A = R^{-1} \cdot T \cdot R \equiv R^T \cdot T \cdot R \quad \text{for either site.}$$

Under the conditions applying here viz small rotation, R will approximate the identity matrix. Thus cross-products of off-diagonal elements of R

can be neglected and diagonal elements can be replaced by unity. This is equivalent to commutation of the rotations about the three axes, so that these rotations can be treated as independent. With these approximations the elements of \underline{A} can be evaluated:

$$A_{11} = T_{11} + 2T_{12}R_{21} + 2T_{13}R_{31}$$

$$A_{22} = T_{22} + 2T_{12}R_{12} + 2T_{23}R_{32}$$

$$A_{33} = T_{33} + 2T_{23}R_{23} + 2T_{13}R_{13}$$

$$A_{12} = T_{12} + T_{11}R_{12} + T_{22}R_{21} + T_{13}R_{32} + T_{32}R_{31}$$

$$A_{13} = T_{13} + T_{11}R_{13} + T_{33}R_{31} + T_{12}R_{23} + T_{23}R_{21}$$

$$A_{23} = T_{23} + T_{22}R_{23} + T_{33}R_{32} + T_{12}R_{13} + T_{13}R_{12}$$

If rotations about \underline{b} are eliminated (so that $R_{31}=R_{13}=0$ and $R_{ij}=-R_{ji}$ for $i \neq j$) these equations reduce to

$$A_{11} = T_{11} - 2T_{12}R_{12}$$

$$A_{22} = T_{22} + 2T_{12}R_{12} + 2T_{23}R_{32}$$

$$A_{33} = T_{33} - 2T_{23}R_{32}$$

$$A_{12} = T_{12} + (T_{11}-T_{22})R_{12} + T_{13}R_{32}$$

$$A_{13} = T_{13} - T_{12}R_{32} - T_{23}R_{12}$$

$$A_{23} = T_{23} + (T_{33} - T_{22})R_{32} + T_{13}R_{12}.$$

Note that the trace is conserved. Also, by virtue of the symmetry relations for $T_{ij}^{(1)}$ and $T_{ij}^{(2)}$ the numerical mean value of $A_{ij}^{(1)}$ and $A_{ij}^{(2)}$ is T_{ij} . Since $A_{ij}^{(1)}$ and $A_{ij}^{(2)}$ are thus symmetrically displaced from $T_{ij}^{(1)}$ and $T_{ij}^{(2)}$ the lines corresponding to the two sites will still have the correct crossover frequency.

A more detailed proof of this is given below.

Either set of equations can be used to obtain the R_{ij} by fitting the experimental data. One method which is directly applicable uses the displacement of the crossover point from an 'axis' in the misaligned plane of observation.

At axis 1, in the plane of observation, the first order ENDOR frequency for site (1) will be given by

$$\nu_{(1)}^2 = (\frac{1}{4}A_{11}^2)^{(1)} + \nu_p A_{11}^{(1)} + \nu_p^2,$$

with $(A_{11}^2)_{11} = A_{11}^2 + A_{12}^2 + A_{13}^2$.

The ENDOR frequency for site (2) will be the same expression with $A_{ij}^{(1)}$ replaced by $A_{ij}^{(2)}$.

If ν_T is the true ENDOR frequency at axis 1 given by

$$\nu_T^2 = (\frac{1}{4}T_{11}^2) + \nu_p T_{11} + \nu_p^2,$$

then

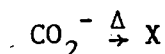
$$\begin{aligned} \nu_{(i)}^2 - \nu_T^2 = & \frac{1}{4}[(A_{11}-T_{11})(A_{11}+T_{11}) + (A_{12}-T_{12})(A_{12}+T_{12}) \\ & + (A_{13}-T_{13})(A_{13}+T_{13})] + \nu_p(A_{11}-T_{11}) \end{aligned}$$

where (i) refers to site (1) or (2) and the same superscript is understood for A_{ij} and T_{ij} . To a good approximation the left hand side is $2\nu_T \Delta\nu_{(i)}$ where $\Delta\nu_{(i)}$ is the shift from the 'true' frequency, while the products on the right hand side are essentially of the form $2T_{ij} \Delta A_{ij}$ where $\Delta A_{ij} = A_{ij} - T_{ij}$.

As noted above, if $R_{13}=0$ $|A_{ij}^{(1)}|$ and $|A_{ij}^{(2)}|$ are symmetrically placed about $|T_{ij}|$, so that $\Delta A_{ij}^{(1)} = -\Delta A_{ij}^{(2)}$ and hence $\Delta \nu_{(1)} = -\Delta \nu_{(2)}$. Thus for small misalignments the ENDOR lines from sites (1) and (2) in the region of the crossover are symmetric about the true lines; and hence the crossover frequency is unchanged. The same holds for other axes by permutation of subscripts.

Appendix 4 A uv-Induced Radical Reaction in Irradiated
Sodium Formate

Bellis and Clough identified as $(\text{H.C(O).O.CO}_2)^{-2}$ the free radical produced when X or γ irradiated sodium formate is heated. Denoting this species by X, the reaction



is essentially complete after ~30 minutes at 120°C or after ~1 year's aging at room temperature, as is easily shown by the change in appearance of the EPR spectrum.

In the course of our studies on NaHCO_2 we found that this reaction could be reversed by ultra violet light. The optimum wavelength lies in the range 270-300 nm. The kinetics of this reverse reaction were studied by uv-irradiating crystals containing radical X in the EPR cavity. At suitable orientations the spectra of X and CO_2^- were sufficiently separated for the relative peak heights and linewidths to be determined quite easily, thus enabling the relative concentrations of the two radicals to be estimated.

The results of one such experiment are shown in Fig. 26. For more than 65% conversion the total concentration of radicals remained constant: the small fluctuations in the value of $[\text{CO}_2^-] + [\text{X}]$ are attributed to changes in cavity temperature. A plot of $[\text{CO}_2^-]/[\text{X}]$ vs time is essentially linear (Fig. 27), implying second order kinetics.

For a second order reaction, the slope of this plot is $k_2 C$ where k_2 is the rate constant and C the initial (=total) radical concentration. Using this fact it was possible to estimate the dependence of k_2 upon light intensity and temperature.

By interposing different neutral density filters and measuring the

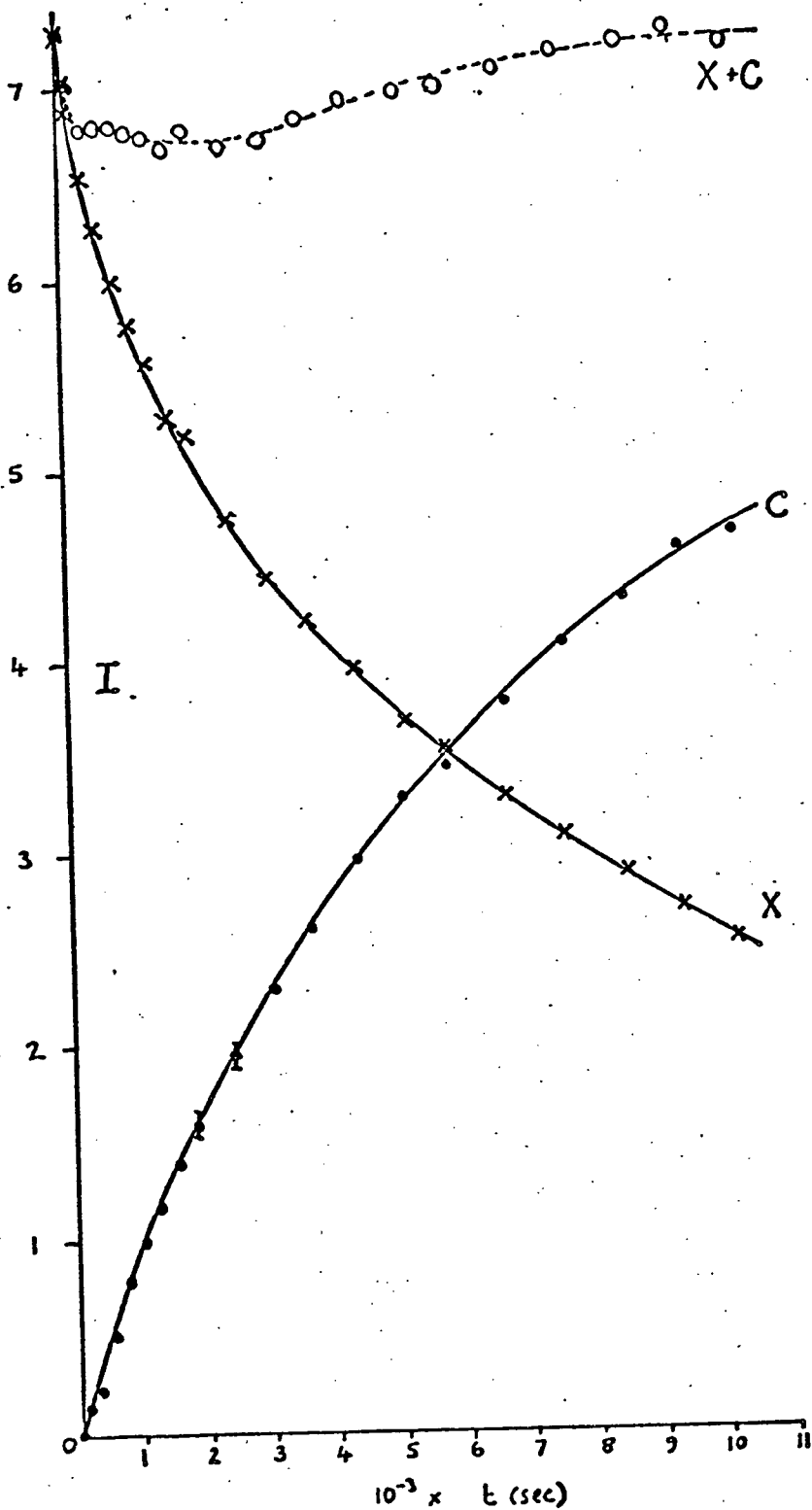


Fig. 26. Relative intensities of CO_2^- (C) and secondary radical (X) EPR spectra as a function of uv-irradiation time.

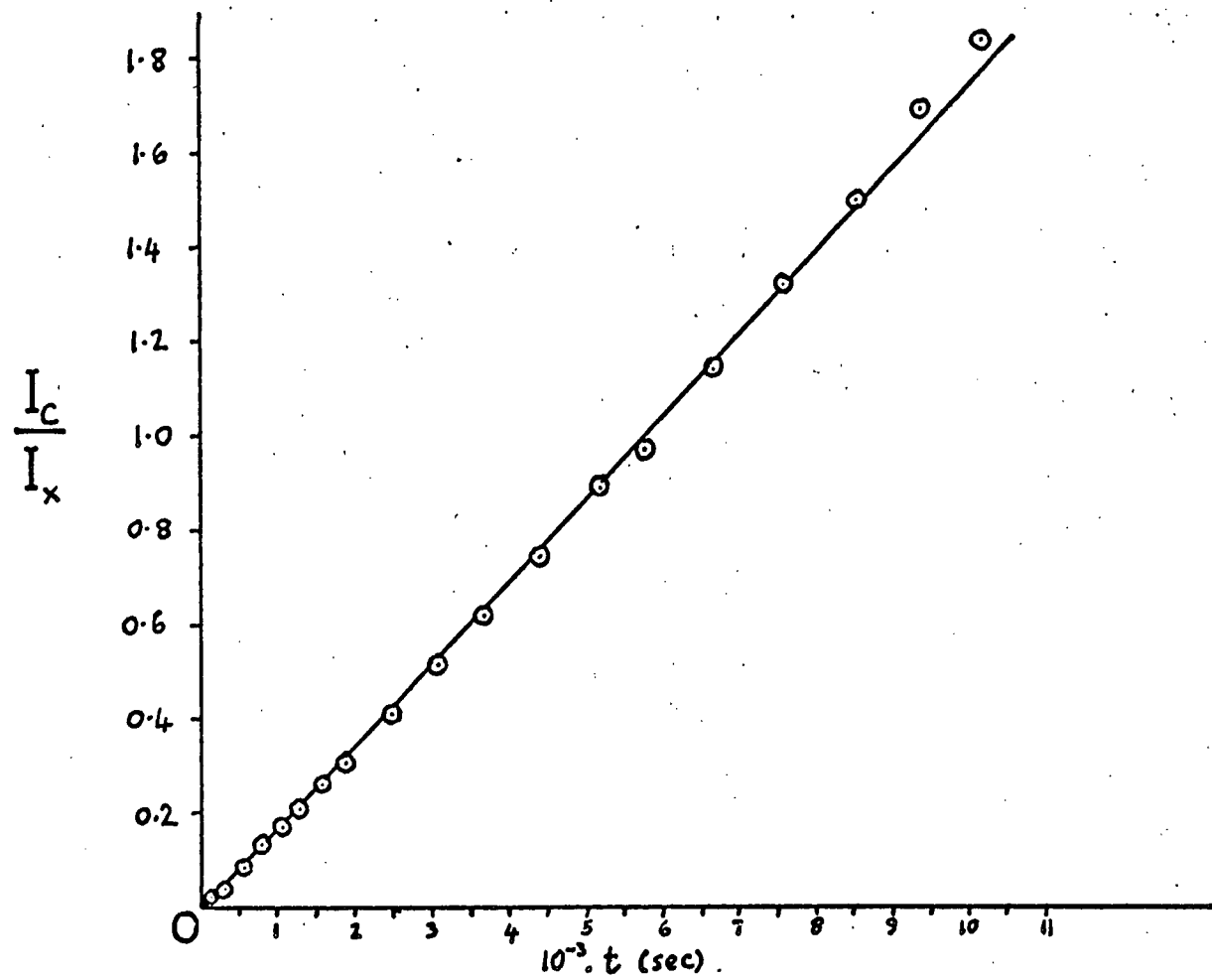


Fig. 27. Ratio of EPR intensities $[C]/[X]=I_C/I_X$ as a function of uv-irradiation time.

corresponding values of k_2C from the resulting linear plots it was found that the reaction is essentially first order with respect to light intensity, the experimental value of the exponent being 1.16 ± 0.1 .

Similarly by carrying out the irradiations at room temperature and 77K the activation energy E_a in the simple Arrhenius equation $k_2 = A \exp(-E_a/RT)$ was found to be $E_a = 0.5 \pm 0.2$ kcal/mole.

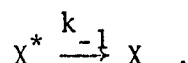
The uv-induced reaction was essentially reversible: heating the sample at 110°C for ~30 minutes restored the presence of X, and this cycle could be repeated several times, although with a small loss of intensity on heating.

These results are difficult to interpret, primarily because of the second order kinetics, which imply diffusion through the crystal lattice. The following model covers several features of the results.

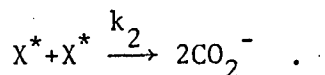
(i) Light is absorbed, either by the sodium formate lattice, or by species X itself, to form an activated species X^*



X^* decays with a high probability to X:



(ii) A small fraction of the X^* formed diffuses through the lattice until two X^* species react to form CO_2^- .



The rate equations are

$$\frac{d[X]}{dt} = -k_1 [X] + k_{-1} [X^*] ,$$

$$\frac{d[X^*]}{dt} = -k_2[X^*]^2 + k_1[X] - k_{-1}[X^*]$$

$$\frac{d[CO_2^-]}{dt} = k_2[X^*]^2$$

If $k_2[X^*] < k_1 < k_{-1}$, $[X^*]$ will be present in small proportions, almost in equilibrium with X; the overall reaction will then be driven by step (ii) giving rise to the observed second order kinetics with an effective rate constant $k_2 k_1 / k_{-1}$. Numerical solution of the rate equations confirms this result.

This model is not entirely satisfactory in that it offers no clue as to the nature of X^* or its mode of diffusion. The relatively high rate of reaction suggests that X^* may be a species which 'diffuses' by a series of head-to-tail reactions with neighbouring formate ions:



alternatively X^* might be an electron or an excitation rather than a chemical species. This possibility is favoured by the nature of step (ii), the formation of CO_2^- . The absence of any spin-spin splittings characteristic of radical pairs shows that the formation of CO_2^- from X^* does not produce two CO_2^- ions in close proximity, so some easily delocalised form of energy is probably instrumental in the reaction.